The PHILOSOPHICAL MAGAZINE

UNIVERSITY OF HAWAII
LIBRARY
MAR [illegible] '56

FIRST PUBLISHED IN 1798

1 Eighth Series No. 1 January 1956

A Journal of Theoretical Experimental and Applied Physics

EDITOR
PROFESSOR N. F. MOTT, M.A., D.Sc., F.R.S.

EDITORIAL BOARD
SIR LAWRENCE BRAGG, O.B.E., M.C., M.A., D.Sc., F.R.S.
SIR GEORGE THOMSON, M.A., D.Sc., F.R.S.
PROFESSOR A. M. TYNDALL, C.B.E., D.Sc., F.R.S.

PRICE 15s. 0d.

Annual Subscription £8 0s. 0d. payable in advance

ALERE FLAMMAM.
Printed and Published by
TAYLOR & FRANCIS LTD.
RED LION COURT, FLEET STREET, LONDON, E.C.4

PRE-PUBLICATION NOTICE

MEDICAL AND BIOLOGICAL PHYSICS

Taylor & Francis, Ltd., Publishers, wish to announce that early in 1956, they will be publishing a new International Journal dealing with the above subjects.

●

Further information concerning the policy of this journal will appear shortly or may be had on application to the Publishers

TAYLOR & FRANCIS, LTD.
RED LION COURT, FLEET STREET, E.C.4
Publications Division, Crane Court, Fleet St., E.C.4

AUSTRALIA—UNIVERSITY OF SYDNEY

Applications are invited for

RESEARCH STUDENTSHIPS/FELLOWSHIPS IN THE SCHOOL OF PHYSICS

for the year 1956

The successful applicants will be appointed, according to qualifications and experience, to a Research Studentship (£A750–£A850 per annum) or to a Research Fellowship (£A1,100–£A1,500 per annum).

Fares to and from Australia not exceeding a total of £A200 may be paid.

The awards will normally be made for a period of two years, after which the tenure may be renewed for a further period. Pre-doctoral candidates will normally be awarded Research Studentships and will be expected to pass the Physics IV examination at Honours B.Sc. level before proceeding to work for the Ph.D. degree. Study for this examination may take up part or all of the first year in Sydney. Experimental work in the School of Physics is directed by Dr. E. P. George and covers a wide field of high energy nuclear physics research. Nuclear research emulsions, cloud chambers and counters are used in the experiments at present being carried out. Among the candidates who are experimentalists preference will be given to those interested in nuclear emulsion work. Theoretical research into problems of nuclear, atomic and solid state physics is being actively pursued under the direction of Professor H. Messel. A large high-speed digital computer is under construction.

Applications, giving names of three referees, should be forwarded to reach the undersigned* not later than *31st January, 1956*. Overseas candidates are required to forward a copy of the application to the Secretary of the Association of Universities of the British Commonwealth, 36 Gordon Square, London, S.W.1.

* M. A. TELFER, *Registrar*

CONTENTS OF No. I.

Page

I. Collective Oscillations and Characteristic Electron-Energy Losses. By D. Gabor, Imperial College, London 1

II. The Optical Model Applied to the Elastic Scattering of Nucleons by Various Light Nuclei. By E. J. Burge, Y. Fujimoto and A. Hossain, H. H. Wills Physical Laboratory, University of Bristol........ 19

III. Dislocation Densities in some Annealed and Cold-Worked Metals from Measurements on the x-ray Debye–Scherrer Spectrum. By G. K. Williamson and R. E. Smallman, Metallurgy Division, A.E.R.E., Harwell........ 34

IV. Coincidence Measurements on the β-Decay of Boron 12. By N. W. Tanner, Cavendish Laboratory, Cambridge 47

V. The Measurement of the Angular Diameter of Two Intense Radio Sources. I: A Radio Interferometer using Post-Detector Correlation. By R. C. Jennison and M. K. Das Gupta, University of Manchester, Jodrell Bank Experimental Station, Cheshire 55

VI. The Measurements of the Angular Diameter of Two Intense Radio Sources. II: Diameter and Structural Measurements of the Radio Stars Cygnus A and Cassiopeia A. By R. C. Jennison and M. K. Das Gupta, Jodrell Bank Experimental Station, Cheshire 65

VII. A Thermodynamic Treatment of Ferroelectricity and Antiferroelectricity in Pseudo-Cubic Dielectrics. By L. E. Cross, Electrical Research Association, Perivale, Middlesex 76

VIII. An Unusual Double V-Event at Sea Level. By J. L. Lloyd and A. W. Wolfendale, The Physical Laboratories, The University, Manchester........ 93

IX. Correspondence :—

Proportional Counter Measurements of π-Mesonic x-rays from Beryllium. By D. West and E. F. Bradley, Atomic Energy Research Establishment, Harwell 97

Polygonization in Copper. By A. Franks and D. McLean, Communication from the National Physical Laboratory 101

Gamma Rays from Inelastic Neutron Scattering in Sodium and Iodine. By Elizabeth A. Wolf, Clarendon Laboratory, Oxford........ 102

The Interactions of Cosmic Ray Alpha-Particles. By C. J. Waddington, H. H. Wills Physical Laboratory, University of Bristol 105

The Paramagnetic Resonance Spectrum of Chlorine Dioxide. By J. E. Bennett and D. J. E. Ingram, University of Southampton 109

X. Reviews of Books........ 112

***All communications for the Philosophical Magazine should be addressed, post-paid, to the Editors, c/o Messrs. Taylor and Francis, Ltd., Red Lion Court, Fleet Street, London, England.

THE
PHILOSOPHICAL MAGAZINE
A JOURNAL OF THEORETICAL EXPERIMENTAL
AND APPLIED PHYSICS
First published in 1798
[EIGHTH SERIES—VOL. 1]

I. *Collective Oscillations and Characteristic Electron-Energy Losses*

By D. Gabor
Imperial College, London*

[Received September 1, 1955]

§ 1. The Nature of the Collision Process

Sharply defined 'characteristic' energy losses of medium-energy electrons in thin films, sometimes approaching the appearance of line-spectra, have been observed by a great number of authors.† No acceptable interpretation was forthcoming until Bohm and Pines (1952) and Pines (1954) suggested that they might represent the transfer of one or several vibrational quanta from the fast electron to the collective oscillations of the electron gas in metals.†

Since that time two pieces of experimental evidence have been found which appear to give strong support to the 'collective' interpretation. One is the recent observation by Watanabe‡ of a strong correlation between energy loss and direction of the electrons, which, as will be discussed below, appears to give a direct verification of the dispersion law $\omega(k)$ of the plasma waves. The other is the observation, by Gabor and Jull (1955) of the strongly non-linear increase of the collision cross section with film thickness. Neither of these is compatible with an interpretation by atomic collisions, but further evidence is required before rejecting other alternatives.

It will be attempted to give a simple but adequate theory of the interaction of fast electrons with thin films of solids, sufficient for covering past experiments and for suggesting new, crucial tests.

---

* Communicated by the Author.

† There is no need for exhaustive references as two very comprehensive reviews will appear shortly, one on the experimental side, the other on the theory. The first is by L. Marton, L. B. Leder and H. Mendlowitz, 1955, *Advances in Electronics* (Academic Press), the second by D. Pines, 1955, *Advances in Solid State Physics* (Academic Press). I thank these authors for letting me read their manuscripts.

‡ To be published. Quoted by Pines *loc. cit.*

Interaction of electrons with collective oscillations is a rather anomalous phenomenon, because it is a *coherent but inelastic collision process*. It is analogous to the reflection of light by moving mirrors, or by sound waves, or to Bragg-diffraction on a moving lattice. The analogue of the Čerenkov-radiation, used by Bohm and Pines, though illuminating, misses the point of coherence. In fact the wave-character of the electron is of no importance in an extended medium, as treated by these authors, but becomes so in the thin films as used in all experiments. Moreover, as will be shown below, it is not sufficient to replace the electron by a plane, monochromatic wave, but a more detailed representation of the electron beam is required, which takes account of its chromatic and geometrical coherence properties.

As regards the solid film, we will use the simplest model which appears likely to represent its relevant features. If a is the thickness of the film, we imagine it built up of rectangular ' grains ' with transverse dimensions b, c. We postulate that each grain is capable of vibrational modes corresponding to a dispersion law $\omega(k)$, and that all grains oscillate independently of one another. Most of the theory below will be applicable to any dispersion law $\omega(k)$ of longitudinal electric waves, and it is irrelevant whether this is derived from the side of the free electron gas, as in the theory of Pines and Bohm, or by an approach from the optical dispersion theory of solids, as in the recent papers by Hubbard (1955) and by Fröhlich and Pelzer (1955). It is essential only that there must be a strong dispersion, that is to say the wave number k must vary widely for a small change of the frequency ω. In some places, though, we shall make use of the dispersion of the free electron gas, as an illustration.

The main result of the theory is that it gives two new crucial tests of the hypothesis of collective oscillations. One is, that the characteristic losses must increase very strongly if the energy-spread of the bombarding electron beam is reduced. The other is that, other things being equal, the effect must become less if the geometrical coherence of the beam is increased. These are striking tests, because they mean that chromatic and geometrical coherence of the electron beam have opposite effects. Neither would have any influence if the phenomenon were an atomic collision process.

§ 2. Representing the Electron Beam

While in atomic collision processes it is sufficient to represent the incident electron as a plane wave, this is not so in the present case, as the bombarded object b, c need not be small compared with the lateral width over which the electron beam can be considered as coherent. In order to avoid complicated calculations, involving partial coherence, we represent the electron beam at the object as the juxtaposition of beamlets, each coherent in itself, incoherent with the others.

The lateral coherence width is, nearly enough, one-half of the de Broglie wavelength λ_e, divided by the angle which the image of the source (the hot cathode), subtends at the foil. For 10 kev electrons λ_e is 0·11 Å and the collimation used by most experimenters is in the limits 10^{-3}–10^{-4} radian, hence the coherence widths are of the order 50–500 Å. This happens to be a very important range, and more attention will have to be paid to the coherence width in the future.

Second, we must pay attention also to the ' chromatic coherence ' of the beam, that is to say its energy spread. We will use below perturbation theory for calculating the interaction with the collective oscillators in the solid, and for this we require an interaction time. It would be of course quite wrong to identify this with the transit time of the electron through the foil ; the particle has no place in a theory which deals with wave-features of the electron. It will be shown later that the transit time of a 10 kev electron through a 60 Å foil of Al corresponds only to a half-cycle of the collective oscillation. One could never account for the observation that the energy spread in the line corresponding to a loss of 14·7 ev is not appreciably more than the primary spread, of a fraction of a volt only, if the electron had ' seen ' only half a cycle of the oscillation. It is not the thickness of the foil, but the length of the wavetrain that counts.

In order to simplify the calculations, we will replace the inhomogeneous beam by pulses of monochromatic waves, of duration τ. It is evident from the uncertainty principle that for a hot cathode of temperature T this must be of the order $\hbar/kT$, but the numerical factor is of great importance because the collision probability will be found directly proportional to τ. In the Appendix a careful estimation of the best fit has been carried out, and the result is

$$\tau=\pi\hbar/kT. \qquad . \quad . \quad . \quad . \quad . \quad . \quad . \quad . \quad . \quad (1)$$

It is useful to express this in terms of the wavetrain length, τv, where v is the velocity of the primary electrons. This is

$$\tau v=\pi\hbar/kTv=(\pi\hbar/kc)\beta/T=7{\cdot}2\beta/T \text{ cm.}$$

For a tungsten cathode, as used by all experimenters, $T=2500$°c, and for 10 kev electrons, $\beta=0{\cdot}197$, this is 5700 ångströms ; many times more than the foil thicknesses which are at most a few hundred ångströms. In aluminium for instance this wave ' sees ' 34 full cycles, irrespective of the foil thickness.

§ 3. THE MODEL OF THE FOIL

The Bohm–Pines theory of collective electron interaction has not yet been extended to non-uniform structures, and it is difficult to say what gaps or structural differences must exist between two , grains ' to make them independent. The experiments of Jull and the author suggest that it is sufficient to introduce a carbonaceous ' contamination ' layer of the order 10–20 Å between two gold layers, or a gold film of similar thickness between two aluminium layers for effective separation. It is not our purpose at present to go into this question ; it will be assumed that the grain sizes are given, and we will discuss the consequences.

A rectangular grain with the boundaries $x=0, a,\ y=0, b,\ z=0, c$ is completely decoupled from its neighbours if the electric field is permanently zero at the boundaries. Thus the potential field ϕ can be represented by a sum of standing-wave modes k, $\omega(k)$

$$\phi=\phi_k \cos(\pi n_1 x/a) \cos(\pi n_2 y/b) \cos(\pi n_3 z/c) \exp(i\omega t). \quad . \quad (2)$$

The mode numbers n_1, n_2, n_3 are positive integers, starting with unity, and ending where the wave number k

$$k^2=\pi^2\left(\frac{n_1^2}{a^2}+\frac{n_2^2}{b^2}+\frac{n_3^2}{c^2}\right) \quad . \quad . \quad . \quad . \quad . \quad . \quad (3)$$

reaches the critical or ' cut-off ' value k_c.

In principle we could use this representation for any grain size, but it will be convenient to use it only if b, c are smaller than the lateral coherence widths. If the grains are larger this is not convenient because it is a redundant representation. It is evident that the standing character of the waves will not be noticeable if the grains very much exceed the coherence dimensions, but it can be shown that this will be the case even if they exceed them only a few times. Let us now consider b, c as the coherence widths, and B, C as the grain dimensions. First, it is clear that as soon as $B \geqslant 2b$, $C \geqslant 2c$ there will be no restriction inside b, c on the *instantaneous* configurations of the electric field. Yet, the grain walls could still be noticed by the waves sent out from b, c which return into the region after reflection. But these reflections can be disregarded if the wave returns into b, c only after the interaction time.

It will be shown later, and it is also evident, that in a grain smaller than the coherence region a single collision process will appreciably excite two modes in n_1, n_2, n_3 simultaneously. In a grain B, C, it will excite $2B/b$, $2C/c$ modes in n_2, n_3, because these modes cannot be distinguished inside b, c. These modes then form a *wavegroup*, of approximate lengths b, c which will move towards the grain boundaries with the group velocity $V_g=d\omega/dk$. With the assumption mentioned above this must be a small velocity, because of the strong dispersion. As an illustration let us use the law of Pines and Bohm for a free electron gas (degenerate).

$$\omega^2=\omega_0^2+u^2k^2, \quad u^2=\tfrac{6}{5}E_F/m \quad . \quad . \quad . \quad . \quad . \quad . \quad (4)$$

where E_F is the Fermi energy. This gives

$$V_g=\frac{d\omega}{dk}=\frac{6}{5}\frac{E_F}{m}\frac{k}{\omega}=\frac{6hk}{5m}\frac{E_F}{E_L}=8{\cdot}75\frac{E_F}{E_L}\frac{1}{\lambda}.$$

Here E_L is the characteristic loss energy, and $\lambda=2\pi/k$ is the wavelength. E_F/E_L is for most metals about 2/3, and the smallest (critical) λ is (in aluminium) about 10 Å. Hence the group velocity is at most about 6×10^7 cm sec^{-1}. τ on the other hand, for a tungsten cathode, is about 10^{-11} sec, hence the wavegroup will move at most about 60 ångströms during the interaction time. This means that if the grain size is twice the coherence width, the standing-wave restriction will be absolutely unnoticeable inside a border 30 Å from the grain boundaries. In brief, as soon as the grains appreciably exceed the coherence region, we can substitute for the potential field inside b, c, instead of eqn. (2) the *travelling-wave pattern*

$$\phi=\phi_k \cos\frac{\pi n_1 x}{a} \exp\left\{2\pi i\left(\frac{n_2 y}{b}+\frac{n_3 z}{c}\right)\right\}\exp(i\omega t) \quad . \quad . \quad (5)$$

in which the mode numbers n_2, n_3 run over positive and negative values, not excluding zero. It will be shown later that, other things being equal, the pattern 5 produces about four times the collision probability than the standing-wave pattern 2.

§ 4. INTERACTION WITH VIBRATIONAL MODES, AS A PERTURBATION PROBLEM

Assuming first that the grain a, b, c is inside the coherent region, we describe the incident electron as a plane monochromatic wave, of finite duration

$$\Psi_0(x, y, z, t)=\text{const.} \exp\{i(\kappa_0 x-(E_0/\hbar)t\} \qquad 0<t<\tau$$

where $\kappa_0=2\pi/\lambda_e$ is the wave number and E_0 the mean energy of the beam electrons. In the interaction this breaks up into a mixture of states

$$\Psi_m(x, y, z, t)=\psi_m(x, y, z) \exp\{-i(E_m/\hbar)t\}$$

with $$\psi_m=(abc)^{-1/2} \exp\{i(\kappa_1 x+\kappa_2 y+\kappa_3 z)_m\}.$$

If one subjects the wave numbers κ_1, κ_2, κ_3 to the conditions

$$a\kappa_1=2\pi m_1, \quad b\kappa_2=2\pi m_2, \quad c\kappa_3=2\pi m_3$$

with integer m_1, m_2, m_3—s, the ψ_m form an orthonormal set in a, b, c. One can then apply a well-known result of first-order perturbation theory. If at the time $t=0$ the electron is in a state O, the probability amplitude c_m of the state m will grow during the interaction time according to

$$\frac{dc_m}{dt}=-i\frac{e}{\hbar}\exp\left\{-i\left(\frac{E_0-E_m}{\hbar}\right)t\right\}\int_0^a\int_0^b\int_0^c \psi_m{}^*\phi\psi_0\, dx\, dy\, dz$$

where ϕ is the electrostatic potential in a, b, c. Assuming that the total of the transition probabilities is not large, the probability of the electron being found in state m after the interaction time τ is

$$c_m{}^*c_m=\left(\frac{e}{\hbar}\right)^2\left|\int_0^\tau\int_0^a\int_0^b\int_0^c \exp(-i\Omega t)\psi_m{}^*\phi\psi_0\, dt\, dx\, dy\, dz\right|^2 . \quad . \quad (6)$$

Here we have introduced the 'loss frequency'

$$\Omega=(E_0-E_m)/\hbar=E_L/\hbar$$

and we will continue to measure energies in terms of frequencies.

It is convenient and justified to consider the m-states as continuous, as the electron wavelength is always very small compared with the dimensions a, b, c. We specify the electron after the collision by its loss frequency Ω, its polar angle θ and its azimuth ϕ. Let the probability of the electron being found in the range $d\Omega$, $d\theta$, $d\phi$ be

$$p(\Omega, \theta, \phi) \sin\theta\, d\Omega\, d\theta\, d\phi=c_m{}^*c_m\, dn \quad . \quad . \quad . \quad . \quad (7)$$

p is the fraction of electrons per unit $d\Omega$ and unit solid angle. dn is the number of m-states in this range. This is found to be

$$dn=\frac{abc}{(2\pi)^3}d\kappa_1\,d\kappa_2\,d\kappa_3=\frac{abc}{(2\pi)^3}\sin\theta\kappa^2\,d\kappa\,d\theta\,d\phi$$

$$=\frac{abc}{(2\pi)^3}\frac{m}{\hbar}\kappa\sin\theta\,d\Omega\,d\theta\,d\phi. \quad . \quad . \quad (8)$$

In the second equation we have gone over to polar coordinates in the κ-space. In the third we have made use of the non-relativistic energy equation

$$\kappa^2=2mE/\hbar^2$$

and of

$$\Omega=(E_0-E_m)/\hbar=\hbar/2m(\kappa_0{}^2-\kappa_m{}^2)$$

hence

$$d\Omega=-(\hbar/m)\kappa\,d\kappa.$$

In the last eqn. (8) we can replace κ by κ_0 without appreciable error.

Combining eqns. (6) to (8) we obtain

$$p(\Omega,\theta,\phi)=\frac{abc}{(2\pi)^3}\frac{m}{\hbar}\kappa_0 c_m{}^*c_m$$

$$=\frac{abc}{(2\pi)^3}\frac{m}{\hbar}\left(\frac{e}{\hbar}\right)^2\left|\int_0^\tau\int_0^a\int_0^b\int_0^c\exp(-i\Omega t)\psi_m{}^*\phi\psi_0\,dt\,dx\,dy\,dz\right|^2. \quad (9)$$

This is a general formula for the energy and angular distribution of an electron beam which has interacted during a time τ with a potential field ϕ. We now assume that ϕ consists of a mixture of modes

$$\phi=\phi_n\cos(\pi n_1x/a)\cos(\pi n_2y/b)\cos(\pi n_3z/c)\exp(i\omega t) \quad . \quad . \quad (2)$$

with random phases, which are contained in the amplitude factors ϕ_n. That is to say, in the mean

$$\overline{\phi_n{}^*\phi_m}=0$$

if n and m stand for different sets of (n_1, n_2, n_3). Hence, carrying out the averaging process in eqn. (9), all cross-products will vanish, and the result is a sum over the single modes. A longish but elementary calculation gives

$$<\left|\int_0^\tau\int_0^a\int_0^b\int_0^c\exp(-i\Omega t)\psi_m{}^*\phi\psi_0\,dt\,dx\,dy\,dz\right|^2>$$

$$=\tau^2\sum_{n_1}\sum_{n_2}\sum_{n_3}\phi_n{}^*\phi_n[\omega][n_1][n_2][n_3] \quad . \quad . \quad . \quad . \quad . \quad . \quad (10)$$

where the square brackets are abbreviations for the following expressions

$$[\omega]=\left(\frac{\sin\frac{1}{2}(\Omega-\omega)\tau}{\frac{1}{2}(\Omega-\omega)\tau}\right)^2, \quad . \quad . \quad . \quad . \quad . \quad . \quad (11)$$

$$[n_1]=\left(\frac{\sin\frac{1}{2}[(\kappa_0-\kappa_1)a-\pi n_1]}{\frac{1}{2}[(\kappa_0-\kappa_1)a-\pi n_1]}\right)^2\left(\frac{(\kappa_0-\kappa_1)a}{(\kappa_0-\kappa_1)a+\pi n_1}\right)^2, \quad . \quad (12)$$

$$[n_2]=\left(\frac{\sin\frac{1}{2}(\kappa_2b-\pi n_2)}{\frac{1}{2}(\kappa_2b-\pi n_2)}\right)^2\left(\frac{\kappa_2b}{\kappa_2b+\pi n_2}\right)^2, \quad . \quad . \quad . \quad . \quad . \quad (13)$$

and similarly for $[n_3]$. The first of these expressions is the 'energy resonance bracket', the others are 'momentum resonance brackets'. The first factor in (12) and (13) is the resonance bracket for a travelling wave, the second arises from a wave travelling in the opposite direction, which together with the first produces a standing wave. It can be seen that when the first factor attains its maximum value, which is unity, the second factor is $\frac{1}{4}$. This arises from the fact that the effective part of the amplitude, corresponding to the first travelling wave, is one-half of the total, and the effect on the transition probability is one-quarter.

In order to complete eqn. (10) we now only require the mean values $\overline{\phi_n{}^*\phi_n}$. We obtain these from the consideration that in an electric wave, with wave number k, the electric field amplitude is k times the potential amplitude. The energy in the mode n is, in the mean, equal to the zero point energy $\frac{1}{2}\hbar\omega$, and this again is equal to the electrostatic energy stored at the instant of maximum field amplitude. Thus

$$\frac{abc}{8\pi}\,k^2\overline{\phi_n{}^*\phi_n}=\tfrac{1}{2}\hbar\omega(k) \quad . \; . \; . \; . \; . \; . \; . \; . \quad (14)$$

where k^2 is given by eqn. (3). Substituting this value into eqn. (10) we obtain finally

$$p(\Omega,\,\theta,\,\phi)=\frac{1}{2\pi^2}\,m\,\frac{e^2}{\hbar}\,\kappa_0\tau^2\sum_n\frac{\omega}{k^2}[\omega][n_1][n_2][n_3] \quad . \; . \quad (15)$$

where the summation is to be carried out over all the modes, from $n_1=n_2=n_3=1$ up to the cut-off.

§ 5. EVALUATION OF THE INTRAECTION PROBABILITY

Figure 1 illustrates in physical terms the mathematical problem involved in the summation (15). For any electron emerging with wave numbers κ_1, κ_2, κ_3 the maximum of the contribution will come from those terms of the sum-over-modes which are nearest to resonance, that is to say for which the conservation of energy and momentum is most nearly satisfied. (A standing wave carries no momentum as a whole, but one of its components, which was effective in the collision, does.)

Fig. 1

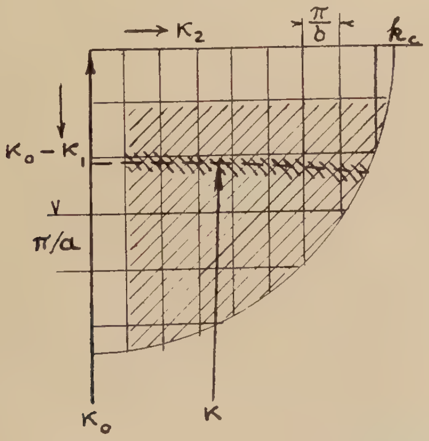

Momentum diagram in the XY-plane. Each lattice point corresponds to a mode. The hyperbolic regression line between the longitudinal and the transversal momentum arises from the combination of the conservation equations with the dispersion relation.

The momentum factors $[n_1]$, $[n_2]$ can be imagined as resonance functions centring on the lattice points n_1, n_2. In fact these resonance functions overlap sufficiently for making the discontinuous mode-structure all but unnoticeable. In addition to the momentum factors there is, however, also an energy resonance factor $[\omega]$, which has a maximum value where $\Omega=\omega(k)$. It has been pointed out independently by Mott,* by Watanabe and Kanazawa,† and by Ferrell† that if the energy and momentum conservation conditions were exactly satisfied this would result in a unique deflection angle θ for every loss Ω. This can be shown as follows :

Conservation of momentum gives

$$k^2=\kappa_0^2+\kappa^2-2\kappa_0\kappa\cos\theta=(\kappa_0-\kappa)^2+4\kappa_0\kappa\sin^2\tfrac{1}{2}\theta. \quad . \quad . \quad (16)$$

Conservation of energy gives, using the non-relativistic law

$$\kappa_0-\kappa \simeq (\kappa_0^2-\kappa^2)/2\kappa_0=\Omega/v. \quad . \quad . \quad . \quad . \quad . \quad (17)$$

Adding to these a dispersion relation, of the form

$$\omega^2=\omega_0^2+u^2k^2$$

putting $\Omega=\omega$ and combining the above equations we obtain

$$(\kappa_0\theta)^2=\kappa_t^2=k^2-\left(\frac{\Omega}{v}\right)^2=\left(\frac{1}{u^2}-\frac{1}{v^2}\right)\Omega^2-\frac{\omega_0^2}{u^2} \quad . \quad . \quad (18)$$

where we have written κ_t for the transversal wave number of the electron. This is a hyperbolic relation between the loss Ω and the deflection angle θ, which has been recently brilliantly confirmed by Watanabe,† giving, for Be, Al, Mg and Ge values of u^2 in remarkably good agreement with the value $u^2=\frac{6}{5}E_F/m$ derived by Pines (1954) for a free, degenerate electron gas.

In terms of wave numbers, using eqn. (17), this gives another hyperbola

$$\kappa_t^2=\left\{\frac{v^2}{u^2}-1\right\}(\kappa_0-\kappa)^2-\frac{\omega_0^2}{u^2} \quad . \quad . \quad . \quad . \quad . \quad . \quad (19)$$

which is shown in fig. 1. If the bombarding beam had an energy spread this hyperbola becomes a ‘ regression line ’, indicating the position of the mean energies. The energy distribution is, apart from the shift, the same at every angle θ and equal to the primary distribution.

These somewhat rough considerations, based on rigid conservation laws which need not be exactly satisfied in thin films, give some useful hints for simplifying the rather complicated sum in eqn. (15). Using eqn. (17) we write this sum in the form

$$\sum_n\frac{\omega}{k^2}\left(\frac{\sin\frac{1}{2}\{\Omega-\omega(k)\}\tau}{\frac{1}{2}\{\Omega-\omega(k)\}\tau}\right)^2\left(\frac{\sin\frac{1}{2}(\Omega\tau_e-\pi n_1)}{\frac{1}{2}(\Omega\tau_e-\pi n_1)}\right)^2\left(\frac{\Omega\tau_e}{\Omega\tau_e+\pi n_1}\right)^2[n_2][n_3] \quad . \quad (20)$$

where we have introduced the electron transit time $\tau_e=a/v$.

It can be seen immediately that the energy resonance (the first factor), is much sharper than the x-momentum resonance (the second factor), because in all thin films as used in experiments the wave transit time τ is many times larger than the electron transit time τ_e.

---

* Private communication.

† This information is taken from the article, still unpublished at the time of writing by D. Pines on ‘ Electron Interaction in Metals ’, to appear in *Advances in Solid State Physics*, Vol. I. Academic Press, New York, 1955.

On the other hand it can be shown that in terms of mode numbers n_1 the energy factor is much slower than the momentum factor, except for extremely thin films. If the mode number n_1 changes by unity, the argument of the sine in the second factor changes by $\frac{1}{2}\pi$, while in the first factor it changes by

$$\tfrac{1}{2}\frac{d\omega}{dk}\frac{dk}{dn}\tau=\tfrac{1}{2}\pi\frac{V_g\tau}{a}\frac{k_x}{k}.$$

We substitute here, using the free-gas dispersion relation

$$V_g=\tfrac{6}{5}(E_F/E_L)(\hbar/m)k,\quad \tau=\pi\hbar/kT\quad\text{and}\quad k_x=\Omega/v=E_L/\hbar v$$

which gives

$$\tfrac{1}{2}\frac{d\omega}{dk}\frac{dk}{dn}\tau=\tfrac{1}{2}\pi\frac{6}{5}\frac{e\hbar}{mckT}\frac{V_F}{\beta a}=\tfrac{1}{2}\pi\left(0{\cdot}85\times10^{-5}\frac{V_F}{\beta Ta}\right)$$

where V_F is the Fermi energy in volts. As an example, if $V_F=10$ v, $\beta=0{\cdot}197$ and $T=2500$°c, this gives

$$\tfrac{1}{2}\pi(1{\cdot}72\times10^{-7}/a).$$

That is to say the energy resonance becomes as sharp as the momentum resonance in terms of the mode number n_1 only at thicknesses a of 17 ångström. Thus for thicknesses of more than 30–60 Å *we are justified in considering* $[\omega]$ *as a slow factor*, and to put it before the summation sign in eqn. (15). This means that for all except very thin films the energy distribution will be the same as the primary distribution, except for a shift as calculated from eqn. (18), which is a function of the angle θ. (The sum will still contain Ω, but will be extremely insensitive compared with the factor before the sum.)

For very thin films a more accurate calculation would be needed, but this is hardly worth while because it would be extremely difficult to check experimentally the slight departures of energy distribution in function of the angle θ which it entails. Moreover, these small effects vanish altogether in the integrated probability, because $[\omega]$ is so much sharper than the rest in terms of Ω, especially for thin films.

Putting $[\omega]$ before the summation sign, we are left with

$$\Sigma\left[\omega_0\Big/\left\{\pi^2\left(\frac{n_1^2}{a^2}+\frac{n_2^2}{b^2}+\frac{n_3^2}{c^2}\right)\right\}\right]\left(\frac{\sin\frac{1}{2}(\omega_0\tau_e-\pi n_1)}{\frac{1}{2}(\omega_0\tau_e-\pi n_1)}\right)^2\left(\frac{\omega_0\tau_e}{\omega_0\tau_e+\pi n_1}\right)^2[n_2][n_3]. \quad . \quad . \quad . \quad (21)$$

Here we have replaced ω in the first factor and Ω in the next two by ω_0, as this makes no significant difference.

Consider now the angular distribution. This is entirely contained in the factors $[n_2]$ and $[n_3]$ as only these contain κ_2 and κ_3. We can however simplify matters by replacing the first factor under the sum by

$$\frac{\omega_0}{(\pi n_1/a)^2+\kappa_2^2+\kappa_3^2}$$

that is to say replacing the transverse mode numbers n_2, n_3 by their resonance values. This again is a slow factor, and can be put before the summation signs of the sums in n_2 and n_3. We are now left with

$$\left(\sum_{n_1}\frac{\omega_0}{(\pi n_1/a)^2+\kappa_2{}^2+\kappa_3{}^2}\left[\frac{\sin\frac{1}{2}(\omega_0\tau_e-\pi n_1)}{\frac{1}{2}(\omega_0\tau_e-\pi n_1)}\,\frac{\omega_0\tau_e}{\omega_0\tau_e+\pi n_1}\right]^2\right)\Big(\sum_{n_2}[n_2]\Big)\Big(\sum_{n_3}[n_3]\Big) \quad . \quad . \quad . \quad (22)$$

which is the product of three sums. The last two can be written in the form

$$\Sigma[n_2]=F(\kappa_2 b/\pi), \qquad \Sigma[n_3]=F(\kappa_3 c/\pi) \quad . \quad . \quad . \quad (23)$$

in terms of the function

$$F(x)=\sum_{n=1}^{N}\left(\frac{\sin\frac{1}{2}\pi(x-n)}{\frac{1}{2}\pi(x-n)}\right)^2\left(\frac{x}{x+n}\right)^2. \quad . \quad . \quad . \quad . \quad . \quad (24)$$

This function is illustrated in fig. 2. It starts at zero for $x=0$, rises rapidly near $x=1$ and attains a maximum of 0·5 at $x=2$. It then approaches, with insignificant fluctuations, the asymptotic value 0·481.

Fig. 2

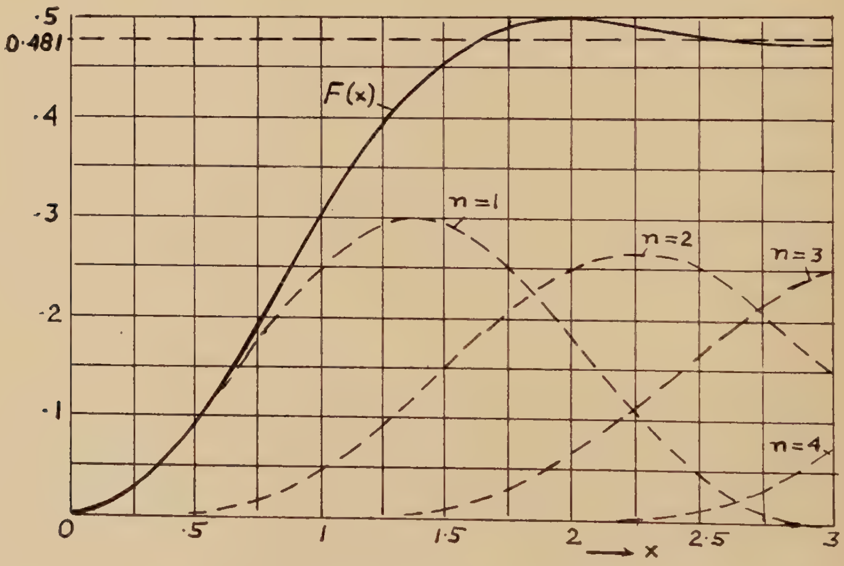

The function $F(x)$ and its components.

It might appear from this that the polar diagram falls to zero at zero angle θ, moreover that there is a cross-shaped gap in it at $\phi=0$ and $\phi=\frac{1}{2}\pi$, parallel to the axes. But these are just covered up by the diffraction which we have neglected when representing the emerging electron by a plane wave, instead of a wave-bundle which has zero value outside b, c. It is therefore more accurate to substitute in the eqn. (22) the asymptotic value 0·481 of $F(x)$, up to the cut-off, and it is seen that the angular and energy distribution is given by a sum of terms of the form

$$\frac{[\omega]}{(\pi n_1/a)^2+(\kappa_0\theta)^2}. \quad . \quad . \quad . \quad . \quad . \quad . \quad . \quad (25)$$

For films which are not too thin one can moreover replace $(\pi n_1/a)$ by the constant value Ω/v, which follows from the X-momentum resonance (cf. Ferrell 1955). This is illustrated in fig. 3. It appears that this type of angular distribution is in good agreement with experiments.

We now calculate the integrated, total probability of excitation, P. The energy dependence is contained in the $[\omega]$ factor, and this is so sharp that we can integrate between infinite limits, using the formula

$$\int_{-\infty}^{\infty}[\omega]\,d\Omega=\int_{-\infty}^{\infty}\left(\frac{\sin\frac{1}{2}(\Omega-\omega)\tau}{\frac{1}{2}(\Omega-\omega)\tau}\right)^2 d\Omega=\frac{1}{2}\frac{\pi}{\tau}\quad . \quad . \quad . \quad (26)$$

Integration of the angular factor 25 over all directions, up to the cut-off gives

$$2\pi\int_0^{(k_c)}\frac{\theta\,d\theta}{(\pi n_1/a)^2+\kappa_t^2}=\frac{2\pi}{\kappa_0^2}\int\frac{\kappa_t\,d\kappa_t}{(\pi n_1/a)^2+\kappa_t^2}=\frac{\pi}{\kappa_0^2}\log\left(\frac{k_c}{\pi n_1/a}\right)\quad . \quad (27)$$

Fig. 3

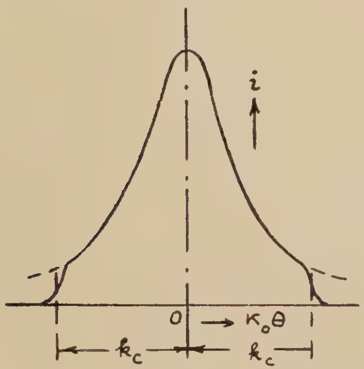

Angular distribution of the current density i per unit solid angle.

Here we have integrated up to a maximum wave number k_c starting from zero transverse wave number, in accordance with the remark made above that diffraction makes the drop-out of the modes $n_2=0$ and $n_3=0$ unnoticeable.

Collecting all factors, from eqn. (15) on, we have now

$$P=\iiint p(\Omega,\theta,\phi)\,d\Omega\theta\,d\theta\,d\phi=\frac{(0{\cdot}481)^2}{4\pi}\left(\frac{c}{v}\right)(\omega_0\tau)\left(\frac{e^2}{\hbar c}\right)$$
$$\times\sum_{n_1}\left(\frac{\sin\frac{1}{2}(\omega_0\tau_e-\pi n_1)}{\frac{1}{2}(\omega_0\tau_e-\pi n_1)}\,\frac{\omega_0\tau_e}{\omega_0\tau_e+\pi n_1}\right)^2\log\left(\frac{k_c a}{\pi n_1}\right)\quad . \quad . \quad . \quad . \quad . \quad . \quad (28)$$

where we have substituted $\kappa_0=mv/\hbar$. In the last remaining sum we now introduce the new variable

$$x=\omega_0\tau_e/\pi=\omega_0 a/\pi v=a/a_\pi.\quad . \quad . \quad . \quad . \quad . \quad (29)$$

This is a very convenient measure of the thickness, in units of the thickness a_π in which the electron 'sees' just half a cycle of ω_0. This is

$$a_\pi = \pi v/\omega_0 = \pi\beta c\hbar/eV_L = 6{\cdot}12\times10^{-5}\beta/V_L \text{ cm} \quad . \; . \; . \; . \quad (30)$$

where V_L is the characteristic loss in volts. For 10 kev electrons, $\beta = 0{\cdot}197$ and aluminium, $V_L = 14{\cdot}7$ v, this gives $a_\pi = 80$ Å.

We now introduce the function

$$G(x) = \sum_{n=1}^{N} \log n \left(\frac{\sin\frac{1}{2}(x-n)}{\frac{1}{2}(x-n)} \, \frac{x}{x+n} \right)^2 \quad . \; . \; . \; . \; . \quad (31)$$

which is illustrated in fig. 4. In terms of this function and the previously defined $F(x)$ (eqn. (24)), we can now write the last sum in eqn. (28) in the form

$$\Sigma[n_1] \log\left(\frac{k_c a}{\pi n_1}\right) = Q\left(\frac{a_\pi}{\frac{1}{2}\lambda_c}, \frac{a}{a_\pi}\right)$$

$$= \log\left(\frac{a_\pi}{\frac{1}{2}\lambda_c}\right) F\left(\frac{a}{a_\pi}\right) - G\left(\frac{a}{a_\pi}\right) + \log\frac{a}{a_\pi}\Big) F\left(\frac{a}{a_\pi}\right). \quad (32)$$

Fig. 4

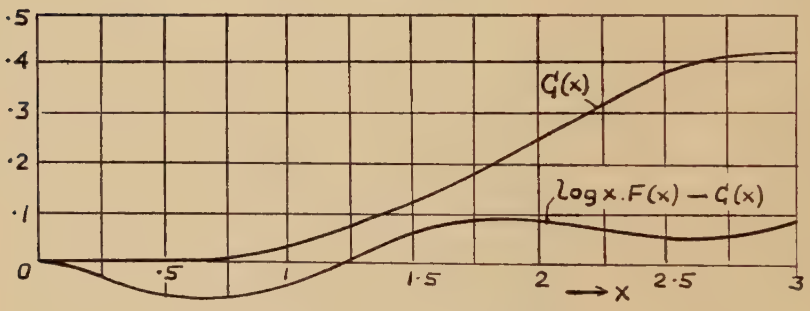

The functions $F(x)$ and $\log xF(x) - G(x)$.

The function $\log xF(x) - G(x)$ is also illustrated in fig. 4. It goes asymptotically to zero after one negative and one positive excursion.

Our final result is, therefore, *for coherently illuminated grains*

$$P = \frac{(0{\cdot}481)^2}{4\pi} \, \frac{1}{137} \left(\frac{c}{v}\right) (\omega_0 \tau) Q\left(\frac{a_\pi}{\frac{1}{2}\lambda_c}, \frac{a}{a_\pi}\right) \quad . \; . \; . \; . \quad (33)$$

where we have used $\hbar c/e^2 = 137$. Instead of the cut-off wave number k_c we have used the corresponding critical wavelength $\lambda_c = 2\pi/k_c$. The function Q is illustrated in fig. 5.

It is seen that the cross section or collision probability for a collective interaction behaves indeed very differently from the corresponding quantity in an atomic process. Instead of being linear in function of the thickness a, it starts first very flat, and then approaches rapidly a constant asymptotic value which it overshoots slightly at $2a_\pi$. This asymptotic value is

$$P_\infty = \frac{(0{\cdot}481)^3}{4\pi}\,\frac{1}{137}\left(\frac{c}{v}\right)(\omega_0\tau)\log\left(a_\pi/\tfrac{1}{2}\lambda_c\right) = 6{\cdot}5\times10^{-5}\,\frac{\omega_0\tau}{\beta}\log\left(a_\pi/\tfrac{1}{2}\lambda_c\right). \quad (34)$$

where we must substitute

$$\omega_0\tau = \pi e V_L/kT = \pi\ 11\,600\ V_L/T. \quad . \quad . \quad . \quad . \quad . \quad . \quad (35)$$

As an example take aluminium. The maximum deflection angle θ, which can be roughly identified with the cut-off, observed by Watanabe with 25 kev electrons was $1{\cdot}2\times10^{-2}$. This corresponds to $\lambda_c=9$ Å. With $V_L=14{\cdot}7$ v and a tungsten cathode $\omega_0\tau=214$. This gives for

$V=10$ kv, $\beta=0{\cdot}197$, $a_\pi=80$ Å, $P=0{\cdot}204$,

$V=25$ kv, $\beta=0{\cdot}304$, $a_\pi=126$ Å, $P=0{\cdot}148$.

Fig. 5

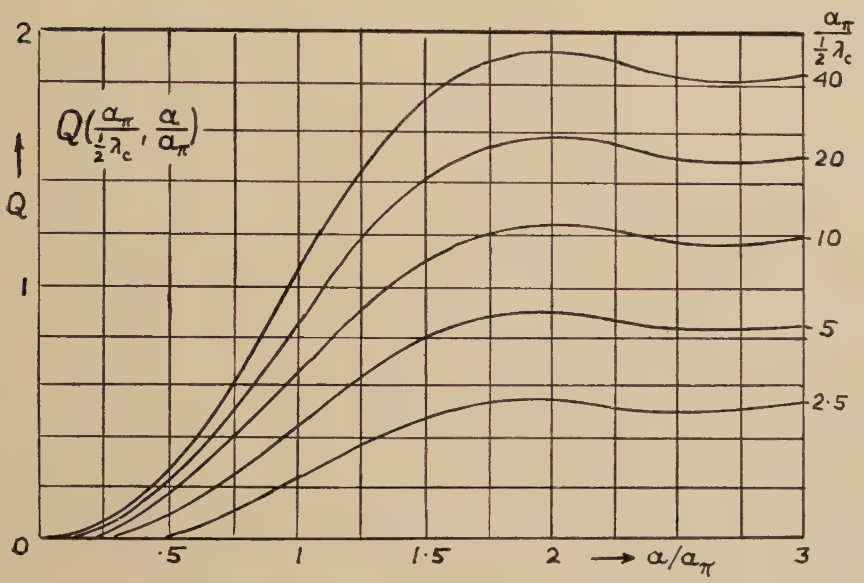

The collision probability function Q, in function of the thickness and of the cut-off wavelength λ_c.

Before discussing this and other consequences of eqn. (33), we calculate the corresponding quantities for incoherent illumination.

§ 6. INTERACTION WITH GRAINS SIGNIFICANTLY LARGER THAN THE COHERENCE WIDTH

In this case we have essentially incoherent illumination. As explained in § 3, each elementary excitation process produces travelling waves of the type as in eqn. (5). Nothing changes in the previous calculation up to eqn. (13), which we must now replace by

$$[n_2]' = \left(\frac{\sin \frac{1}{2}(\kappa_2 b - 2\pi n_2)}{\frac{1}{2}(\kappa_2 b - 2\pi n_2)}\right)^2 \quad . \quad . \quad . \quad . \quad . \quad . \quad (13')$$

and correspondingly eqn. (24) must be replaced by

$$F'(x) = \sum_{-N}^{N} \left(\frac{\sin \frac{1}{2}\pi(x-2n)}{\frac{1}{2}\pi(x-2n)}\right)^2 . \quad . \quad . \quad . \quad . \quad . \quad . \quad (24')$$

But this function is exactly unity, independently of x, if N goes to infinity, and if N is finite it is still appreciably unity for $-N<x<N$ and zero outside. Hence in the incoherent case nothing is changed in the energy or angular distribution, but the previous factors 0·481 in eqn. (33) must now be replaced by unity. This means that in the case of incoherent illumination *the probabilities* P and P_x in eqns. (33) and (34) *must be multiplied by* $1/0{\cdot}481^2 = 4{\cdot}32$.

§ 7. COMPARISON WITH THE EXPERIMENTS OF GABOR AND JULL

In these experiments, which have been only partly published so far (Gabor and Jull 1955), ‘ stratified ’ layers of metals were built up of thin layers, with some foreign material between. In one experiment for instance six layers of gold of 25–30 Å each were evaporated on top of one another, with thin layers of perhaps 10–20 Å of ‘ carbonaceous contamination ’ between, which are easily produced in any continuously evacuated system by electron bombardment, which cracks the oil and grease molecules which are always present in the residual gas. It was found that the 16 ev gold line was just perceptible in the layer with six strata equivalent to 170 Å of solid gold ; about an order of magnitude weaker than in a solid gold layer of 110 Å thickness.

These experiments undoubtedly indicate that the initial rise of P is stronger than linear, the difficulty is only that *the evidence is too strong*. For 10 kev electrons, as used by Gabor and Jull, and $V_L = 16$ v, a_π is about 75 Å hence the six layers correspond to about $x = 0{\cdot}38$ each, while the single gold layer of 110 Å corresponds to $x = 1{\cdot}5$. As seen in fig. 5, such a strong effect could be expected only if $a_\pi/\frac{1}{2}\lambda_c$ were about 2·5, which corresponds to a cut-off wavelength of about 60 Å. The first interpretation put forward by Gabor and Jull was, accordingly, that the critical wavelength must be much longer than expected on the basis of the theory of Pines and Bohm. In view of the experiments of Watanabe, which indicate cut-off wavelengths of rather less than 10 Å we must now explore alternative explanations.

One possibility suggested by the foregoing theory is that perhaps the grain size in the 25–30 Å gold films was much smaller than that in the foil of 110 Å so that the first were coherently illuminated and the other incoherently. If this were the case, one could just reconcile the experiments with a cut-off wavelength of about 10 Å. This would approximately correspond to a curve for $a_\pi/\frac{1}{2}\lambda_c=15$ in fig. 5. This gives $Q=0{\cdot}10$ for $x=0{\cdot}38$ and $Q=1{\cdot}27$ for $x=1{\cdot}5$. Hence six layers of $x=0{\cdot}38$ would give an effect of 0·61, but if the solid foil was incoherently illuminated this would have to be compared with $4{\cdot}32\times1{\cdot}27=5{\cdot}5$, which is nine times stronger. But this explanation does not agree with direct observations of the grain size in electron micrographs and in diffraction diagrams. The electron micrographs showed indeed that the granules of the stratified layer were smaller, but they were still of the order 1000 Å which is much more than the coherence width used in these experiments. Electron diffraction diagrams even indicated that the stratified layers were better crystallized, which is quite likely in view of their more prolonged bombardment. It appears therefore that this interpretation must be dropped.

There remains only one likely explanation, and this is that it is too naive to think of layers of the order 25–30 Å thickness as if they had the properties of matter in bulk, as regards collective oscillations. If one imagines that there is on the surface of the metal foils *a 'disturbed' surface layer of only* 3–4 *atomic layers thickness*, so that the standing waves have these as boundary, this would mean that we have to consider the effective thickness of these layers as perhaps 15–20 Å less than the nominal thickness and the experiments are readily explained.

§ 8. CONCLUSIONS. NEW CRUCIAL TESTS

Consider again eqn. (33) for the probability of exciting the first-order characteristic loss

$$P=\frac{0{\cdot}65\times10^{-4}}{2{\cdot}80\times10^{-4}}\left(\frac{c}{v}\right)(\omega_0\tau)\,Q\left(\frac{a\pi}{\frac{1}{2}\lambda_c},\frac{a}{a_\pi}\right)\begin{matrix}\text{incoherent}\\\text{coherent}\end{matrix}\ \text{illumination.} \quad . \quad (36)$$

This function has so many features in which it differs from the probability of exciting single-electron transitions, that it ought to be possible to decide about the 'collective' or 'single-electron' nature of any characteristic loss beyond a doubt. We have already discussed the non-linear start for small thicknesses. Another striking feature is the asymptotic value of P, which is reached at about $a=2a_\pi$, that is to say at a thickness of the order 100–150 Å under usual experimental conditions. This is easily understood. Once the thickness is of this order, any single collision act will excite significantly 2–3 modes in the X-direction. This number remains constant if the thickness is increased; the momentum resonance becomes sharper instead of stronger. The reason is that the interaction time is determined by the train length instead of by the foil thickness.

We have seen that P_∞ for coherent illumination is of the order 0·15–0·2, while for incoherent irradiation it is of the order unity. In this case of course first-order perturbation theory is no longer accurate. In reality P would increase, once it has reached appreciable values, slower than the Q-function, because the primary electrons are used up, nor would it go beyond about 0·5 because 2d, 3d, . . . order transitions would become important. From the fact that some experimenters have observed simultaneously lines of five orders in Al, we must infer that in these experiments the illumination was incoherent.

The eqn. (36) suggests two crucial tests. The first arises from the factor $\omega_0\tau$ which is inversely proportional to the primary energy-spread, i.e. to the temperature of the cathode. With an oxide cathode, $T=1000°$, P should be 2·5 times stronger than with a tungsten cathode, $T=2500°$. This means that, using the same foil, weaker lines, if they are due to collective interaction, should be increased in intensity 2·5 times, while in the case of stronger lines the higher orders should increase very noticeably. It appears that all experimenters have used tungsten cathodes, as is usual in demountable vacuum devices. If the hypothesis of collective interaction is right, it ought to be possible, using oxide cathodes or some other methods of producing electron beams of more uniform energy, to produce the collective part of the loss-spectrum *almost pure, much stronger than hitherto observed*, and to separate it from loss-lines of other origin.

A second crucial test is suggested by the large difference between P for coherent and for incoherent illumination. Most experimenters have probably operated with rather large grains (well-crystallized foils), and not too well collimated electron beams. With grains of the order of a few hundred ångströms it ought to be possible to notice a strong diminution of the characteristic losses of collective origin if one passes from, say, critical illumination to a well-collimated beam, with divergences of less than 10^{-4} radian.

It may be noted that this theory and the proposed crucial tests apply only to *sharp lines*. This is the consequence of our assumption that the collective oscillations are undamped, up to the critical wave number, where they are suddenly cut off. If they are appreciably damped, as is probably the case in insulators, and also in most heavy metals, the theory must be revised, introducing complex values of ω, to account for the broad lines observed in many experiments.

REFERENCES

Ferrell, R., 1955, *Bull. Amer. Phys. Soc.*, **30,** No. 3, Abstract R 10.
Fröhlich, H., and Pelzer, H., 1955, *Proc. Phys. Soc.* A, **68,** 525.
Gabor, D., and Jull, G. W., 1955, *Nature, Lond.*, **175,** 718.
Hubbard, J., 1955, *Proc. Phys. Soc.* A, **68,** 441.
Pines, D., 1954, *Phys. Rev.*, **92,** 1954.
Pines, D., and Bohm, D., 1952, *Phys. Rev.*, **85,** 338.

APPENDIX

THE EQUIVALENT TRAIN LENGTH OF ELECTRONS EMITTED BY A HOT CATHODE

If v_0 is the initial velocity of the electrons in the x-direction, the current in the limits v_0, dv_0 is, at the cathode, proportional to

$$\exp\left(-\tfrac{1}{2}mv_0^2/kT\right)v_0\,dv_0.$$

Adding an energy E_0, corresponding to a voltage drop E_0/e, the energy distribution in the beam current becomes

$$\exp\left[-(E-E_0)/kT\right] dE.$$

The mean energy of the electrons in the beam is E_0+kT. This distribution is shown in fig. 6.

Compare this with the energy distribution corresponding to a chopped wave train of frequency ω_0 and duration τ. To obtain this we need only calculate the absolute square of its Fourier transform, going over to energies by $E=\hbar\omega$. This gives

$$\left(\frac{\sin\left\{\frac{1}{2}(\omega-\omega_0)\tau\right\}}{\frac{1}{2}(\omega-\omega_0)\tau}\right)^2=\left(\frac{\sin\left\{\frac{1}{2}(E-E_0-kT)\tau/\hbar\right\}}{\frac{1}{2}(E-E_0-kT)\tau/\hbar}\right)^2$$

where we have identified $\omega_0\hbar$ with E_0+kT. Figure 6 shows this distribution for three values of τ, $\frac{1}{2}\pi\hbar/kT$, $\omega\hbar/kT$ and $2\pi\hbar/kT$.

Fig. 6

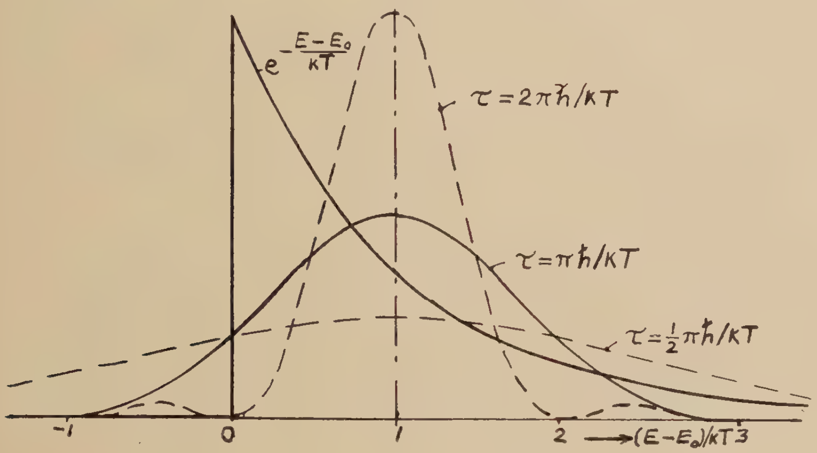

Energy distribution in an electron beam emitted by a hot cathode, compared with three chopped monokinetic pulses of different durations. All areas are equal.

In order to make the best choice we make the comparison in yet another way, by comparing the chopped monochromatic train with the 'time-representation' of an electron beam with Maxwellian probability distribution. We obtain this formally by taking the square root of the Maxwellian density in E, and then taking the absolute square of its Fourier transform, which is of the form

$$\frac{1}{1+(2kTt/\hbar)^2}.$$

The physical meaning of this formal representation is that the electron beam issuing from a hot cathode of temperature T could not be distinguished from a source which emits probability pulses of this shape. This pulse shape is compared with chopped pulses of durations $\tau = \frac{1}{2}\pi\hbar/kT$, $\pi\hbar/kT$ and $2\pi\hbar/kT$ in fig. 7.

Fig. 7

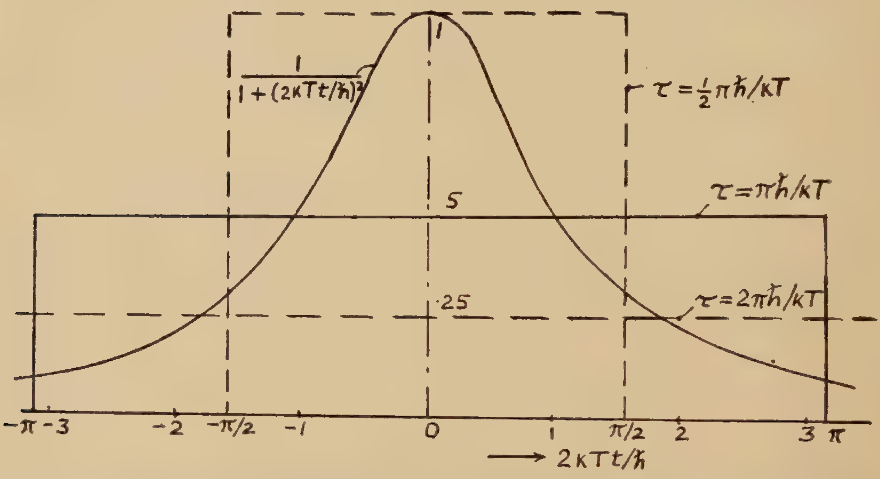

The probability pulse corresponding to a Maxwellian beam, in time representation, compared with three chopped waves of different durations. All areas are equal.

Testing the fit by the rule of least squares in both representations, the conclusion is that $\tau = \pi\hbar/kT$ is the best compromise. The energy representation appears to favour slightly larger values, while the time representation favours smaller ones. The compromise solution $\tau = \pi\hbar/kT$ has been adopted in the text.

II. *The Optical Model Applied to the Elastic Scattering of Nucleons by Various Light Nuclei*

By E. J. Burge,* Y. Fujimoto† and A. Hossain‡
H. H. Wills Physical Laboratory, University of Bristol §

[Received September 14, 1955]

Summary

The Optical Model of the nucleus has been applied to the elastic scattering of 9·5 Mev protons by He, C, N, O, F, Ne and A, and 14 Mev neutrons by C, N and O. In general, fair agreement has been obtained for a square-well potential, but the results suggest that for higher energies and heavier nuclei a shaping of the well is necessary. By making the nuclear radius a variable parameter, instead of $1{\cdot}45 \times A^{1/3} \times 10^{-13}$ cm, better agreement could probably be obtained. The mean free path of nucleons of these energies in nuclear matter is found to be larger than the nuclear radius. No simple relation was found between the depth of the potential-well and the atomic weight.

§ 1. Introduction

The Optical Model of the nucleus (see e.g. Feshbach *et al.* 1954) attempts to reconcile the independent-particle model with the strong-interaction model. At the same time, it allows the scattering of a proton or neutron by a nucleus to be treated as a two-body problem. The nucleus is represented by a potential-well of complex depth, and of radius R, such that in the simplest case of a square well

$$V = -(V_0 + iW_0), \text{ for } r < R.$$

The Coulomb effect for protons is represented by

$$V = Ze^2/r, \text{ for } r > R.$$

It has been shown by Chase and Rohrlich (1954) that the square-well potential cannot give a good fit to the angular distribution of 18 Mev protons elastically scattered from aluminium. They conclude that agreement may be better for nuclei with smaller Z. However, the work of Britten (1952) had already demonstrated that this simple theory does not fit for beryllium bombarded by 31·5 Mev protons. It appeared therefore that an application of the theory to the scattering of lower energy protons (9·5 MeV) by the lighter nuclei would be of interest. At this energy, the wavelength of the incident nucleons is of the same order as the radius of the nucleus and therefore the effect of the edge is not so serious as it is for higher energies. Also the calculations are somewhat easier, especially in the absence of an electronic calculating machine, since only a few values of L (usually $L=0 \rightarrow 4$) are significant.

---

* Now at The Wheatstone Laboratory, King's College, University of London.

† On leave of absence from the University of Kyoto.

‡ Now at the University of Dacca.

§ Communicated by Professor C. F. Powell, F.R.S.

For reasons given by Adair (1954) from low energy neutron data, the expected value of V_0 is in the region of 42 MeV. Feshbach *et al.* (1954) give theoretical curves of differential cross sections for 1 MeV neutrons elastically scattered from elements of $A=40$ to $A=260$. They use $V=-42(1+i0{\cdot}03)$, and the agreement is, in general, remarkably good.

A two-body interaction model leads to a more accurate representation of the scattering of nucleons by even nuclei than by odd nuclei. With the exception of nitrogen and fluorine, the elements studied here are even–even. It is of considerable interest, therefore, to compare the results of the application of the Optical Model to these two nuclei (N, F) with those obtained for the other nuclei. We can expect a small value of W_0 for even nuclei, which have few low lying levels.

§ 2. APPLICATION TO OXYGEN

Oxygen is a closed shell even–even nucleus and it was for this element that the properties mentioned above were demonstrated experimentally. Thus it has been shown (Ajzenberg and Lauritsen 1952) that the value of the reduced width indicates the validity of the two-body model for low energies. The value of the resonant energy (E_r) for neutrons can be related to the radius R and potential V_0 of a square well by the equation, $E_r=-(V_0+E_r)\cot^2(k'R)$, where $k'=\sqrt{2M(V_0+E_r)}$ since only waves of $L=0$ are involved. This gives, for $R=3{\cdot}65\times10^{-13}$ cm, the value $V_0=42$ MeV. At higher energies, however, other values of L are involved. Hence the criteria for fit allow, in principle, a less ambiguous assignment of V and R. On the other hand, this is complicated by the introduction of W_0, which in the case of oxygen is conveniently small. In an earlier communication (Fujimoto and Hossain 1955) some of the results for oxygen were reported. This element was chosen for the reasons given above for an extended study of the variation of the differential cross section curve with the three parameters; R the radius of the nucleus, and V_0 and W_0 which determine the complex potential $V=-(V_0+iW_0)$.

The expression given by Blatt and Weisskopf (p. 336) can be easily rearranged using the same notation to give the more convenient form

$$\frac{d\sigma(\phi)}{d\Omega}=\left[\frac{Ze^2}{Mv^2}\operatorname{cosec}^2(\phi/2)-\frac{1}{k}\sum_{L=0}^{\infty}(2L+1)\cos\psi_L\sin\delta_L P_L(\cos\phi)\right]^2$$

$$-\frac{1}{k^2}\left[\sum_{L=0}^{\infty}(2L+1)\sin\psi_L\sin\delta_L P_L(\cos\phi)\right]^2,$$

where $$\psi_L=2(\sigma_L-\sigma_0)+\delta_L+2\gamma\log_e(\sin\phi/2).$$

The value of R for the present calculations was given by $R = r_0 A^{1/3} \times 10^{-13}$ cm, where A=Mass Number. Following Feshbach *et al.* (1954) the value of r_0 was taken as 1·45 giving $R = 3{\cdot}65 \times 10^{-13}$ cm for oxygen. The contributions from terms involving $L \geqslant 4$ were shown to be negligible in the case of oxygen. It was found that the shape of the curve depended critically on the value of V_0 as shown in fig. 1. As V_0 was varied from 32 to 42 Mev with $W_0 = 0$ the shape showed a marked change at $V_0 = 38$ Mev. This was occasioned by the magnitude and sign of the f-wave ($L = 3$) component near $\phi = 70°$ which first cancelled out the other terms for $V_0 \approx 36$, and then at $V_0 = 38$ swamped the $L = 0, 1, 2$ contributions and produced a subsidiary maximum.

Fig. 1

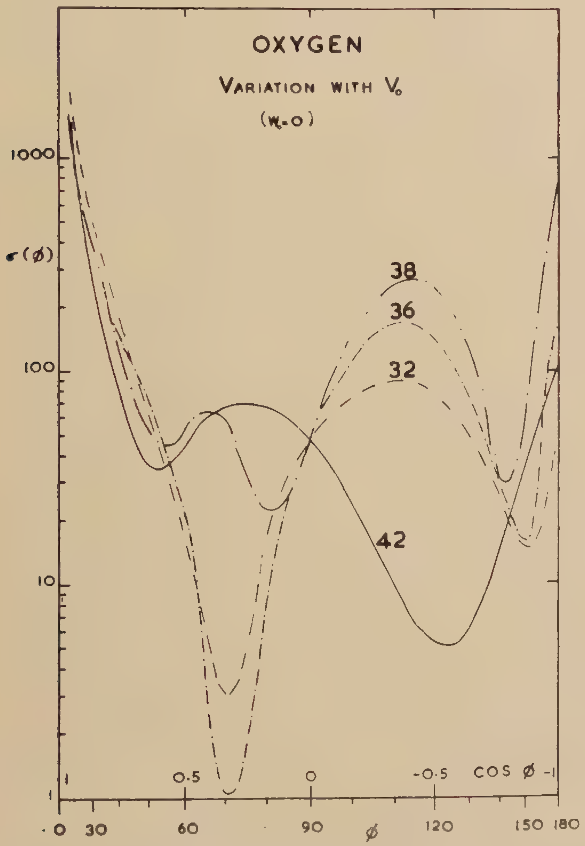

Theoretical proton scattering curves. $\sigma(\phi)$ is in mB/steradian and ϕ is the c.m.s. angle (as for all figures).

This rather complicated behaviour is also presented by other elements for certain values of R, V_0 and W_0 (cf. fig. 5, for nitrogen). However, in attempts to fit the experimental results, this leads to no real difficulty. Preliminary values, for neon in particular, sometimes gave curves near an anomalous region.

The introduction of W_0 tends to flatten the curves, in the sense that it increases $\sigma(\phi)$ at the first minimum and reduces the first maximum. With the exception of near-critical values of V_0 it does not alter very much the positions of the first minimum and maximum. This was found to be true for all the elements studied, and the curves for nitrogen (fig. 5) show both the typical and the anomalous dependence on W_0.

Two criteria were found to be useful for determining the 'best' fit. The angular position of the first interference minimum was adjusted by suitable variation of V_0. In most cases this also served to locate the first maximum at approximately the correct value of ϕ. The other criterion was the value of $\sigma(\phi)$ at the first maximum and this could usually be obtained by adjusting W_0, remembering that increasing W_0 was always found to lower $\sigma(\phi)$ at this maximum. It was expected that the departure from the experimental values would be greatest for the higher values of ϕ. This justified the relative neglect of the position and absolute value of the second minimum.

The theoretical curves giving the closest fit for oxygen are shown in fig. 2; the experimental points are from Burcham *et al.* (1953), with certain additions communicated privately. The curve for $V=-(42+i0)$ is also shown because of the importance of this value of V_0 in the interpretation of neutron data at 1 Mev. There is a series of values of V_0 from 30 to 36 Mev, with a suitable value of W_0 from 1 to 2 Mev, giving curves in very fair agreement with experiment. The values near $V_0=36$ Mev give a slightly better value of ϕ for the first minimum. The absolute value of $\sigma(\phi)$ in this region could most probably be improved by tedious adjustments of V_0 and W_0, since V_0 is becoming very critical. As already indicated, at $V_0=36$ Mev the maximum contribution to the scattering comes from proton waves of angular momentum $L=3$. This suggests that the states of ^{17}F near 10 Mev are predominantly *f*-states and hence have spins of 5/2 or 7/2, thereby showing that the one-particle model is in this case a sufficiently good approximation for explaining the energy states concerned.

The application of the Optical Model to the elastic scattering of 14·1 Mev neutrons by oxygen, as already reported (Fujimoto and Hossain 1955) showed that the values $V=-(32+i7)$ and $V=-(36+i5)$ give a fairly good fit to both the differential and total cross-sections. However, the experimental results (Conner 1953) for the differential cross sections are, as yet, insufficiently precise to distinguish between the possible values of V. The values of total cross section are of greater interest. As shown in table 1, the value $V=-(32+i8)$ gives the better ratio of the absorption and elastic cross sections for a total cross section equal to that obtained experimentally (1·6 barns). Nevertheless, the ratio (0·70) is not in good agreement with the experimental value (1·28). The best ratio for $V_0=$ 42 Mev gives a poor value of total cross section, but still a tolerably good fit to the angular distribution. This value, $V_0=42$ Mev, is of further interest in that it gives a bound 2 s state for ^{17}O at a binding energy, for

Fig. 2

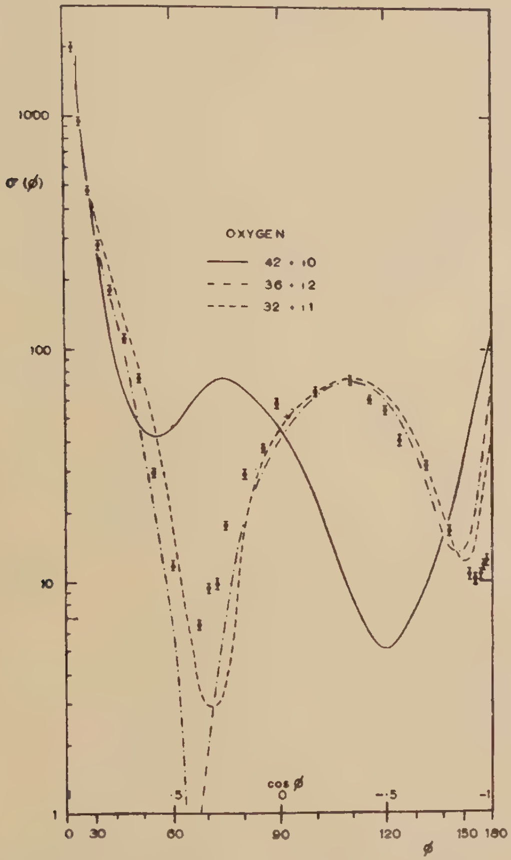

Experimental points and theoretical curves for 9·5 MEV protons elastically scattered by oxygen.

Table 1. Cross sections for the Scattering of 14 MEV Neutrons by Oxygen (in barns)

Square-Well Potential (MEV)	Elastic Scattering cross section	Absorption cross section	Total cross section
$30+i5$	1·21	0·59	1·80
$32+i2$	1·68	0·43	2·11
$32+i5$	1·16	0·61	1·77
$32+i6$	1·08	0·63	1·71
$32+i8$	0·93	0·66	1·59
$36+i5$	1·01	0·54	1·55
$36+i6$	0·96	0·58	1·54
$40+i5$	0·70	0·44	1·14
$42+i5$	0·73	0·45	1·17
$42+i8$	0·66	0·59	1·25
Experimental	0·7	0·9	1·6

the well known 0·875 MeV level, of 3·23 MeV in exact agreement with the experimental value.

The effect of varying V_0 or W_0 can be seen from the tables. General rules can easily be drawn up, but certain exceptions have been found.

§ 3. Carbon

Using the same criteria of fit for protons elastically scattered from carbon, it was found that a square-well potential with $V_0 \approx 44$ MeV and $W_0 \approx 4$ MeV gave the best results (fig. 3). In this case $V_0 = 42$ MeV is a tolerably good fit, but the position of the first minimum suggests that higher values of V_0 may give a better fit. The curves are for $L \leqslant 3$, higher values of L making negligible contributions. The experimental points given here are those of Burcham *et al.* (1953) with certain additions communicated privately. The results of Fischer (1954) have been compared and found to give a somewhat smaller cross section. For $\phi > 60°$ they are well fitted by $V = -(42 + i6{\cdot}3)$, but for $\phi < 60°$ the experimental values of $\sigma(\phi)$ are rather low.

Fig. 3

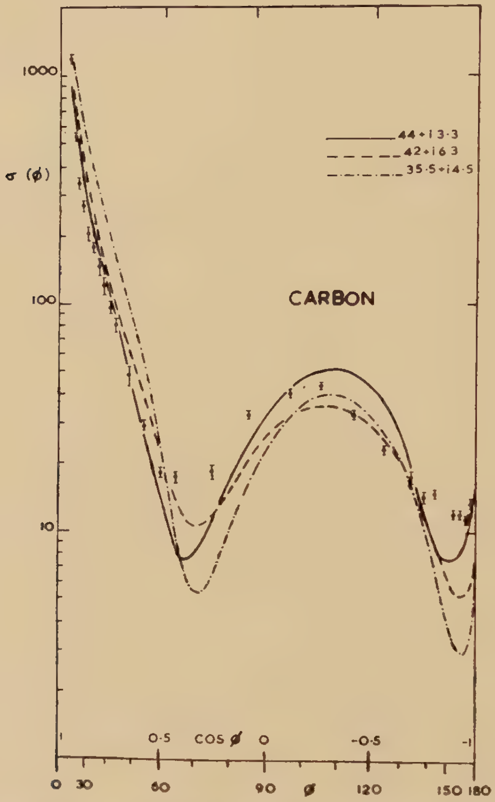

Experimental points and theoretical curves for 9·5 MeV protons elastically scattered by carbon.

Fig. 4

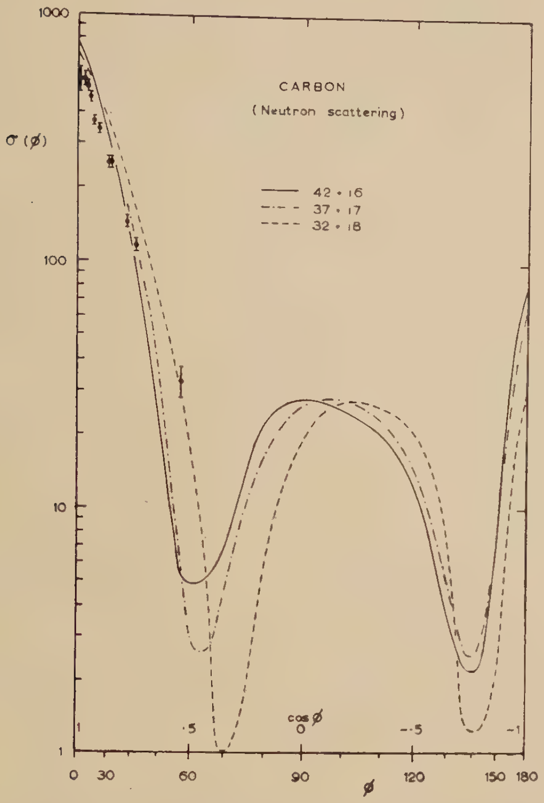

Experimental points and theoretical curves for 14 MEV neutrons elastically scattered by carbon.

Table 2. Cross sections for the Scattering of 14 MEV Neutrons by Carbon (in barns)

Square-Well Potential (MEV)	Elastic scattering cross section	Absorption cross section	Total cross section
$32+i8$	0·82	0·49	1·31
$37+i6$	0·87	0·48	1·35
$37+i7$	0·77	0·54	1·31
$42+i5$	0·85	0·56	1·41
$42+i6$	0·76	0·56	1·32
$42+i8$	0·61	0·57	1·18
$44+i5$	0·81	0·54	1·35
$44+i6$	0·73	0·56	1·29
$47+i5$	0·69	0·49	1·18
Experimental	0·72 ± 0·04	0·60 ± 0·03	1·32 ± 0·02

The larger values of W_0 for this element, compared with that for oxygen, may well be explained by the presence of more low lying levels in carbon than in oxygen, providing a greater total inelastic cross section. The thresholds for both (p, n) and (p, pn) reactions are above 9·5 MeV, and the cross sections for (p, α) and (p, γ) are probably very small. The values of r_0 for carbon, nitrogen and argon are slightly different from that for oxygen. This was occasioned by a small simplification of the calculations, and is known to have a negligible effect on the theoretical curve.

Preliminary calculations have been made in an attempt to fit the experimental results of Wright (1953) for the scattering of 30·6 MeV protons by carbon. The radius used was $3{\cdot}320\times10^{-13}$ cm and values of $L\leqslant4$ were considered. It was possible to give a fairly good fit up to $\phi=90°$, for $V=-(42+i6{\cdot}3)$ but the positions of the higher angle minima were at much smaller angles than the experimental values. The cross sections for $\phi>140°$ rise steeply to values near 180° which are of the order of 100 times the experimental values. Both of these divergencies confirm the work of Chase and Rohrlich (1954) and indicate the greater need for shaping the well at higher energies, as done by Woods and Saxon (1954).

The differential cross section for 14 MeV neutrons elastically scattered from carbon is available only for $\phi<55°$ (Coon, private communication). This is insufficient for a determination of the best values of V_0 and W_0. However the further criterion of total elastic and absorption cross sections can be applied. Table 2 gives the values for a series of potentials, and the experimental results. Combinations of V_0 and W_0 are given which lead to a total cross section of about 1·32 barns, i.e. the experimental value. As V_0 is increased from 32 to 47 MeV, W_0 must be decreased from 8 to 4 MeV. At the same time the absorption cross section increases and the elastic scattering cross section decreases, each approaching the experimental value. It is seen that the most probable value of V is $-(42+i6)$. Figure 4 shows the corresponding differential cross sections, and the experimental points.

§ 4. NITROGEN

The experimental values of the differential cross section for 9·5 MeV protons elastically scattered from nitrogen (Freemantle *et al.* 1954) are shown in fig. 5. The points do not appear to lie on a smooth curve and the values rise steeply at backward angles ($\phi>150°$). It is possible that this is associated with the odd–odd system of nucleons, which can be expected to produce a complicated configuration of the nucleus. The Optical Model gives no more than a moderately good fit. The best curve is that for $V=-(42+i4{\cdot}2)$. Figure 5 includes the curves for $V_0=42$ with $W_0=0$, 2·1, 4·2, and 6·3 MeV showing the characteristic variation of the shape as W_0 is decreased from 6·3 to 2·1 MeV. The curve for $W_0=0$ shows the anomalous subsidiary maximum near $\phi=60°$ occasioned by a large contribution for $L=3$ (cf. fig. 1 where this occurs at $V_0=38$ with $W_0=0$ for oxygen).

The differential cross section for 14 MeV neutrons elastically scattered from nitrogen has been measured by Smith (1954) and the total elastic and absorption cross sections are given by Coon *et al.* (1952). Total cross sections are easier to calculate than differential cross sections and the results for certain potentials are given in table 3. No really good agreement could be obtained, the best values being for $V=-(36+i8)$.

Fig. 5.

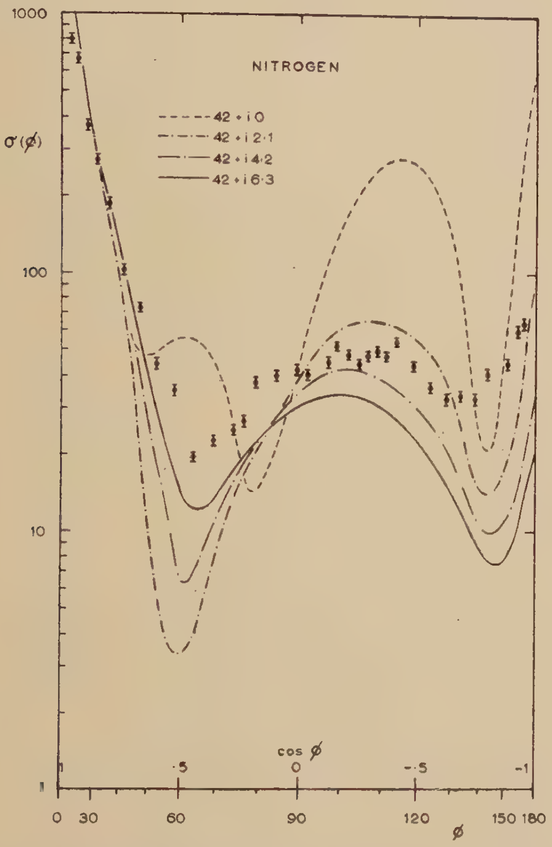

Experimental points for 9·5 MeV protons elastically scattered by nitrogen. The series of theoretical curves shows the variation with W_0, as discussed in the text.

Difficulty was experienced in obtaining a sufficiently high value of the total cross section consistent with an approximately correct ratio of elastic to absorption cross section. It was also difficult to fit the differential cross section curve, as can be seen in fig. 6. The general pattern of maxima and minima is of course reproduced, but the absolute values are far from correct. Thus it is not possible to make a sensible comparison between the best values of V for protons and neutrons. This also may be due to the odd–odd system of nucleons. On the other hand, the paucity

Fig. 6

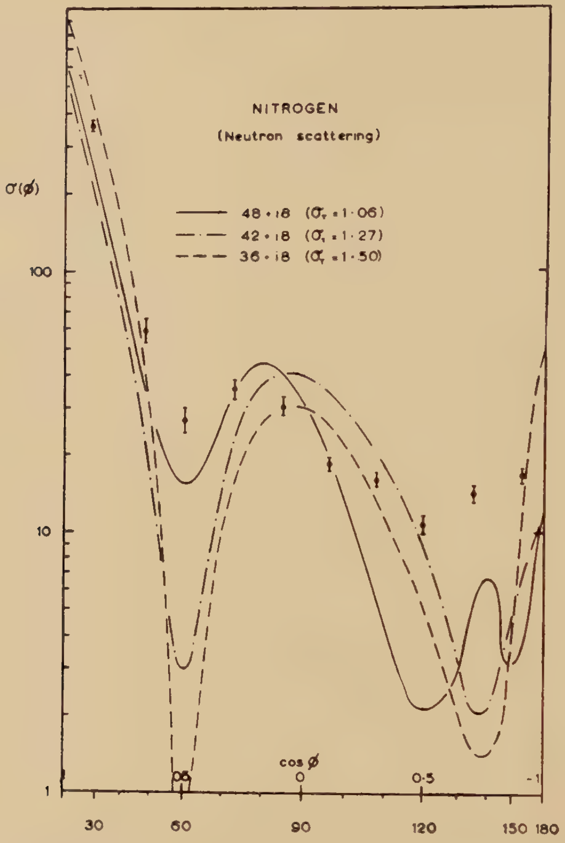

Experimental points and theoretical curves of 14 MeV neutrons elastically scattered by nitrogen.

Table 3. Cross sections for the scattering of 14 MeV neutrons by Nitrogen (in barns)

Square-Well Potential (MeV)	Elastic scattering cross section	Absorption cross section	Total cross section
$32+i8$	0·89 (5)	0·58 (5)	1·48
$36+i8$	0·86	0·63 (5)	1·49 (5)
$39+i8$	0·80	0·62	1·42
$42+i5$	1·03	0·49	1·52
$42+i8$	0·71	0·56	1·27
$48+i5$	0·95 (5)	0·30	1·25 (5)
$48+i8$	0·57	0·49	1·06
Experimental	0·82	0·77	1·59

of differential cross section data for neutrons of this energy does not allow the conclusion to be drawn that nitrogen is unusual for both neutrons and protons. It is possible that the square-well Optical Model does not give a good representation of the differential cross section curve for neutrons of this energy region—but in the light of its fair success for protons this would be a surprising result.

Fig. 7

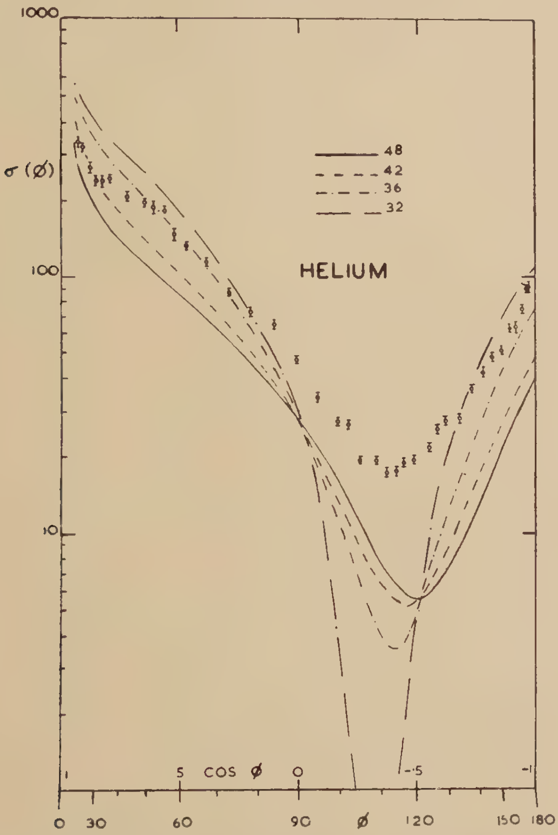

Experimental points and theoretical curves for 9·5 MeV protons elastically scattered by helium.

§ 5. HELIUM, NEON, FLUORINE AND ARGON

Angular distributions for 9·5 MeV protons elastically scattered from these elements have been obtained experimentally. The values for fluorine have been kindly communicated, prior to publication, by Dr. D. J. A. Prowse. For the other elements the results used here are those of Freemantle *et al.* (1954) with certain additions communicated privately.

Other data are available for helium, and those obtained by Putnam (1952) have been subjected to a detailed phase-shift analysis by Dodder and Gammel (1952). Nevertheless it was felt to be worthwhile to use the

Optical Model for this element also, in order to discover the limits within which it could be applied. The results are shown in fig. 7. It was found that contributions arising from $L \geqslant 3$ were negligible because of the small size of the nucleus. The fit is better than might have been expected especially considering the relative crudity of the model which neglects *inter alia* spin-orbit coupling. The value of W_0 was taken to be zero,

Fig. 8

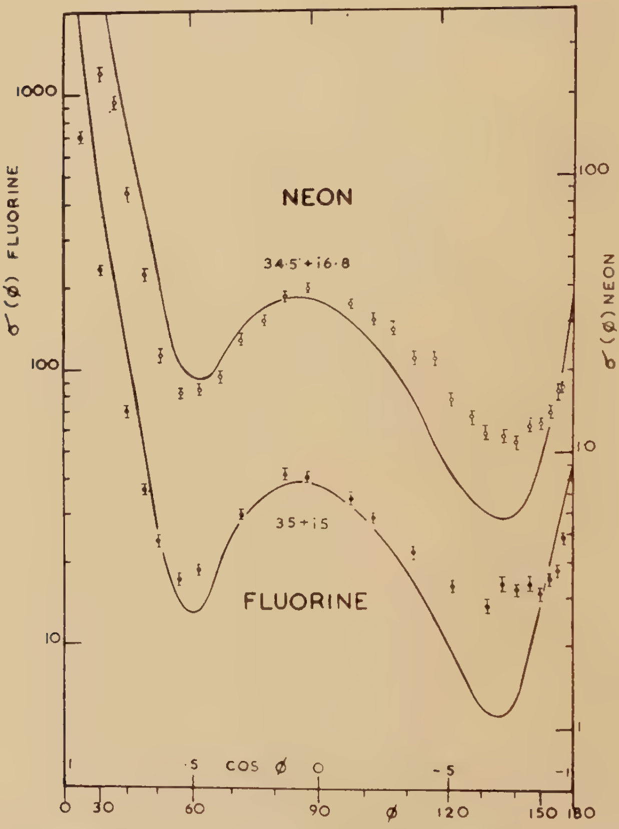

Experimental points and theoretical curves for 9·5 Mev protons elastically scattered by neon and fluorine. Note that the $\sigma(\phi)$ scale for neon is displaced upwards by half a cycle.

thereby assuming a zero absorption cross section. However, we tentatively suggest that the fit may be improved by introducing a value of W_0 to allow for the formation of the compound nucleus ^{5}Li and then calculating the ' compound-elastic ' scattering. In this particular case the only channel open to the protons is that leading to the formation of an alpha particle. It is also possible that a larger radius could be invoked to produce a larger cross section and therefore a better fit.

Neon and fluorine yield almost identical experimental values of angular distributions, and are shown for comparison in the same figure (fig. 8).

The $\sigma(\phi)$ scales are displaced to show the agreement with the theoretical curves. This agreement is quite good, except near the second minimum, for potential values of $V=-(34{\cdot}5+i6{\cdot}8)$ for neon and $V=-(35+i5)$ for fluorine. The higher value of W_0 for neon, compared with nitrogen, is consistent with the available energy levels and the sum of their cross sections, which is fairly high. In the case of fluorine however, the value of W_0 might be expected to be larger than that found here. It would appear from these results that the square-well Optical Model applies equally well to the even nucleus neon and the odd nucleus fluorine for the interpretation of the scattering of 9·5 MeV protons. The close resemblance of the experimental curves for these two nuclei is very striking.

Fig. 9

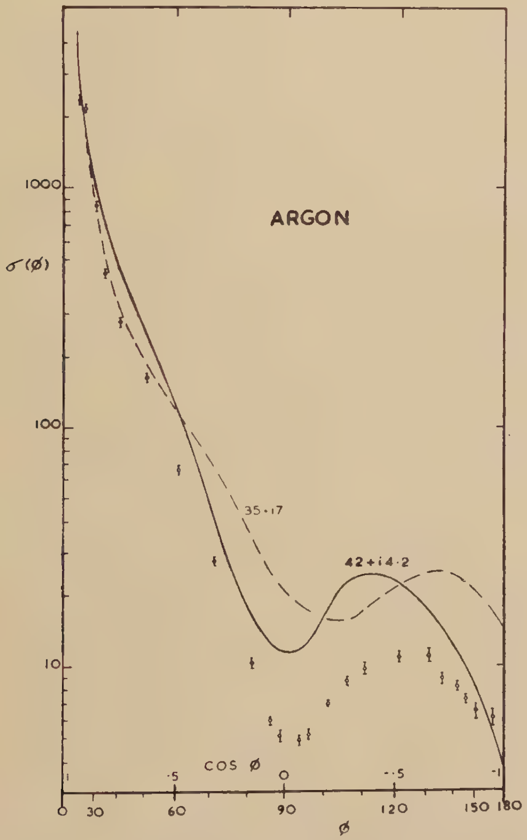

Experimental points and theoretical curves for 9·5 MeV protons elastically scattered by argon.

Calculations have also been made for 9·5 MeV protons elastically scattered from argon. The results are shown in fig. 9. For the radius used here, $4{\cdot}80\times10^{-13}$ cm, the value of $\sigma(\phi)$ is too high, suggesting that it might be more nearly fitted by using a smaller radius. However, it is possible to fit the angular position of the first minimum and maximum by $V=-(42+i4{\cdot}2)$.

§ 6. DISCUSSION

The present results indicate that the scattering of low energy (9·5 MeV) protons by the lighter nuclei can be moderately well represented by the Optical Model of the nucleus, using a square-well potential as a first approximation. It is however confirmed that scattering of the same energy protons by somewhat heavier nuclei (e.g. argon) cannot be so well accounted for by such a simple model. This agrees with the conclusions of Chase and Rohrlich (1954). The work of Britten (1952) on 31·5 MeV protons scattered by beryllium appears to be confirmed by the preliminary calculations for 30·6 MeV protons on carbon, showing that higher energies also require a more complicated model for a satisfactory account of experimental values.

It is quite possible that better fits could be obtained by a systematic investigation of the influence of the radius R on the calculations. In the case of oxygen, preliminary calculations showed that a radius of $4{\cdot}4\times10^{-13}$ cm gave much too great a cross section. Also a change from 3·65 to $3{\cdot}75\times10^{-13}$ cm made very little difference to the shape and absolute cross section for a given potential. In this connection it is noticed that the formula $R=(1{\cdot}2A^{1/3}+0{\cdot}7)\times10^{-13}$ cm recently proposed by Weisskopf (private communication) gives values of the radius which would lead to better fits, as discussed above. Thus for helium this formula gives $R=2{\cdot}61\times10^{-13}$ cm compared with the value $2{\cdot}3\times10^{-13}$ cm used here, and for argon $R=4{\cdot}8\times10^{-13}$ cm instead of the value $4{\cdot}95\times10^{-13}$ cm. In the latter case the change in the differential cross section curve would be very small.

For the elements considered here, the mean free path of the incident protons in nuclear matter lies between $4{\cdot}4\times10^{-13}$ cm (for neon) and $8{\cdot}2\times10^{-13}$ cm (for carbon), except for oxygen where it is somewhat larger ($15{\cdot}1\times10^{-13}$ cm). These values are calculated from the relation $4{\cdot}5(E+V_0)^{1/2}/W_0$ (see Chase and Rohrlich 1952) using the best values of V_0 and W_0. No value was found smaller than the nuclear radius.

It is possible that a particular element is characterized by a certain value of V_0 but this may vary with the energy of the incident nucleons. This points to the need for more experimental values of the differential cross sections of elastically scattered neutrons at various energies. The calculations for neutrons are much simpler, and the absence of Coulomb scattering allows comparisons of total cross sections.

The work reported here indicates the limits of application of the square-well Optical Model. A closer approximation to the true picture is provided by a shaping of the well thereby taking into account the diffuseness of the nuclear surface and, in the proton case, allowing the equivalent of a variable charge distribution of the nucleus. This has been done by Woods and Saxon (1954) for 22 MeV and 18 MeV protons on platinum and nickel respectively. A greatly improved agreement was obtained for the relation

$$V_{(r)}=\frac{V+iW}{1+\exp[(r-r_0)/a]}$$

with $V \approx 40$ MeV, $W \approx 10$ MeV, $r_0(\mathrm{Pt}) = 8{\cdot}24 \times 10^{-13}$ cm, $a(\mathrm{Pt}) = 0{\cdot}49 \times 10^{-13}$ cm and $r_0(\mathrm{Ni}) = 5{\cdot}3 \times 10^{-13}$ cm and $a(\mathrm{Ni}) = 0{\cdot}35 \times 10^{-13}$ cm. This energy region allows a more sensitive test of the shaping of the potential well, because of the shorter wavelength. It is evident that a multiplication of independently variable parameters can be expected to lead to more precise agreement between theory and experiment.

ACKNOWLEDGMENTS

We are grateful to Dr. D. J. A. Prowse for valuable discussions during the course of this work and to Professor C. F. Powell, F.R.S. for his interest and encouragement.

REFERENCES

ADAIR, R. K., 1954, *Phys. Rev.*, **94,** 737.
AJZENBERG, F., and LAURITSEN, T., 1952, *Rev. Mod. Phys.*, **24,** 321.
BLATT, J., and WEISSKOPF, V. F., 1952, *Theoretical Nuclear Physics* (New York: John Wiley and Sons).
BRITTEN, R., 1952, *Phys. Rev.*, **88,** 283.
BURCHAM, W. E., GIBSON, W. M., HOSSAIN, A., and ROTBLAT, J., 1953, *Phys. Rev.*, **92,** 1266.
CHASE, D. M., and ROHRLICH, F., 1954, *Phys. Rev.*, **94,** 81.
CONNER, J. P., 1953, *Phys. Rev.*, **89,** 712.
COON, J. H., GRAVES, E. R., and BARSCHALL, H. H., 1952, *Phys. Rev.*, **88,** 562.
DODDER, D. C., and GAMMEL, J. L., 1952, *Phys. Rev.*, **88,** 520.
FESHBACH, H., PORTER, C. E., and WEISSKOPF, V. F., 1954, *Phys. Rev.*, **96,** 448.
FISCHER, G. E., 1954, *Phys. Rev.*, **96,** 704.
FREEMANTLE, R. G., PROWSE, D. J., and ROTBLAT, J., 1954, *Phys. Rev.*, **96,** 1268.
FREEMANTLE, R. G., PROWSE, D. J., HOSSAIN, A,. and ROTBLAT, J., 1954, *Phys. Rev.*, **96,** 1270.
FREEMANTLE, R. G. GROTDAL, T., GIBSON, W. M., MCKEAGUE, R., PROWSE, D. J., and ROTBLAT, J., 1954, *Phil. Mag.*, **45,** 1090.
FUJIMOTO, Y., and HOSSAIN, A., 1955, *Phil. Mag.*, **46,** 542.
SMITH, J. R., 1954, *Phys. Rev.*, **95,** 730.
WOODS, R. D., and SAXON, D. S., 1954, *Phys. Rev.*, **95,** 577.
WRIGHT, B. T., 1953, *University of California Report*, UCRL, 2422.

III. *Dislocation Densities in Some Annealed and Cold-Worked Metals from Measurements on the X-ray Debye–Scherrer Spectrum*

By G. K. Williamson and R. E. Smallman
Metallurgy Division, A.E.R.E., Harwell*

[Received August 11, 1955]

Abstract

Two basic equations are derived for deducing the dislocation density in powdered materials from the particle size and strain breadth measured from the Debye–Scherrer spectrum. In the particle size estimate, it is assumed that the material has a block structure similar to that found in microbeam studies and that the dislocations lie along the block surfaces. The number of dislocations along each face, n, is not known. In the strain broadening estimate the x-ray line broadening from a dislocation array is calculated in terms of the broadening due to an isolated dislocation and a strain energy factor F, which allows for the effect of dislocation arrangement. Both methods involve an unknown quantity but by equating the two results it is possible in most cases to get both a narrow bracket for the dislocation density and considerable information on the dislocation arrangement.

In annealed metals the values of ρ range from 2×10^7 cm of dislocation line per cm^3 for aluminium to 3×10^8 for tungsten and molybdenum, the majority of dislocations being ‘ random ’, i.e. the number along each edge is approximately 1. There is some correlation between ρ and the purity and annealing treatment of the powder. High purity and high annealing temperatures result in smaller dislocation densities.

In cold-worked metals the dislocation density is more variable. A precise analysis is possible for aluminium ; high purity aluminium filed at room temperature gives $\rho=4{\cdot}5$ to $7{\cdot}6\times10^9$ with evidence for recovery, possibly by polygonization. Commercially pure aluminium filed at both room temperature and liquid air give $\rho=5\times10^9$ to $2{\cdot}7\times10^{10}$ and $\rho=1{\cdot}5\times10^{10}$ to $3{\cdot}2\times10^{11}$ respectively. Some dislocation array such as a ‘ pile-up ’, which causes an increase in the strain energy of dislocations exists in both these samples as with all the other metals examined. Dislocation densities are also given for tungsten, molybdenum, iron and α-brass. In α-brass, the only alloy considered, ρ is higher than for the pure metals and there is strong evidence that the dislocations are effectively random and that each dislocation is attached to a stacking fault.

---

* Communicated by the Authors.

§ 1. INTRODUCTION

DISLOCATION densities and information about dislocation arrangements have been deduced recently by Gay, Hirsch and Kelly (1953, 1954) from x-ray microbeam studies of cold-worked metals. The dislocation densities quoted are lower than previously accepted values and it appeared desirable to derive values from other x-ray results. In this paper values are deduced from x-ray measurements on the Debye–Scherrer spectrum of a number of metals and additional information about dislocation arrangements is given.

§ 2. METHODS

Two quantities, both of which can be calculated from measurements on the Debye–Scherrer spectrum, may be used for calculating the dislocation density. The particle size may be derived from measurements of primary extinction (Williamson and Smallman 1955), line broadening (Williamson and Hall 1953, and Williamson and Smallman 1954) and from measurements of the peak shift produced by stacking faults (Paterson 1952 and Warren and Warekois 1953). The evidence from microbeam experiments indicates that the metal is broken up into blocks, the dislocations lying in the boundaries between the blocks. If there are n dislocations per block face the total length of dislocation line per block is $6\,n\,D/2$ (since each face is shared by 2 blocks) where D is the dimension of the block. The number of blocks per unit volume is $1/D^3$ and thus the dislocation density calculated from the particle size is

$$\rho = 6nD/2D^3 = 3n/D^2. \qquad \text{(1)}$$

To utilize this equation the value of n must be determined or assumed. The value $n=1$ gives a minimum dislocation density and could apply to annealed metals and to very severely deformed metals, in which state the dislocations may be very nearly random.

In deriving eqn. (1) we have defined ρ as the total length of dislocation line in unit volume. With this definition ρ is independent of the dislocation distribution. Densities expressed as the number of dislocation lines cutting unit area are usually equivalent, but an alternative interpretation of this has been employed which is not equivalent to eqn. (1). Gay, Hirsch and Kelly (1953), for example, have given values in terms of the effective numbers of dislocations cutting unit area with Burgers vector lying in the surface of the area. Using this definition one would obtain, instead of eqn. (1), that $\rho = n/D^2$, i.e. values $\frac{1}{3}$ of those quoted in the remainder of this paper*. This factor has been allowed for in comparing our values with those of Gay, Hirsch and Kelly in that the values quoted here are 3 times their published figures.

---

* The factor is $\frac{1}{3}$ only for an isotropic distribution of dislocations. For a non-isotropic distribution the latter definition is ambiguous and gives a variable value for ρ; by a special choice of the orientation of the area it is sometimes possible to make the two definitions agree.

From measurements of line profile it is possible to deduce the breadth of the strain distribution ξ (Williamson and Hall 1953). If $\overline{S^2}$ is the mean square strain of this distribution the stored energy of the lattice V is

$$V=3\,E\,\overline{S^2}/2=3\,E\,(A\xi^2)/2 \qquad (2)$$

where E is Young's modulus and the factor A depends on the shape of the strain distribution. The energy of a dislocation v_c can be calculated in the absence of interaction with other dislocations and has been shown to be, for a screw dislocation

$$v_c=\frac{\mu\mathbf{b}^2}{4\pi}\ln(r/r_0) \qquad (3)$$

where $\mathbf{b}$ is the Burgers vector of the dislocation, μ is the shear modulus, r is the radius of the crystal containing the dislocation and r_0 is a suitably chosen integration limit, usually about 10^{-7} cm (see Cottrell 1954).

In reality dislocations interact so that their strain energies are changed on the average by a factor F, i.e.

$$v_{\text{real}}=v_cF. \qquad (4)$$

The dislocation density ρ calculated from the strain broadening is thus

$$\rho=\frac{V}{v_{\text{real}}}=\frac{k}{F}\cdot\frac{\xi^2}{\mathbf{b}^2} \qquad (5)$$

where $k=6\pi EA/\mu\ln(r/r_0)$. An approximate value of k can be found simply; E/μ is fairly constant for the metals studied here and is approximately 2·6, $\ln(r/r_0)$ is a slowly varying function of r a reasonable value being 4, so that $k\sim 12\,A$. Williamson and Smallman (1954) have investigated the effect of line shape and have shown that for cold-worked metals the profile of the strain distribution lies between the extremes of a Cauchy and Gaussian distribution; for the Cauchy $A\sim 2$, and for a Gaussian $A=\frac{1}{2}\pi$. Thus k lies in the range 2 to 25.

A more exact calculation of k which does not involve any of the above assumptions, is possible by using the results of Wilson (1949) for the broadening by a screw dislocation. This calculation is done in the Appendix and gives $k=16{\cdot}1$ for face-centred cubic materials with Burgers vector $\mathbf{b}$ along [110], and $k=14{\cdot}4$ for body-centred cubic metals with $\mathbf{b}$ along [111]. These values agree well with the approximate values deduced above and support the contention (Williamson and Smallman 1954) that the actual strain profile is very close to a Cauchy distribution.

Equation (5) can be applied directly to the results only if the interaction factor F is known or assumed. The simplest assumption (one that is always made in calculating dislocation densities from the calorimetric determination of stored energy) is that $F=1$. One model which approximates to $F=1$ is that in which one dislocation coincides with the edge of each block, the dislocations then have their maximum separation and interaction is a minimum. Evidently this model coincides with $n=1$ in addition to $F=1$ and it is easy to test the validity of these two assumptions since their correctness would imply that $\rho_p=\rho_s$, where ρ_p and ρ_s

are the values of ρ calculated from eqns. (1) and (5) respectively in which values $n=1$ and $F=1$ have been used.

This possibility of testing from the experimental results whether a given dislocation arrangement is possible can be extended further and in addition to giving valuable information about the dislocation arrangement it considerably reduces the range of uncertainty in the final values for ρ. We shall consider two simple arrangements for which there is considerable experimental evidence and which appear to represent the two possible extremes for the factor F. If other models can be devised which produce a greater range of interaction factors these could be used equally well in the following discussion.

Piling up of the dislocations against barriers in the slip plane is commonly postulated as a mechanism for producing work hardening and this causes a large increase in the strain energy per dislocation. If there are n dislocations in each pile up they act to a first approximation as one dislocation of Burgers vector $n\mathbf{b}$ and hence the strain energy is increased from nv_c to n^2v_c (since it is the square of the Burgers vector which determines the energy in eqn. (3)). Thus $F=n$.

Polygonization on the other hand decreases the strain energy since the dislocations ‘ climb ’ from their slip planes to form bend planes and their long range stress fields cancel at distances from the bend planes greater than h, where h is the separation of dislocations in the bend plane. The energy of each dislocation is reduced from the value given in eqn. (3) to the value corresponding to $r=h$. Thus

$$F=\ln (h/r_0)/\ln (r/r_0). \qquad . \quad . \quad . \quad . \quad . \quad . \quad (6)$$

However, $h=D/n$ and substituting eqn. (1) for n, $h=3/\rho D$, where ρ is the true dislocation density, also $r\sim\frac{1}{2}\sqrt{3/\rho}$ and $r_0=10^{-7}$ cm.*

Equation (5) now reduces to an equation for ρ, namely

$$\rho=\rho_s/F=\rho_s \ln\left(\frac{10^7\sqrt{3}}{2\sqrt{\rho}}\right)\bigg/ \ln (3\times 10^7/\rho D). \quad . \quad . \quad . \quad . \quad (7)$$

This equation is best solved by trial and error starting with $\rho=\rho_s$ in the right hand side and, if the results are inconsistent with polygonization (i.e. F less than unity) the successive values of ρ rapidly diverge to infinity. If polygonization is shown to be impossible by this treatment a lower limit to ρ can be determined since pile up appears at present to represent the extreme degree of interaction. In this case $F=n$ so that $\rho=n\rho_p=\rho_s/n$ Thus

$$n=(\rho_s/\rho_p)^{1/2} \text{ and } \rho=(\rho_s\rho_p)^{1/2}. \qquad . \quad . \quad . \quad . \quad . \quad . \quad (8)$$

---

* This value of r_0 is used in calculating the energy per dislocation to exclude the dislocation core for within this region the energy is not proportional to the (strain)^2. If the value of h closely approaches r_0 a value $r_0=3\times 10^{-8}$ cm may be more appropriate since line broadening is sensitive to strain and not stored energy. In the case discussed in later sections h is much greater than r_0 and the difficulty does not arise.

§ 3. Dislocation Densities in Annealed Metals

Annealed metals invariably exhibit extinction. Recent studies by Williamson and Smallman (1955 a) show that, for aluminium and α-brass, extinction is primary, and will probably be primary in all metals having a larger absorption coefficient and similar mosaic size. From measurements of the fall in intensity due to extinction it is possible to obtain the average linear dimension of the mosaic blocks D.

If a mosaic block is to reflect incoherently with its neighbouring blocks it must have a misregister of at least one atomic diameter along each edge (see Wilson 1949 a). Exactly such an effect would be produced by the block structure assumed in deriving eqn. (1) and the values of D deduced from measurements of extinction (or particle size broadening) do represent the physical quantity implied by D in eqn. (1). Confirmation of this argument, if it were necessary, is given by the very close correspondence between the values of D found in this study for aluminium and the values measured using microbeam methods (Gay, Hirsch and Kelly 1953).

Studies of extinction in a number of metals give the values of particle D shown in table 1. The value for tungsten has been derived from data for the 110 reflection only, the remaining values have been obtained using all the observed lines. Values of D for the annealed specimen of thoriated tungsten (Warren and McKeenham 1953) have not been included in table 1 since $D=8\times10^{-6}$ cm giving $\rho_p=4{\cdot}5\times10^{10}$; this sample is certainly not recrystallized. This result was anticipated because of the low annealing temperature used, 1050°c, compared to a temperature of 1350°c required for purer tungsten in the experiments of Williamson and Hall (1953).

The values for the strain broadening from annealed metals are more uncertain than the particle size. Williamson and Hall have shown that for aluminium and tungsten the slope of a plot of β^* against d^* has a minimum value (after correcting for the geometrical abberation of spectrometer) of about 3×10^{-4}. The maximum value of this slope is probably 4×10^{-4}. This broadening has been tentatively attributed to strains by Williamson and Hall (1953). However, a reliable estimate of the strain breadth is difficult since the natural breadth of the Kα doublet produces an effect indistinguishable from strain broadening For copper Kα radiation the half peak width of the wavelength distribution is 5×10^{-4} Å and the apparent strain breadth is $5\times10^{-4}/1{\cdot}5\simeq3\times10^{-4}$. Since the maximum experimental error in this determination is approximately 1×10^{-4}, then the probable value for the strain breadth is in the region of $0{\cdot}5\times10^{-4}$. Taking $\mathbf{b}$ as $2{\cdot}7\times10^{-8}$ cm the value ρ_s (i.e. $F=1$) is about 5×10^{-7}. This is in very close agreement with the values of ρ_p given in table 1 and justifies the appliaction of the block model with one dislocation at each block edge in discussing the annealed state. Only the values ρ_p are given in table 1 as these are the more accurate.

An important correlation also appears between the variations in ρ and the annealing temperature in table 1. This is best seen by comparing

Table 1. Minimum Values of the Dislocation Density in Annealed Metals from Extinction Studies

Source of original data	Metal	Purity	Anneal Temp. T	λ	D (cm)	$\rho_p = \frac{3}{D^2}$	$\frac{T_M}{T}$
Williamson & Hall 1953	Al	99·99%	500°c	Cu K	$3{\cdot}5 \times 10^{-4}$	$2{\cdot}4 \times 10^{7}$	1·21
Averbach & Warren 1949	α-brass	—	350°c	Cu K	$1{\cdot}25 \times 10^{-4}$	$2{\cdot}4 \times 10^{8}$	2·12
Williamson & Hall 1953	W	99·9+%	1350°c	Cu K	$0{\cdot}8$ to $1{\cdot}2 \times 10^{-4}$	3×10^{8}	2·28
Williamson & Smallman 1955 b	Fe	Armco	675°c	Co K	$1{\cdot}2 \times 10^{-4}$	2×10^{8}	1·96
	Fe	Carbon-Free	675°c	Mo K	2×10^{-4}	7×10^{7}	
	Mo	commercially pure	1360°c	Cu K	1×10^{-4}	3×10^{8}	1·82
	Mo		1860°c	Mo K	2×10^{-4}	7×10^{7}	1·43

the value of ρ with the ratio T_M/T where T_M is the melting point (°K) and T the annealing temperature. Aluminium, with the lowest value of ρ observed in these studies has the lowest value T_M/T (1·21) whilst tungsten with a temperature ratio (2·28) gives a dislocation density of about 3×10^{-8}. The values for molybdenum illustrate this effect most clearly since both samples had the same purity and only differed in their annealing treatment. This case shows that ρ is a very steep function of T_M/T. No quantitative correlation using all the results is possible since the purity of the material appears to have an appreciable effect. The values for iron differ considerably even though both samples had the same annealing treatment; this difference must be ascribed to the difference in carbon content since one sample had been decarburized (other traces of impurities would be present to the same extent in both specimens). The amount of carbon in the armco iron before decarburization impeded the motion of dislocations at room temperature to a sufficient extent for a yield point to be observed, no such yield point being detected after decarburization. However, the magnitude of the effect of the carbon on the value of ρ is at first surprising for at the temperature of annealing the carbon atoms would have a very fast rate of diffusion. The effect might be explained if it were assumed that, during prolonged annealing after recrystallization the dislocations are in constant motion so that the mosaic block pattern is constantly changing.

§ 4. DISLOCATION DENSITIES IN COLD-WORKED METALS

Measurements of strain breadth can be made with comparative ease for all cold-worked metals but the values for particle size can be deduced with accuracy only for those metals which exhibit extinction even after cold working. For the remaining metals the particle size has been estimated from the line broadening but this answer is very much less accurate. In table 2 two columns each for D are given to indicate the reliability.

The results on aluminium are most useful since accurate particle sizes are known. For high purity aluminium the trial and error solution of eqn. (7) rapidly converges on a dislocation density $\rho=7\cdot6\times10^9$ corresponding to a strain reduction factor of 1·69, $n=162$ dislocations per surface and to an angle between neighbouring blocks $\alpha\simeq1°$. This tilt is in good agreement with microbeam results, as is the particle size D. The results are consistent with polygonization having occurred, as suggested earlier by Williamson and Hall (1953) from a study of Fourier coefficients of the broadened profiles; but it is interesting that, even in this high purity material which recovers readily (so that in some circumstances it recrystallizes at room temperature), the effect of recovery on the line broadening is slight, the density is only 70% greater than ρ_s. Since the effect of recovery is expected to be less for all the other materials studied the values of ρ_s given in table 2 can be taken as upper limits to ρ.

Table 2. Calculation of Dislocation Density in Cold-Worked Metals from Particle Size and Strain Broadening. A random dislocation arrangement is not possible since these two values do not agree

Ref.*	Metal and Purity	Treatment and Temperature	Strain Breadth ξ	b cm $\times 10^8$	Max. Stored Energy cals/gm	ρ_s $(F=1)$	D (cm)		ρ_p $(n=1)$
							Extinction	Line Broadening	
W. & H.	Aluminium 99·99%	Filed 20°c	$4{\cdot}5\times 10^{-4}$	2·85	0·004	$4{\cdot}0\times 10^{9}$	$2{\cdot}6\times 10^{-4}$		$4{\cdot}5\times 10^{7}$
W. & H.	Aluminium (Commercial)	Filed 20°c	$1{\cdot}1\times 10^{-3}$	2·85	0·03	$2{\cdot}4\times 10^{10}$	2×10^{-4}		7×10^{7}
W. & S.	Aluminium (Commercial)	Filed −183°c	4×10^{-3}†	2·85	0·3	$3{\cdot}2\times 10^{11}$	$0{\cdot}7\times 10^{-4}$†		6×10^{8}
W. & H.	Tungsten (99·9%+)	Filed 20°c	$6{\cdot}5\times 10^{-3}$	2·74	0·62	$7{\cdot}8\times 10^{11}$		10^{-5}	3×10^{10}
W. & H.	Tungsten (99·9%+)	Annealed 1130°c	10^{-3}	2·74	0·015	$2{\cdot}1\times 10^{10}$	$4{\cdot}5\times 10^{-5}$		$1{\cdot}4\times 10^{9}$
W. & S.	Molybaenum (Commercial)	Filed 20°c	$5{\cdot}5\times 10^{-3}$	2·72	0·62	$5{\cdot}8\times 10^{11}$		10^{-5}	3×10^{10}
W. & S.	Iron (Armco)	Filed −183°c	$5{\cdot}5\times 10^{-3}$	2·47	0·60	$6{\cdot}9\times 10^{11}$		10^{-5}	3×10^{10}
W. & S.	Iron (Armco)	Filed 20°c	4×10^{-3}	2·47	0·33	$3{\cdot}7\times 10^{11}$		10^{-5}	3×10^{10}

* W. & H.=Williamson and Hall (1953), W. & S.=Williamson and Smallman 1955.

† The low temperature value for aluminium is based on the rapid measurement of one line, the breadth of which decreased even during this short time. The value of D is an estimate from the above value (see text).

This postulate is confirmed by an analysis of the results for commercially pure aluminium. Equation (7) has no solution unless $h<r_0$ and $\alpha>20°$. Tilts of this magnitude have not been observed in micro-beam studies and polygonization is very unlikely. Thus $\rho_s=2{\cdot}4\times10^{10}$ appears to be an upper limit to the dislocation density in this case. The lower limit corresponding to severe pile up is $\rho=1{\cdot}4\times10^9$ (corresponding to $n=20$). Since commercially pure aluminium recovers some of its mechanical properties very readily at room temperature we would anticipate some ' unpiling ' so that ρ would be in the range 1–$2{\cdot}7\times10^{10}$. The results from the aluminium filed at liquid air temperatures are consistent with this, although a precise calculation is not possible as D is not known. A crude estimate of D is possible since Gay, Hirsch and Kelly (1954) have suggested that D is the slip band spacing, and Brown (1951) has shown that for deformation at liquid air temperatures the slip bands have one-third the separation they have at room temperature. If $D_{-183°}=0{\cdot}7\times10^{-4}$ ($D_{20°}=2\times10^{-4}$ cm) then there can be no polygonization as eqn. (7) has no solution. Equation (8) gives a dislocation density of $1{\cdot}5\times10^{10}$ if pile up is severe, whilst the upper limit to the density (ρ_s) is $3{\cdot}2\times10^{11}$. We expect less ' unpiling ' in this sample and $\rho\sim2\times10^{10}$ is consistent both with this and the ' unpiled ' value for the sample filed at room temperature.

A similar treatment is possible for the results from tungsten annealed at 1150°C which Hall and Williamson (1953) showed not to be recrystallized. Solution of eqn. (7) indicates slight recovery, the dislocation density being $2{\cdot}6\times10^{10}$, corresponding to a reduction in the strain energy per dislocation by 25%, with $n=20$; and to a tilt α of about $50'$ of arc. A similar analysis could be done using the results from thoriated tungsten published by Warren and McKeenhan (1953) since their ' annealed ' sample showed extinction corresponding to $D=8\times10^{-6}$ cm and $\rho_p=4{\cdot}5\times10^{10}$. It seems likely that this sample is polygonized and not truly annealed since the annealing temperature was 100°C lower than that used for the recovery treatment on the pure tungsten. The strain broadening was not measured although the strain breadth must exceed $1{\cdot}5\times10^{-3}$. Assuming by analogy that $n\sim10$ then $\rho\sim4{\cdot}5\times10^{11}$.

It is not possible to carry out such a detailed discussion for the remaining results listed in table 2 since exact values of D are not available. It is possible to set a lower limit to the particle size by line broadening studies and generally $10^{-4}\text{ cm}>D>10^{-5}$ cm. From the foregoing discussion on aluminium we do not expect any polygonization, though even if it does occur the effect on the upper limit of the dislocation density will be negligible. The range of values of ρ produced by taking these limits for D are given in table 4 for tungsten, molybdenum, iron filed at $-183°$C and iron filed at 20°C respectively.

Values for ρ_s can also be deduced by the Fourier analysis of line shapes which usually gives values of the mean square strain instead of the line breadth. The mean square strain for heavily cold-worked metals assuming a Gaussian profile is usually one-quarter that obtained assuming a Cauchy profile. The stored energy approach is used to give the two extreme values of ρ listed in table 3. Values for brass are taken from Warren and Warekois (1953), who only give values for the Gaussian profile, the upper limit is a very approximate estimate from this result.

Table 3. Calculation of Dislocation Density from the Mean Square Strain Determined by Fourier Analysis

Metal	Gaussian Profile		Cauchy Profile	
	$\overline{S^2}$	ρ_s	$\overline{S^2}$	ρ_s
Molybdenum	2×10^{-5}	3×10^{11}	8×10^{-5}	$1{\cdot}3\times10^{12}$
Iron	1×10^{-5}	$1{\cdot}9\times10^{11}$	6×10^{-5}	$1{\cdot}2\times10^{12}$
α-brass	6×10^{-5}	$1{\cdot}2\times10^{12}$	20×10^{-5}	3×10^{12}

The Gaussian and Cauchy profiles bracket the true value of $\overline{S^2}$ and hence ρ_s lies between the two values given.

It should be noted that for α-brass ρ_s is larger than for pure metals. However, Warren and Warekois (1953) have shown that there are extensive stacking faults in this material and these, in addition to contributing to the broadening will act as barriers, maintaining any pile up. For 70/30 brass they give the separation of stacking faults to be approximately 120 Å and, assuming this to be the particle size, $\rho_p = 2{\cdot}5\times10^{12}$ suggesting that $n=1$ and that virtually all dislocations are split into partials separated by an extended stacking fault.

§ 5. DISCUSSION

For the metals examined in the present study the minimum dislocation density in annealed metals varies from $2{\cdot}7\times10^{7}$ to 3×10^{8} and these values agree well with the values found using microbeam methods. The suggestion (made above) that high temperature anneals produce a lower dislocation density is supported by the work of Gay, Hirsch and Kelly who quote a value of $1{\cdot}5\times10^{7}$ cm of dislocation line per cm^3 for an aluminium crystal grown by a method which involves a prolonged anneal just below the melting point. The agreement between all these results is good; in annealed metals it appears that ρ can vary from 10^{7} to 3×10^{8} cm of line per cm^3, the value depending on both the annealing treatment and the purity. The dislocations in annealed metals are arranged in a fairly random fashion, each dislocation forming the edge of a mosaic block and producing the tilt necessary to make them reflect incoherently.

The probable range of values of dislocation density in cold-worked metals is listed in table 4. For heavily cold-worked pure metals the values are in good agreement with those of Gay, Hirsch and Kelly and are an order of magnitude or more lower than the accepted values. Brass, the only alloy considered here appears to have a dislocation density more nearly the conventional value, though this result appears to be associated with the presence of faulting.

In the last column of table 4 the type of dislocation arrangement is indicated as discussed in the text. The range of values for the dislocation density in the tungsten (filed 20°C), molybdenum (filed 20°C) and iron (filed 20°C and −183°C) correspond to the uncertainty in particle size which has been estimated from line broadening ; $\rho_{\min}$ corresponds to $D=10^{-4}$ cm and $\rho_{\max}$ to $D=10^{-5}$ cm. It should be noted that there is no apparent reduction in the dislocation density in tungsten on giving it a recovery treatment at 1150°C sufficient to allow polygonization.

Table 4. Most Probable Range of Dislocation Density in Heavily Cold-Worked Metals

Metal	Treatment	$\rho_{\min}$	$\rho_{\max}$	Dislocation Arrangement
Al 99·99%	Filed 20°C	$4\cdot5\times10^{9}$	$7\cdot6\times10^{9}$	Polygonized
Al (99·7%)	Filed 20°C	5×10^{9}	$2\cdot4\times10^{10}$	Some pile up
Al (99·7%)	Filed −183°C	$1\cdot5\times10^{10}$	$3\cdot2\times10^{11}$	Some pile up
W (99·9+)	Filed 20°C	$1\cdot7\times10^{10}$	$1\cdot7\times10^{11}$	Some pile up
W (99·9+)	Annealed 1150°C	$2\cdot1\times10^{10}$	$2\cdot6\times10^{10}$	Polygonized
Mo (99·9)	Filed 20°C	$1\cdot5\times10^{10}$	$1\cdot5\times10^{11}$	Some pile up
Fe (99·85)	Filed 20°C	$1\cdot05\times10^{10}$	$1\cdot05\times10^{11}$	Some pile up
Fe (99·85)	Filed −183°C	$1\cdot6\times10^{10}$	$1\cdot6\times10^{11}$	Some pile up
Brass	Filed 20°C	2×10^{12}	3×10^{12}	Random

ACKNOWLEDGMENTS

We are very grateful to Dr. H. M. Finniston, head of the Metallurgy Division, A.E.R.E., for his interest and encouragement throughout this work. We have also had valuable discussions with Dr. A. H. Cottrell and Dr. P. B. Hirsch. The unpublished experimental results quoted in this paper were obtained while the authors were in the Metallurgy Department, University of Birmingham.

REFERENCES

AVERBACH, B. L., and WARREN, B. E., 1949, *J. Appl. Phys.*, **20**, 1060.
BROWN, A. F., 1951, *J. Inst. Metals*, **80**, 115.
COTTRELL, A. H., 1954, *Dislocations and Plastic Flow in Metal Crystals* (Oxford : Clarendon Press).
FRANK, F. C., 1949, *Research*, **2**, 542.
GAY, P., HIRSCH, P. B., and KELLY, A., 1953, *Acta Met.*, **1**, 315 ; 1954, *Acta Cryst.*, **7**, 41.
HALL, W. H., and WILLIAMSON, G. K., 1951, *Proc. Phys. Soc.* B, **64**, 946.
PATTERSON, M., 1952, *J. Appl. Phys.*, **23**, 805.
WARREN, B. E., and MCKEENHAN, M., 1953, *J. Appl. Phys.*, **24**, 52.
WARREN, B. E., and WAREKOIS, E. P., 1953, *J. Appl. Phys.*, **24**, 951.
WILLIAMSON, G. K., and HALL, W. H., 1953, *Acta Met.*, **1**, 22.
WILLIAMSON, G. K., and SMALLMAN, R. E., 1954, *Acta Cryst.*, **7**, 574 ; 1955 a, *Proc. Phys. Soc.* B, **68**, 577 ; 1955 b, Unpublished work.
WILSON, A. J. C., 1949 a, *X-ray Optics* (London : Methuen & Co.), p. 3 ; 1949 b, *Research*, **2**, 541 ; 1952, *Acta Cryst.*, **5**, 318.

APPENDIX

Calculation of Strain Broadening Produced by a Dislocation in the Powder Pattern

Wilson (1949, 1952) and Frank (1949) have considered the broadening produced by a screw dislocation. They find that the broadening is very anisotropic, each reciprocal lattice point being broadened in directions perpendicular to the Burgers vector of the dislocation but not in parallel directions. If the axes of reciprocal space are chosen so that the c^* direction is parallel to the Burgers vector then each spot is broadened to a halo whose breadth is given by

$$\beta^* = \frac{1}{\epsilon_0}(1 + 1{\cdot}33\, l)$$

where β^* is the reciprocal lattice breadth, ϵ_0 is the effective particle size of the crystal cylinder containing the dislocation and h, k and l are the orders of reflection along the a^*, b^* and c^* axes respectively. The component of the broadening due to strains is thus $1{\cdot}33\, l/\epsilon_0$ (the breadth of the strain distribution is reduced with increase in r, the radius of the cylinder since this increases the volume of material with low strain energy hence ϵ_0 appears in the term for the strain broadening). However this does not correspond to the broadening observed in practice for two reasons. Firstly the experimental broadening is sensitive only to the variation of the distance of reciprocal lattice intensity from the origin (i.e. the variation in d^*). Thus if ϕ is the angle between this line and the c^* direction the foreshortening factor is cosec ϕ (Wilson 1949). Secondly in a powder pattern on the average all possible reflections of each form will occur and these will not necessarily have the same value of l. Even in hypothetical primitive cubic crystals with dislocation axis along [001] it is clear that the 110, $\bar{1}10$, $1\bar{1}0$ and $\bar{1}\bar{1}0$ reflections have $l=0$, so that four out of the twelve (110) planes will make no contribution to the strain broadening. If ϕ is known, $l = d^*/\mathbf{b}^* \cos\phi$ where $\mathbf{b}^*$ is the reciprocal of the Burgers vector. Thus the effective strain broadening of each reciprocal lattice point is :

$$\beta_s^* = 1{\cdot}33\,(d^*\,\mathbf{b}^*)\sin\phi\cos\phi$$

and the strain breadth ψ (defined as β_s^*/d^*) of each point is

$$\psi = \frac{1{\cdot}33 \sin\phi\cos\phi}{\epsilon_0 \mathbf{b}^*} \quad . \quad . \quad . \quad . \quad . \quad . \quad . \quad . \quad (6)$$

Wilson has calculated the effective particle size for a cylinder of radius, r and has shown that

$$\epsilon_0 = 16r/3\pi$$

and hence $\psi = 0{\cdot}393 \sin 2\phi .\ b/r.$

In table 5 the various values of ϕ, l, and their multiplicities p, ψ and $\bar{\psi}$ are given for possible reflecting planes from a face centred cubic lattice with Burgers vector along the $\langle 110 \rangle$ direction. $\bar{\psi}$ is the weighted mean defined as

$$\bar{\psi} = \Sigma p\psi / \Sigma p.$$

The mean of the breadth $\bar{\psi}$ averaged over lines 3, 4, 11, 12, 16, 19 and 20 is

$$\xi = 0{\cdot}244\ \mathbf{b}/r.$$

Since we are considering the case where there is no interaction between dislocations D^2 in eqn. (1) can be equated to πr^2 and thus

$$\rho = \frac{3}{\pi}\left(\frac{\xi}{0{\cdot}244\ \mathbf{b}}\right)^2 = 16{\cdot}1\xi^2/\mathbf{b}^2\,.$$

For body centred cubic metals with Burgers vector along the $\langle 111 \rangle$ direction $\xi = (0{\cdot}258)\ b/r$ and

$$\rho = \frac{3}{\pi}\left(\frac{\xi}{0{\cdot}258\ \mathbf{b}}\right)^2 = 14{\cdot}4\xi/\mathbf{b}^2.$$

Table 5. Calculation of the Strain Broadening Produced by a Dislocation in the Powder Pattern from Face-Centred Cubic Metals (Burgers Vector along $\langle 110 \rangle$).

Plane	ϕ	l	p	ψ	$\bar{\psi}$
111	35° 16	1	4	0·37 *b*/*r*	0·185 *b*/*r*
(and 222)	90°	0	4	0	
200	45°	1	4	0·393 *b*/*r*	0·262 *b*/*r*
(and 400)	90°	0	2	0	
220	0	2	2	0	0·227 *b*/*r*
	60°	1	8	0·34 *b*/*r*	
	90°	0	2	0	
311	31° 28	2	8	0·350 *b*/*r*	0·268 *b*/*r*
	64 46	1	12	0·303 *b*/*r*	
	90°	0	4	0	
331	13° 15	3	4	0·175 *b*/*r*	0·240 *b*/*r*
	49° 51	2	8	0·387 *b*/*r*	
	71° 41	1	8	0·241 *b*/*r*	
	90°	0	4	0	
420	18° 26	3	4	0·236 *b*/*r*	0·285 *b*/*r*
	50° 46	2	8	0·385 *b*/*r*	
	71° 34	1	12	0·236 *b*/*r*	
				$\xi=$	0·244 *b*/*r*

IV. *Coincidence Measurements on the β-Decay of Boron* 12

By N. W. TANNER
Cavendish Laboratory, Cambridge*

[Received August 15, 1955]

SUMMARY

A study of β–γ and γ–γ coincidences associated with the β-decay of ^{12}B has been made in order to analyse the β-spectrum. It is concluded that, relative to the transition to the ground state of ^{12}C, $(1{\cdot}7\pm0{\cdot}4)\%$ of the β-transitions are to the 4·43 MeV excited state, and $\leqslant(0{\cdot}0\pm0{\cdot}2)\%$ to the 7·66 MeV state. A technique of comparison between ^{12}B and ^{8}Li was used which incidentally gave a new upper limit of $\leqslant(0{\cdot}2\pm0{\cdot}1)\%$ for γ-radiation following the ^{8}Li decay.

§ 1. INTRODUCTION

THE β-spectrum from ^{12}B was studied by Hornyak and Lauritsen (1950) who showed that 90% of the β-transitions are to the ground state of ^{12}C. For this transition $\log ft=4{\cdot}17$ which is a normal 'allowed' value indicating that the ^{12}B ground state is spin 1, even parity; it is assumed that the β-decay comes under the Gamow–Teller description in accord with the isotopic spin selection rule (Christy 1952). Provided $J=1+$ for ^{12}B, then β-transitions to the 4·43 MeV ($J=2+$) and 7·66 MeV (believed to be $J=0+$) excited states of ^{12}C will also be allowed.

The data of Hornyak and Lauritsen† have been re-analysed in terms of the present knowledge of the excited states of ^{12}C. An excellent least squares fit was obtained with 4·8% transition to the 7·66 MeV state of ^{12}C and 3·2% to higher states near 11 MeV; less than 0·1% was indicated for a branch to the 4·43 MeV level. However, plotting $N^{1/2}/p(E_0-E)$ against E (E is the total electron energy, E_0 the maximum total energy, p the momentum, N the counts per unit momentum interval), showed that the β-spectrum could, with difficulty, be reconciled with as much as a 2% transition to the 4·43 MeV level together with several per cent to a higher state, probably that at 9·61 MeV.

Coincidence measurements on the β and γ radiations from ^{12}B have previously been made by Vendryes (1951). Unfortunately the work was done with Geiger counters which did not allow a distinction of β–γ coincidences from β-bremsstrahlung coincidences with any certainty. Vendryes' conclusion was that $(4\pm1)\%$ of all the β-decays are to a γ-decaying state of ^{12}C, probably that at 4·43 MeV.

---

*Communicated by the Author.

† I am grateful to Professor T. Lauritsen for the opportunity of studying the original data on the β-spectrum.

§ 2. PRODUCTION OF ^{12}B

The convenient manner of producing ^{12}B is by the reaction ^{11}B(d, p)^{12}B : a thick natural boron target gave adequate yield with the deuteron energy and beam available from the Cavendish 1 Mv accelerator.

As the half-life of ^{12}B is short (25 m sec), and the background from a deuteron bombardment very intense, it was considered essential to use a pulsed beam technique, i.e. alternate bombardment of target and counting of radiation. An elementary calculation showed that maximum efficiency of ^{12}B counting would be achieved for a pulsing cycle extending over about two half-lives (50 m sec) or less.

The arrangement used consisted of a cylinder mounted within the vacuum system in the path of the deuteron beam. A synchronous motor rotated the cylinder, via a Wilson seal shaft, at 300 r.p.m. Four slots in the cylinder allowed the beam to bombard the target during alternate 25 m sec periods. A lamp and photocell arrangement, using the same rotating cylinder as shutter, provided a signal to the master timing circuit which allowed counts to be recorded only while the beam was off the target.

The master timing circuit consisted essentially of electronic gates which intercepted pulses in appropriate parts of the counting circuits (see fig. 2). An additional function (not shown in fig. 2) performed by the master timing circuit was to switch off the scintillation counters while the deuteron beam was bombarding the target. The immense count rate during bombardment was liable to cause instability in the photomultiplier gain. Switching of the photomultiplier was obtained by applying a 120 volt, 20 m sec long rectangular pulse to the first dynode ; during the pulse the voltage of the first dynode was pulled below that of the second dynode so that the photomultiplier gain was zero.

In the following sections, no further mention will be made of the pulsed beam technique, as this system was used for all measurements.

§ 3. COMPARISON OF ^{12}B AND ^{8}Li

Any attempt to detect γ-radiation following the β-decay of ^{12}B, or any other high energy β emitter, has special difficulties. Absorbers can be used to prevent the γ-counters detecting the β-particles directly, but only at the cost of a considerable intensity of bremsstrahlung (even for materials such as wax or graphite). Anti-coincidence techniques are possible, but in practice it was found difficult to achieve the necessary 100% counting efficiency for the β-detector.

A unique solution to this difficulty was found in the remarkable similarity of the β-spectrum of ^{8}Li to that of ^{12}B, together with the knowledge that there is little or no nuclear γ-radiation associated with the ^{8}Li decay. Bunbury (1953) has put an upper limit of 0·8% on the existence of β–γ coincidences from ^{8}Li and this was confirmed in the experiments to be described.

Figure 1 compares the two β-spectra normalized to the same total count. The ^{12}B spectrum has rather more high energy β-particles than the ^{8}Li spectrum. The agreement, however, is sufficiently good to justify using ^{8}Li for measuring the bremsstrahlung background while looking for nuclear γ-radiation from ^{12}B. An approximate calculation, described in the Appendix, showed that the ^{12}B β-particles would give a bremsstrahlung intensity per β-count in excess of that from ^{8}Li by about 21%.

Fig. 1

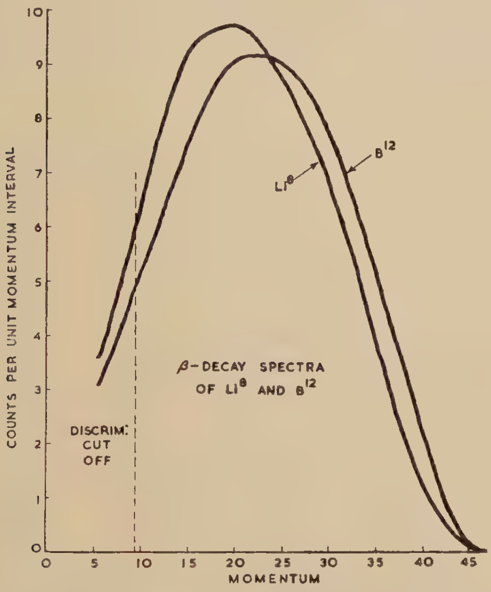

Comparison of the β-spectra of ^{12}B and ^{8}Li normalized to the same total count for momenta greater than the discriminator cut-off. (After Hornyak and Lauritsen 1950.)

Thick Li_2SO_4 targets were used for producing the 0·9 sec ^{8}Li activity via the $^{7}Li(d, p)^{8}Li$ reaction. A target mounting was arranged, with lithium on one side and boron on the other, which could be reversed without opening the vacuum system. For a given deuteron energy and current, the equilibrium β-activities of ^{8}Li and ^{12}B were very much the same. The targets could be distinguished by the lifetimes of the activities.

§ 4. β–γ Coincidences

The arrangement of electronics and counters is illustrated in fig. 2. Detectors used were sodium iodide scintillation counters and a small, thin-walled proportional counter filled with argon to 60 cm pressure. A feature of especial interest was the use of a proportional counter/scintillation counter telescope for detecting the energetic β-particles. The scintillation counter allowed the use of a fast coincidence circuit (0·02 μsec) with the invaluable reduction of random coincidences. At the same time, the proportional counter distinguished genuine β-particles from γ-radiation (bremsstrahlung) or neutron-induced ^{128}I activity in the NaI crystal itself.

Pulses from the γ-scintillation counter were gated to a Hutchinson-Scarrott pulse height analyser, the gating condition being that simultaneous counts (within the resolving times indicated) are recorded in the proportional counter and β-scintillation counter. Use of the pulse height analyser is vital to the experiment, as it is only in this way that the energy of the γ-radiation can be identified. Energy calibration was obtained using ThC″ and Po–Be sources. In addition the Po–Be was used for absolute efficiency calibrations as its activity was known to a 10% accuracy.

Fig. 2

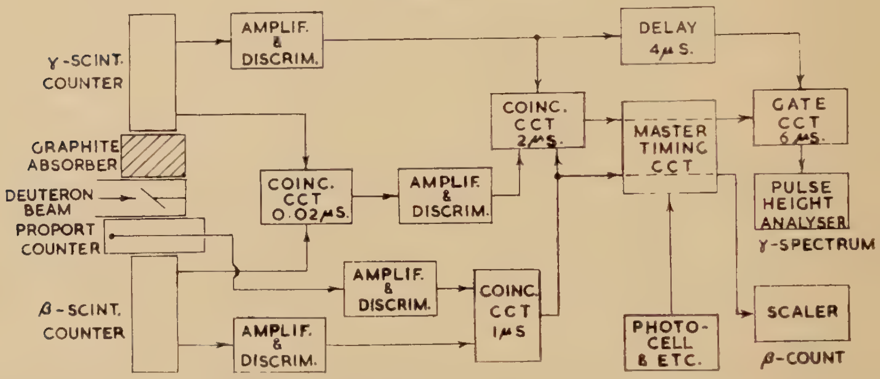

Block schematic diagram of electronic and counter arrangement for β–γ coincidence measurements.

Counting was carried out one hour at a time, alternate hours being used for a total coincidence count and a random coincidence count; the latter was arranged by the introduction of a 0·05 μsec delay one side of the fast coincidence circuit. Coincidences between the proportional counter and β-scintillation counter were recorded on the scaler and served to monitor the β-activity. The spectrum on the pulse height analyser was recorded photographically. For those runs in which comparison with ^{8}Li was made, the ^{8}Li, ^{12}B counts were alternated.

Initially measurements were made with pulse height discrimination such that only those β-particles with energy $\geqslant 2$ Mev were recorded. Even without ^{8}Li for comparison, a 4·4 Mev γ-line could be identified. Figure 3 shows coincidence γ-spectra from ^{12}B and ^{8}Li, normalized to the same β-count, together with the calibration γ-line from Po–Be. The apparent 4·4 Mev γ-radiation could arise by a β-transition either to the 4·43 Mev level of ^{12}C or to the level at 7·66 Mev with subsequent γ–γ cascade decay. In the latter case a 3·2 Mev γ-radiation must also occur.

From the data shown in fig. 3 an upper limit could be placed on the occurrence of a 3·2 Mev radiation and hence a β-transition to the 7·66 Mev level of ^{12}C. Relative to the ground state β-transition this limit is $\leqslant 0{\cdot}3\%$. Assuming zero transition to the 7·66 Mev level, a $(1{\cdot}7 \pm 0{\cdot}4)\%$ transition to the 4·43 Mev level is indicated. These figures represent the mean of several measurements interpreted in the light of the ^{8}Li/^{12}B comparison spectra of fig. 3. Correction was made for the effect of the finite discriminator bias on the relative counting efficiency for ground state and excited state β-spectra.

Figure 3 also serves to justify the use of ^{8}Li for comparison, in that the spectrum indicates that $\leqslant (0{\cdot}2 \pm 0{\cdot}1)\%$ of the ^{8}Li β-transitions are followed by a ~4·9 Mev γ-radiation.

Fig. 3

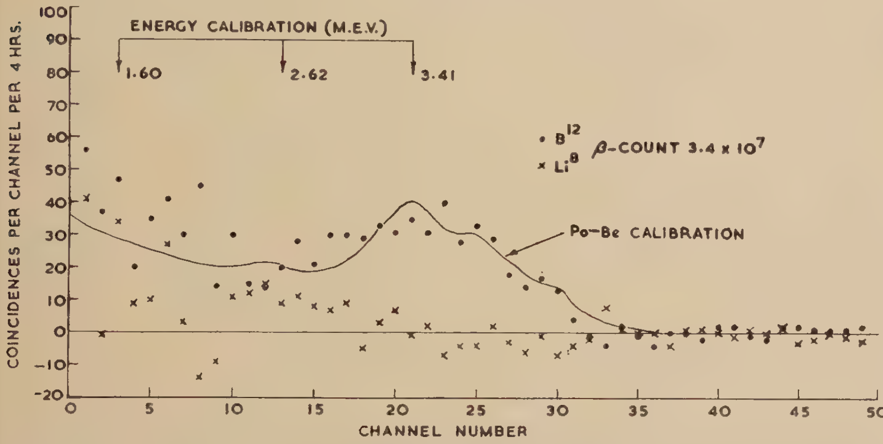

Spectrum of γ-radiation in coincidence with β-particles of energy greater than 2 Mev. (Negative counts are a result of subtracting random coincidences.)

Further β–γ coincidence spectra were taken with the discriminators set to exclude β-particles with energy $\leqslant 5{\cdot}7$ Mev, i.e. the end point energy of a ^{12}B β-transition to the 7·66 Mev level of ^{12}C. Statistics of these counts were so bad that they added little but qualitative evidence to the impression that a β-transition does take place to the 4·43 Mev state of ^{12}C.

A simple re-arrangement of the electronics served to display the β-spectrum, from the β-scintillation counter, on the pulse height analyser. However, even with the coincidence condition of a γ-radiation of energy $\geqslant 3{\cdot}3$ Mev, no useful information was obtained. The broad nature of the β-spectra makes the identification of end point energies very inexact unless good statistical accuracy can be achieved.

§ 5. γ–γ Coincidences

The technique for this experiment involved the use of two scintillation counters (both with graphite β-absorbers), fast coincidence circuit and pulse height analyser, similar to that described in § 4. In this case, however, the output from one counter was fed to the analyser under the conditions that a coincidence occurred and that the pulse height from the other counter corresponded to a γ-ray of energy between 3·3 and 4·5 MEV. The proportional counter was used to monitor the β-activity.

The problems of bremsstrahlung background and low coincidence rates are very much greater in the case of γ–γ as compared to β–γ measurements. Even with the counters set 180° apart (an obvious minimum for bremsstrahlung effects and the expected maximum for γ–γ coincidences from the 7·66 MEV state of ^{12}C (Seed 1955)) the bremsstrahlung coincidences were sufficient to mask completely any nuclear γ-radiations. This was clearly demonstrated by a measurement of the angular correlation which fitted the form cosec$^2\,\theta/2$, i.e. coincidence rate proportional to the inverse square of distance between the two counters: perhaps explicable in terms of Compton scattering of a bremsstrahlung photon or double bremsstrahlung interaction by a single electron; nuclear γ–γ coincidences are quite clearly excluded.

Fig. 4

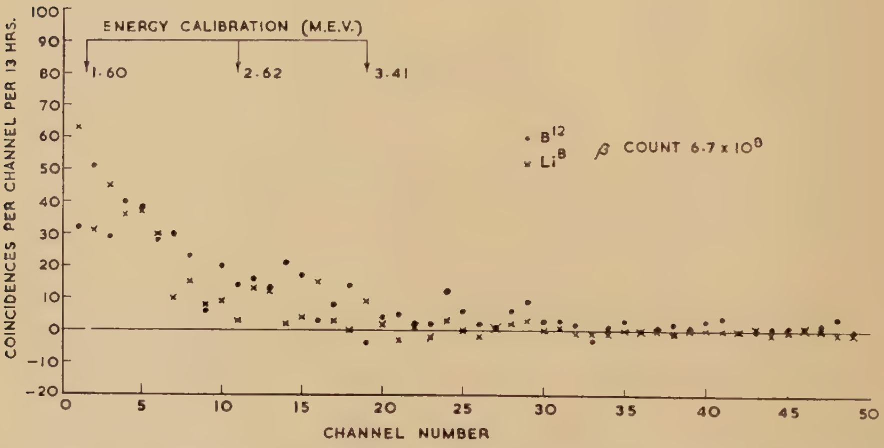

Spectrum of γ-radiation in coincidence with another γ-radiation of energy between 3·3 and 4·5 MEV. (Negative counts are a result of subtracting random coincidences.)

Rather more interesting results were obtained by the ^{8}Li/^{12}B comparison. Figure 4 shows the coincidence γ-spectra normalized to the same monitor β-count. The main characteristic of the two curves is their similarity although the ^{12}B count is significantly greater. Taking the difference between the two curves gives an upper limit value for a ^{12}B($\beta\gamma\gamma$)^{12}C process relative to ^{12}B(β)^{12}C as 0·47%. If however we allow 21% more bremsstrahlung photons per β-count from ^{12}B as compared to ^{8}Li (see Appendix), then the upper limit for a nuclear γ–γ cascade is reduced to (0·04 ± 0·20)%, where the error is that from counting statistics alone.

§ 6. DISCUSSION

The evidence presented indicates that the β-decay of ^{12}B goes primarily to the ground state of ^{12}C but with $(1{\cdot}7 \pm 0{\cdot}4)\%$ branch to the 4·43 MeV level. Transitions to the 7·66 MeV level are excluded to the order of an upper limit of $(0{\cdot}04 \pm 0{\cdot}20)\%$, provided that the state does decay only by γ–γ cascade. Uebergang (1954), Beghian *et al.* (1953) and Seed (1955) all support this contention (the factor of three discrepancy between Uebergang and Beghian *et al.* is merely instrumental in that it arises from the use of a thick target by the latter workers). Rasmussen *et al.* (1955) on the other hand conclude from a study of inelastic scattering of α-particles by ^{12}C, that the 7·66 MeV level of ^{12}C decays to α-particles with a probability of at least 80%; however, it is not clear that their observations might not have been confused by a strong angular distribution and an unfortunate choice of angle.

The allowed β-transition to the 4·43 MeV state of ^{12}C (allowed since ^{12}B ground state is $(1, +)$ and ^{12}C first excited state is $(2, +)$) has $\log ft = 5{\cdot}1$. Assuming the 7·66 MeV level of ^{12}C decays solely by γ–γ cascade, then the β-transition to this state has $\log ft \geqslant 5{\cdot}6$.

The interpretation of the β-spectrum (Hornyak and Lauritsen 1950) has already been discussed in § 1. From the coincidence results, it seems that analysis in terms of a 5% transition to the 7·66 MeV level of ^{12}C, is quite definitely incorrect.

ACKNOWLEDGMENTS

It is a pleasure to acknowledge many helpful discussions with Dr. A. P. French and Professor W. A. Fowler. I am indebted to the Royal Commission for the Exhibition of 1851 for an Overseas Scholarship.

APPENDIX

Difference of Bremsstrahlung from ^{8}Li *and* ^{12}B

Heitler (1947, p. 168) gives the extreme relativistic approximation to the cross section $\phi(k, E)$ for the emission of a bremsstrahlung photon of energy between k and $k+dk$ by an electron of energy E as

$$\phi(k, E) \sim \left[\frac{4(E-k)}{3k} + \frac{k}{E}\right]\left[\log \frac{2E(E-k)}{\mu k} - \frac{1}{2}\right].$$

We are interested in a particular value of k, say 3 MeV, but all values of E from initial energy $E = E_0$ down to $E = k$ as the electron loses energy by inelastic collisions in the absorber (ionization loss is far more important than bremsstrahlung loss for $\sim$10 MeV electrons in graphite). Hence the required cross section is

$$\Phi(k, E_0)= \int_k^{E_0} \phi(k, E)\, dE.$$

Unfortunately the integral cannot be handled analytically, but a graphical method gave the result

$$\Phi\sim(E_0-k)^{2\cdot 6}.$$

It is now necessary to integrate the product of $\Phi(k, E_0)$ and the function $N(E_0)\, dE_0$ which describes the β-spectrum of ^{8}Li or ^{12}B shown in fig. 1. The integrals obtained, again by the graphical method, are proportional to the number of bremsstrahlung photons of energy k per β-particle count. The ratio of the ^{12}B integral to that for ^{8}Li was 1·21 for k=3 MeV.

REFERENCES

BEGHIAN, L. E., HALBAN, H. H., HUSAIN, T., and SANDERS, L. G., 1953, *Phys. Rev.*, **90,** 1129.
BANBURY, D. St. P., 1953, *Phys. Rev.*, **90,** 1121 ; **91,** 1580.
CHRISTY, R. F., 1952, *Proc. Rochester Conference*, p. 4.
HEITLER, W., 1947, *Quantum Theory of Radiation*, 2nd Ed. (Oxford : University Press), p. 161 *et seq.*
HORNYAK, W. F., and LAURITSEN, T., 1950, *Phys. Rev.*, **77,** 160.
RASMUSSEN, V. K., MILLER, D. W., and SAMPSON, M. B., 1955, Pre-print to be published (courtesy of W. A. Fowler).
SEED, J., 1955, *Phil. Mag.*, **46,** 100.
UEBERGANG, R. G., 1954, *Aust. J. Phys.*, **7,** 279.
VENDRYES, G., 1951, *C. R. Paris*, **232,** 1549 ; **233,** 391 ; 1952, *Ann. de Phys.* (12), **7,** 655.

V. *The Measurement of the Angular Diameter of Two Intense Radio Sources*

I: A Radio Interferometer using Post-Detector Correlation

By R. C. Jennison and M. K. Das Gupta
University of Manchester, Jodrell Bank Experimental Station, Cheshire*

[Received July 6, 1955]

SUMMARY

A description of a practical interferometer system based on the principle of post-detector correlation is followed by a short account of an instrument incorporating this principle. This instrument has been used at Jodrell Bank for measurements of the angular diameters and structures of the radiation from the quiet sun and the sources Cygnus and Cassiopeia. The method of computing the results is indicated, and a short account is given of a synthetic source which is used to calibrate the equipment. Reference is made to a method of obtaining the gradient of the correlation function by the use of three adjacent operating frequencies. The results of the measurements on Cassiopeia and Cygnus are given in Part II of this paper.

§ 1. INTRODUCTION

EARLY attempts to measure the angular diameters of the localized radio sources (radio stars) by using interferometer techniques were unsuccessful, and only an upper limit of six minutes of arc could be placed on their size (Ryle and Smith 1948). In anticipation that the sources might subtend angular diameters comparable to those of the visible stars, a new interferometer technique was proposed by Hanbury Brown for measuring the angular diameter of the two most intense radio stars, Cygnus and Cassiopeia. The present paper describes the development of the interferometer and of a small prototype of the instrument which was used to test the principle in a model experiment to determine the diameter of the solar disc at a frequency of 125 Mc/s. An improved full scale instrument was completed in 1952 and applied to the measurement of the angular diameters, and later the fine structures, of the sources in Cygnus and Cassiopeia. The results of these measurements are reported in part II of this paper.

The principle and the theory of the interferometer have been discussed in detail by Hanbury Brown and Twiss (1954). The system does not require coherent local oscillators in the two receivers but relies upon the coherence of the noise spectra formed after the signals in each receiver have been fed into separate square law detectors; for this reason it has been termed a post-detector interferometer. The instrument may be used on very extended baselines; it is capable of a much higher resolving power than previous interferometers and is not seriously affected by ionospheric scintillation.

---

* Communicated by Professor A. C. B. Lovell, F.R.S.

§ 2. The Post-Detector Interferometer

The basic arrangement of the post-detector interferometer is illustrated in the schematic diagram of fig. 1. The aerial systems A_1 and A_2, spaced at a distance d apart, are connected to two independent receivers having identical characteristics. The receivers are double superheterodynes, both tuned to 125 Mc/s and have a radio frequency bandwidth of 200 kc/s. The bandwidth is accurately determined in the final I.F. strip of each receiver immediately prior to a square-law detector.

Fig. 1

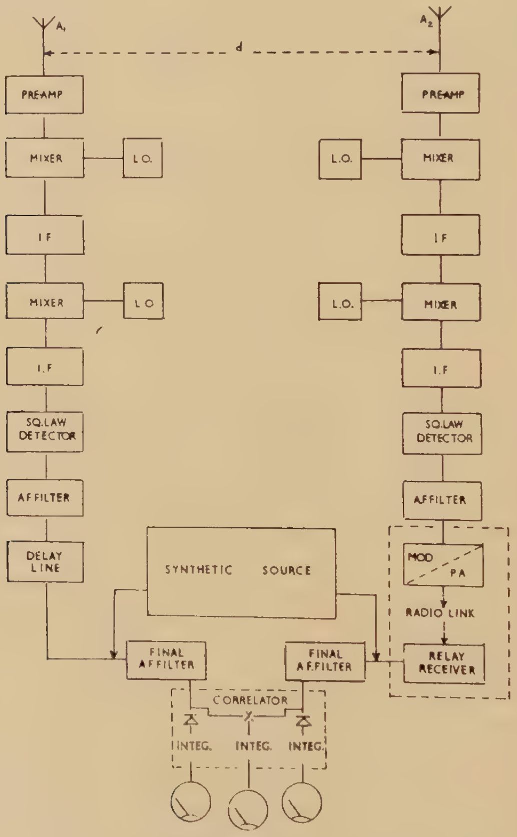

Block diagram of the post-detector interferometer.

The application of a ‘ white ’ noise spectrum to one of the non-linear detector elements produces a system of beat frequencies in the output. These beat frequencies are then passed through a low frequency filter of pass band 1 kc/s to 2·5 kc/s. The outputs from both receivers are treated in a similar manner and the two low frequency outputs are then fed into a common mixer or correlator unit. The function of the correlator is essentially to record the r.m.s. levels, $(\overline{E_1^2})^{1/2}$ and $(\overline{E_2^2})^{1/2}$, and the scalar product, $\overline{(E_1E_2)}$, of the two sets of signals present in the low frequency outputs of the two receivers. From these three parameters the cross correlation coefficient (ρ^2) of the two low frequency spectra may be computed. It can be shown (Hanbury Brown and Twiss 1954) that the function

$$\rho^2 = \frac{F^2 \sin(\omega_0 d/c) + F^2 \cos(\omega_0 d/c)}{F^2 \cos(0)}$$

where ω_0 is the angular frequency to which the aerials are tuned, d is the baseline of the interferometer, and c is the velocity of light. The functions $F_{\sin}$ and $F_{\cos}$ refer to the sine and cosine terms of the Fourier transform of the angular distribution of intensity across the source. Hence by varying the spacing of the aerials, the angular diameter of the source may be computed, and subject to assumptions of symmetry, the intensity distribution may be determined.

In operation the two aerials A_1 and A_2 are each fixed in azimuth and in the same plane of polarization and are adjusted in elevation to the declination of the source. As the source transits across the aerial beam, the increments in the root mean square values of the low frequency outputs together with their scalar product are recorded on a three pen recorder. The value of the cross-correlation coefficient is then obtained from an analysis of the three records.

When a large aerial spacing is used the low frequency output of the distant receiver is transmitted over a radio link by modulating a high frequency carrier. The time of arrival of the two low frequency outputs at the correlator is equalized by inserting in the output of the local receiver a delay equal to the time of transmission along the baseline. As all the parameters in the receivers are identical, the recorded correlator output of the product will be a maximum when the signals entering the receiving aerials are identical, but will diminish with the intensity of either and with the phase shift between their spectra after detection. It is essential that all the components in the equipment should preserve the relative phase of the two low frequency signals, but the problem is considerably simpler in practice than the preservation of the relative phase of the radio frequency signals in conventional interferometers.

The background level of noise in the two receivers is entirely uncorrelated and hence does not contribute to the mean value of the correlation. The effect is, however, to produce a random background of noise in the channel recording $\overline{(E_1E_2)}$, and it is largely this factor which finally limits the sensitivity and resolution of the equipment.

§ 3. DESCRIPTION OF THE APPARATUS

(*a*) *Aerial System*

A high level of resolution may be obtained with the post-detector correlation interferometer provided that the signal to noise ratio in each channel is of the order of unity, but the resolution falls off severely at lower signal levels. In order to achieve a signal to noise ratio of the order of unity from the radio sources Cassiopeia and Cygnus on an operating frequency of 125 Mc/s each aerial was required to have a gain of 600 over a half-wave dipole.

The necessity of moving one of the aerial systems to various sites, in order to determine the variation of correlation with baseline separation, dictated the adoption of a prefabricated antenna which could be readily dismantled and re-erected. The most satisfactory solution was found to lie in a collinear broadside array of full wave dipoles, comprising 320 separate elements fed in 16 bays by equal lengths of coaxial cable. The overall dimensions of each aerial were 128 ft. × 42 ft. and the corresponding beam widths between half-power points were $2\frac{1}{2}°$ in Right Ascension and 11° in declination. The aerials could be tilted about central tripods so that both Cassiopeia and Cygnus were received in the centres of the beams. When it was necessary to dismantle one of the aerials and re-erect it on a new site the whole structure could be collapsed into 32 separate flat units which were readily transportable.

(*b*) *Receivers*

The main requirements for the receiving systems were that the bandwidths and local oscillator frequencies should be accurately matched. The law of detection had to be the same in both channels and the law itself had to be accurately known or calibrated. In order to maintain equal bandwidths in the two receivers a double superheterodyne system was employed in which the gain was accomplished in a broad band intermediate frequency amplifier at 10 Mc/s, whilst the bandwidth was dictated by a single damped tuned circuit at 2·1 Mc/s. These tuned circuits were accurately matched in the two receivers and were arranged to give identical bandwidths over the whole of their response down to −40 dB. The overall bandwidth at −3 dB was 200 kc/s.

The square law detectors each consisted of two pentode valves, type 6B8, operated with the screens regulated at 105 volts and the control grids biased at −13·5 volts. The signal was applied in antiphase to the two control grids whilst the output was taken across a common load of 10 KΩ in the anode circuit. This arrangement rejected the first, third and fifth order harmonics whilst the low level of the fourth order yielded an accuracy of approximately ±0·5% over an input excursion of ±5 volts.

The final stages of the receivers were filter units, defining a low frequency bandwidth of 100–6000 c.p.s. from the output of the square law detectors, and associated amplifiers and cathode followers to feed in one case into the relay transmitter and in the other case directly into the correlator.

(*c*) *Relay System*

The output of the receiver at the distant station consisted of signal and noise frequencies in a band from 100–6000 c.p.s. These were relayed to the home station by a radio link operating on a frequency of 83 Mc/s.

The relay transmitter was crystal controlled and could be operated at a maximum input of 300 watts. The slight phase dispersion occurring in the modulator was compensated by a network having the same characteristics in the opposite limb of the equipment. The radio frequency output of the transmitter was fed into a vertically polarized corner aerial which was beamed towards the home station.

The relay receiver was a superheterodyne, crystal controlled to the transmitter frequency and equipped with a powerful automatic gain control.

(*d*) *Compensation Network and Final Filters*

It was essential that the signals fed into the final correlator unit should be accurately contained in identical bandwidths and that the phase and amplitude dispersion over these bandwidths should be a minimum. The relay system introduced a slight dispersion in one channel and this was compensated by a network of identical characteristics in the opposite channel, where provision was also incorporated for introducing an adjustable time delay to compensate for the delay in the transmission of the signal between the two stations. The delay lines were tapped ladder networks working into matched loads and were capable of a maximum delay of 300 μ sec with a level response up to 10 000 c.p.s. ; they were originally designed for use with anticipated baselines of the order of a hundred kilometres. The delay incurred with a baseline of 12 km., the longest baseline involved in the present experiments, was 40 μ sec corresponding to a phase shift of 14° at 2000 c.p.s.

At this stage the final video bandwidth was defined between 1000 and 2000 c.p.s. by accurately matched resistance–capacity ladder filters. An improvement in the general signal to noise ratio could have been achieved by increasing this bandwidth, but only at the expense of further complications incurred in maintaining a low phase dispersion.

(*e*) *The Correlator*

The correlator accepted the signals from the final filter units in the band from 1000 to 2500 c.p.s. and converted them into their root mean square readings for display on two of the pens of a three pen recorder. To the third pen it fed a signal corresponding to the mean value of the product between the two inputs. The r.m.s. recordings were obtained by rectifying the signals and integrating with a suitable time constant. The rectified signal level was arranged to be sufficient to give full scale deflection of the recording instruments without the need for d.c. amplification.

The operation of the multiplier unit may be understood by reference to the diagram in fig. 2. The outputs of the final filter units were connected to the two points A and B, whence one signal was caused to suffer a reversal of phase every 1/30th second before they were combined in an additional mixer. The combined signal at the point C therefore alternately consisted of the sum and difference of the two spectra at A and B,

$$[(E_1)_s+(E_1)_n]\pm[(E_2)_s+(E_2)_n] \quad . \; . \; . \; . \; . \; . \quad (1)$$

where $(E_1)_s$ and $(E_2)_s$ refer to the low frequency signals and $(E_1)_n$ and $(E_2)_n$ to the corresponding noise terms in the two original channels.

Fig. 2

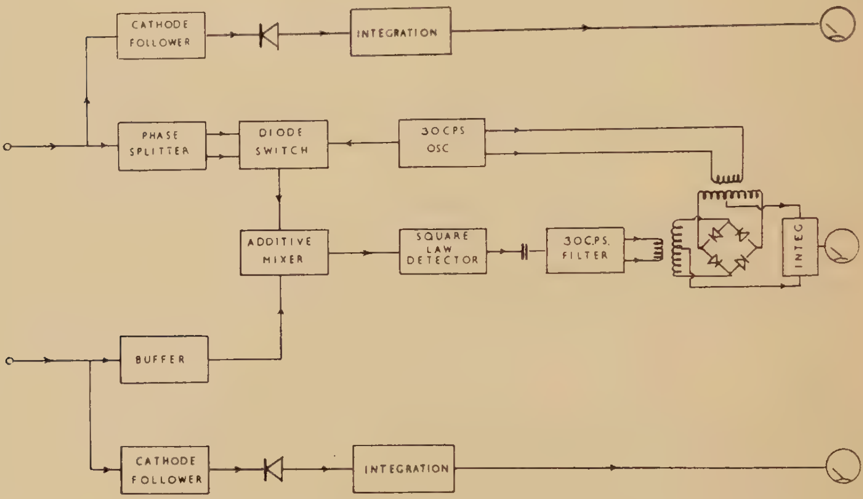

The cross multiplier circuit of the correlator unit.

Upon squaring the signal expressed in eqn. (1) in the following push–push square law detector, and after filtering out the high frequency terms, there remained a constant term proportional to the product

$$\pm(E_1)_s\times(E_2)_s \quad . \; . \; . \; . \; . \; . \; . \quad (2)$$

the polarity of which reversed every 1/30th second in synchronism with the switching waveform. The remaining terms all produced fluctuating signals or were constant without variation at the switch frequency and were largely filtered out in a selective amplifier before being finally presented to a phase sensitive detector. The effect of the latter was to take the difference of the two terms expressed in (2) and, after integration in a simple filter, to feed to the recording meter a signal directly proportional to $\overline{(E_1)_s\times(E_2)_s}$.

§ 4. ASSESSMENT OF CORRELATION, SYNTHETIC NOISE SOURCE

The appearance of the chart after the transit of a source is depicted in fig. 4. The lower record shows the cross modulation product between the components forming the upper two records. As the source is resolved the amplitude of the lower record is reduced whilst those of the upper records remain unchanged. The correlation coefficient (ρ^2) may be computed by measuring the amplitude of the increments $\overline{(E_1^2)}_s^{1/2}$ and $\overline{(E_2^2)}_s^{1/2}$ in the two receiver channels and comparing their product with the observed increment from the third output of the correlator.

Assessment of correlation in this manner requires that the constants of the equipment be accurately known and invariable over long periods. A more reliable method of assessment, which also avoids any possible error in the whole of the correlator system and final filter units, is to introduce, immediately upon the completion of the transit and under identical conditions, a synthetic noise signal whose correlation is known to be unity.

Fig. 3

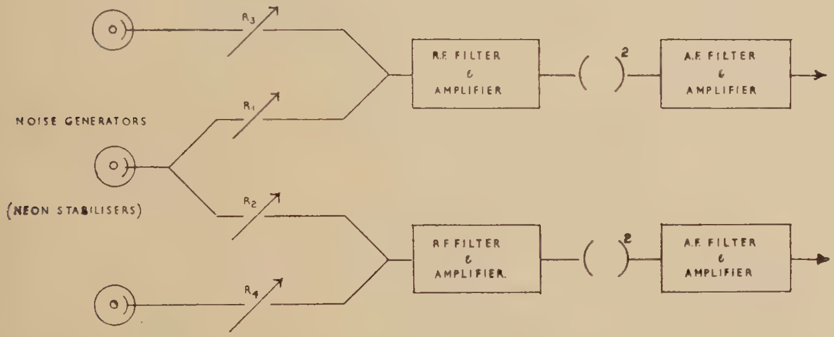

The synthetic source. Adjustments of signal and background noise are made on the controls R_1, R_2, R_3 and R_4 to the left of the diagram.

The correlated component of the synthetic noise signal was produced at a frequency of 200 kc/s in a neon stabiliser tube, whence it was fed separately via two potentiometers, R_1 and R_2 in fig. 3, to two independent but identical radio frequency filter units, having a passband of 150 kc/s at 300 kc/s. Uncorrelated noise signals from the other two neon generators were added independently to each channel through the two gain controls R_3 and R_4 prior to passing through the filter units. The envelope of the noise in each channel was detected by two square law detectors similar to those in the main receivers, and the output frequencies were limited to a similar band by two audio frequency filters of identical characteristics.

The two outputs of the unit were applied to the correlator immediately after the transit of the radio star and the four controls R_1, R_2, R_3, and R_4 were adjusted to give identical conditions in each channel to the actual signal and background noise occurring at transit. An example of the application of this method of calibration is shown to the right of the transit of the source in fig. 4, which depicts a source of 0·65 correlation compared with a synthetic noise signal of unity correlation. The amplitude of the rise in the two intensity recorders is the same for the true source and the synthetic source, but the cross modulation product in the latter case is of almost double the amplitude.

Fig. 4

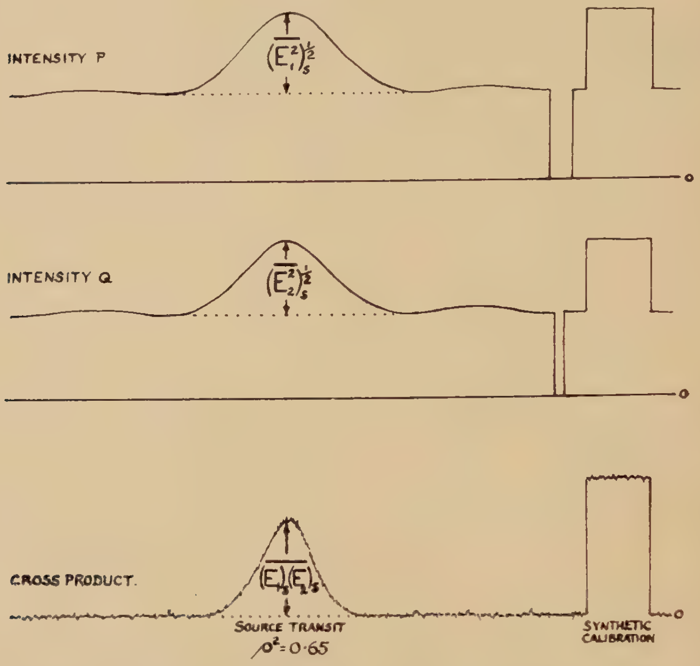

A typical record of the transit of the source in Cassiopeia. The synthetic calibration to the right of the transit shows that the Cassiopeia source had a correlation coefficient $\rho^2 = 0{\cdot}65$ at this aerial separation.

The operation of the synthetic source itself was checked by comparing the correlated output with the correlation of noise in a single audio channel fed into both inputs to the correlator. This enabled the unity point to be compared ; the zero point was checked by applying large uncorrelated inputs in the absence of a correlated signal.

§ 5. FREQUENCY CHANGING

The resolution of the interferometer depended upon the number of wavelengths separating the two aerials. As the aerials were moved apart the resolution increased and the correlation coefficient obtained from the records varied according to the square of the Fourier transform of the intensity distribution across the source. Instead of varying the separation of the two aerials a similar change could be achieved by maintaining a constant aerial separation but varying the frequency of the radio noise selected by the interferometer from the radiation of the source.

Provision was incorporated in the receivers for simple frequency changing so that they could be operated on 116·5, 125, or 132·5 Mc/s, as desired. The three values of the effective baseline (measured in wavelengths) so obtained differed by about 12% and afforded a useful means of measuring the gradient of the correlation function without the need to move the remote aerial system and its associated equipment.

In utilizing this principle it was assumed that the intensity distribution of the radiation across the source was not sharply dependent upon frequency. This assumption was justified for the source in Cassiopeia and Cygnus by noting the effect on a gradient of the transform which had been determined previously by variation of the aerial spacing. Further confirmation is also available by comparing the results of Smith (1952) and Mills (1952) on frequencies of 210 and 101 Mc/s with those obtained on a frequency of 125 Mc/s with the present interferometer.

§ 6. The Equipment in Operation

A prototype of the interferometer was completed in 1951 and the principle of its operation was fully tested with aerial apertures of 100 sq. metres by measurements of the distribution of radiation across

Fig. 5

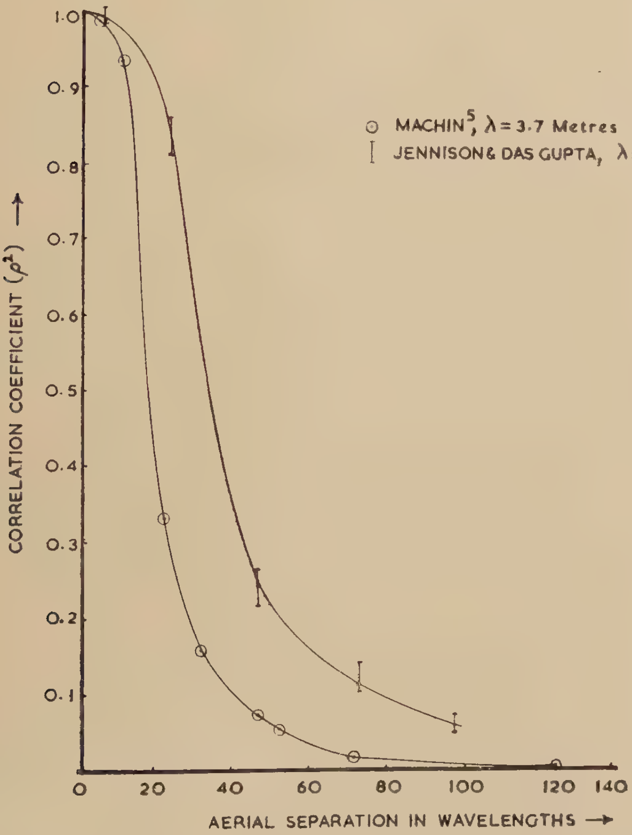

The variation of correlation with aerial spacing observed in the model experiment on the sun. The inner curve is derived from the results of Machin (1951) who used a conventional interferometer on a wavelength of 3·7 metres.

the solar disc on a frequency of 125 Mc/s. The measurements were made at the time of considerable sunspot activity and this contributed a large random error in the readings, together with a systematic increase in the level of correlation at large aerial spacings. A plot of the observed correlation at a number of aerial spacings is shown in fig. 5. The results obtained were consistent with the distribution determined by more conventional techniques, and after minor modification and increase of the aerial aperture the equipment was applied to the measurement of the diameters of the cosmic radio sources Cygnus and Cassiopeia. An extensive series of observations was conducted on these two sources and a detailed account of these observations is given in Part II of this paper. It was found that the equipment operated satisfactorily under all conditions of the experiment and its accuracy was not seriously affected by the presence of severe scintillations. Since both Cassiopeia and Cygnus were resolved at distances much shorter than the extreme baselines which could have been used with this interferometer, the full potentialities of the technique have not yet been realized.

ACKNOWLEDGMENTS

The authors wish to thank Professor A. C. B. Lovell and Mr. R. Hanbury Brown for their encouragement and advice. One of us (R. C. J.) is indebted to the Royal Society for a Mackinnon Studentship during the latter part of this work.

REFERENCES

HANBURY BROWN, R., and TWISS, R. Q., 1954, *Phil. Mag.*, **45**, 663.
MACHIN, K. E., 1951, *Nature, Lond.*, **167**, 889.
MILLS, B. Y., 1952, *Nature, Lond.*, **170**, 1063.
RYLE, M., SMITH, F. G., 1948, *Nature, Lond.*, **165**, 422.
SMITH, F. G., 1952, *Nature, Lond.*, **170**, 1065.

VI. *The Measurement of the Angular Diameter of Two Intense Radio Sources—II : Diameter and Structural Measurements of the Radio Stars Cygnus A and Cassiopeia A*

By R. C. Jennison and M. K. Das Gupta
Jodrell Bank Experimental Station, Cheshire*

[Received September 16, 1955]

Summary

An account is given of the application of the post-detector interferometer to measurements of the radio stars Cygnus A and Cassiopeia A. An outline of the experimental procedure and results is followed by a brief comparison of the photographic and radio frequency distribution of intensity of each source.

§ 1. Introduction

The post-detector interferometer described in the first part of this paper was applied to the measurement of the approximate angular diameters of the intense radio sources in Cygnus and Cassiopeia, and upon the successful completion of this programme it was used to determine the angular distribution of intensity across these sources.

A brief review of the relevant existing information on Cassiopeia and Cygnus is given in table 1.

§ 2. Measurements with the Post-Detector Interferometer

(*a*) *Initial Testing and Calibration of the Instrument*

The new technique was initially tested by performing a model experiment to determine the angular diameter of the solar disc (see Part I). The improved full-scale version of the instrument was then set up on a baseline of 300 metres north–south in order to check the performance of the equipment when recording Cassiopeia and Cygnus.

(*b*) *The Operational Method*

All the measurements described in the succeeding sections were conducted in the following manner. The aerials were adjusted to the declination of the Cygnus source, which was allowed to transit. The receivers were then disconnected and the correlator was calibrated by means of a synthetic source. Two uncorrelated signals were applied and adjusted to give the same background noise as those observed. After a

---

* Communicated by Professor A. C. B. Lovell, F.R.S.

Table 1

		Cygnus	Cassiopeia
Radio source	Flux* watts M^{-2} (c/s)$^{-1}$ at 81 Mc/s	$1{\cdot}35\times10^{-22}$	$2{\cdot}2\times10^{-22}$
	Position† R.A.	$19^{h}\ 51^{m}\ 45^{s}\pm1^{s}$	$23^{h}\ 21^{m}\ 12^{s}\pm1^{s}$
	Dec.	$40^{\circ}\ 35'\pm1'$	$58^{\circ}\ 32{\cdot}1'\pm0{\cdot}7'$
Photographic identification‡	Identified object	Galactic collision	Filamentary emission nebulosity
	Photographic magnitude m_{PG}	15·05	—
	Angular diameter	$18''\times30''$	$6'$
	Distance (old scale)	$3{\cdot}3\times10^{7}$ parsecs	200–2000 parsecs

* Ryle *et al.* (1950). † Smith (1951). ‡ Baade and Minkowski (1954).

short time a correlated signal was also applied and adjusted so that when observed on the two r.m.s. intensity recorders the level on both channels coincided with that observed from the source. The resulting level on the cross multiplier was then measured and the whole calibration procedure was repeated.

The source in Cygnus presented a complication in the uncertainty of the relative levels of the intensity of the radiation from the source and that from the Galaxy. The source is situated on a steeply inclined gradient of the galactic radiation, the uncertainty of the true contour of which masks the true level of the base of the Cygnus transit. The correct level was eventually established by accurately calibrating the contour of the narrow aerial beam in R.A., and also by a detailed analysis of the cross multiplier records, from which the contributions from the localized source could be assessed at all parts of the transit.

A similar procedure to that used on the Cygnus source was carried out for the source in Cassiopeia. Between ten and twenty runs were made on both of the sources at each site and every run was calibrated by means of the synthetic source. Throughout the series of measurements the receiver and relay transmitter were frequently removed to the ‘ home ’ station at Jodrell Bank and tested. Apart from normal testing with signal generators, a method of testing was developed which immediately showed up any loss of correlation in the whole equipment. This method was to split the home aerial into two halves and to apply the two receivers to these. The transit of the Cassiopeia source was then recorded and the equipment was calibrated with the synthetic source to check that it showed unity correlation. The synthetic source itself was checked by reducing the uncorrelated component to zero and comparing the resultant correlation with that obtained by connecting together both the inputs of the correlator and feeding it with the same level of noise from a single channel. A further check was made by removing the correlated signal and increasing the two uncorrelated background noise levels, so that in the absence of a correlated signal the two r.m.s. intensity recorders registered a high reading, whilst the cross multiplier was not deflected.

(*c*) *The Preliminary Diameter Measurements*

The diameter measurements were made on a north–south baseline of 3·9 km with the remote station in a direction 1° east of south. The results showed that the radio sources were both partially resolved. The correlation of the Cygnus source had fallen to about 0·8 whilst that of the source in Cassiopeia had fallen almost to zero. A number of readings were taken to ensure that the results were consistent and the angular widths of both the sources, expressed as the angular widths of equivalent strip sources of constant surface intensity were then calculated. These results, which have already been published (Hanbury Brown *et al.* 1952), showed that the source in Cygnus had an angular diameter of the order of thirty-four seconds of arc, whilst that in Cassiopeia had an angular diameter greater than two minutes of arc.

(*d*) *The Test for Radial Symmetry*

The initial measurements of approximate angular diameter were followed by an investigation into the general shape of the sources. The next series of measurements, which were conducted in the autumn of 1952, were therefore made at a constant aerial spacing along three different azimuths, one of which was chosen to coincide with the north–south azimuth used in the initial diameter measurements. The separation of the aerials was decreased from 3·7 km to 2·16 km in three azimuths inclined to each other at angles of approximately 120°. The reduced baselines were used on the assumption that it would then be possible to obtain correlation coefficients for both sources which were on the steep gradient of the first maximum of the function and which would therefore permit a sensitive measurement of changes in the primary distribution with azimuth.

The values of the correlation coefficients and the equivalent angular strip diameters determined by the measurements along the three axes are given in table 2.

Table 2

Aerial spacing		Cygnus		Cassiopeia	
Distance in km	Bearing degrees from N. (clockwise)	Correlation coefficient * ρ^2	Angular width of equivalent strip	Correlation coefficient * ρ^2	Angular width of equivalent strip
2·16	113	0·30 ± 0·03	2′ 10″ ± 4″	0·08 ± 0·02	2′ 55″ ± 10″
2·16	235·5	0·79 ± 0·08	1′ 10″ ± 7″	< 0·01	≮ 3′ 30″
2·16	176	0·97 ± 0·04	< 30″	0·05 ± 0·03	3′ 20″ ± 15″
3·99	177	0·79 ± 0·07	0′ 34″ ± 8″	< 0·07	unreliable
0·30	349·5	0·99 ± 0·10	< 5′	0·96 ± 0·09	4′ 30″ ± 1′

* The value of ρ^2 is defined in Part I of the present paper.

From these readings it was at once apparent that the source in Cassiopeia was a roughly symmetrical object whilst that in Cygnus was markedly asymmetrical. The Cygnus source was considerably more extended in a direction approximately east–west but it was found that no simple elliptical distribution would fit the observed projections in different azimuths (Hanbury Brown *et al.* 1952).

(*e*) *Measurements of the Intensity Distributions across the Cygnus Source near the Major Axis*

The results for Cygnus, referred to above, did not appear to agree with the measurements made independently by Mills (1952) who concluded that the source exhibited a single central maximum with extensive limb darkening, the half-power width being approximately one minute of arc. The discrepancy could be explained if there was a dip in the correlation function in the neighbourhood of 1200λ, and a series of measurements was therefore made along the previous azimuth of 113° in order to investigate the intensity distribution across the source in a direction close to the major axis.

A modification was made to the equipment in order to obtain the gradient of the correlation function, as the practical difficulties of obtaining small variations in aerial spacing were severe. The modification enabled the equipment to be operated on three alternative frequencies, 116·5, 125 and 132·7 Mc/s. The remote aerial and equipment were removed to a site where operation on these frequencies effectively provided baselines of 1450, 1558 and 1655λ without the necessity of moving the aerials or equipment, and the assumption was made that the source distribution was not sharply dependent on frequency.

The correlation measured at these spacings was very low and the output of the cross multiplier due to the source was of the same order as the noise level of the equipment ; nevertheless it was possible to establish that the correlation function had a positive gradient.

The equipment was then removed to a spacing of 2100λ and the correlation coefficients were again obtained for three values of the effective baseline (Jennison and Das Gupta 1953). Further readings were later taken in the regions of the first maximum, the tail of the second maximum, and the locality of a possible third maximum. No third maximum was measurable although it must be remembered that the equipment was not suitable for the measurement of very small values of correlation and a small third maximum or tailing of the second maximum may exist.

The readings obtained at the various spacings in position angle 113° are tabulated below, whilst the points are plotted for reference in fig. 1.

Table 3. Cygnus Correlation/Aerial Spacing in Position Angle 113°

Aerial spacing in wavelengths	Correlation coefficient (ρ^2)	Aerial spacing in wavelengths	Correlation coefficient (ρ^2)
610	$0{\cdot}460 \pm 0{\cdot}01$	2230	$0{\cdot}290 \pm 0{\cdot}01$
650	$0{\cdot}500 \pm 0{\cdot}05$	2940	$0{\cdot}128 \pm 0{\cdot}008$
900	$0{\cdot}200 \pm 0{\cdot}01$	3140	$0{\cdot}085 \pm 0{\cdot}005$
1450	$0{\cdot}045 \pm 0{\cdot}005$	3350	$0{\cdot}080 \pm 0{\cdot}01$
1558	$0{\cdot}065 \pm 0{\cdot}005$	4650	$< 0{\cdot}025$
1655	$0{\cdot}120 \pm 0{\cdot}01$	5000	$< 0{\cdot}028$
1952	$0{\cdot}245 \pm 0{\cdot}005$	5300	$< 0{\cdot}05$
2100	$0{\cdot}280 \pm 0{\cdot}005$		

Fig. 1

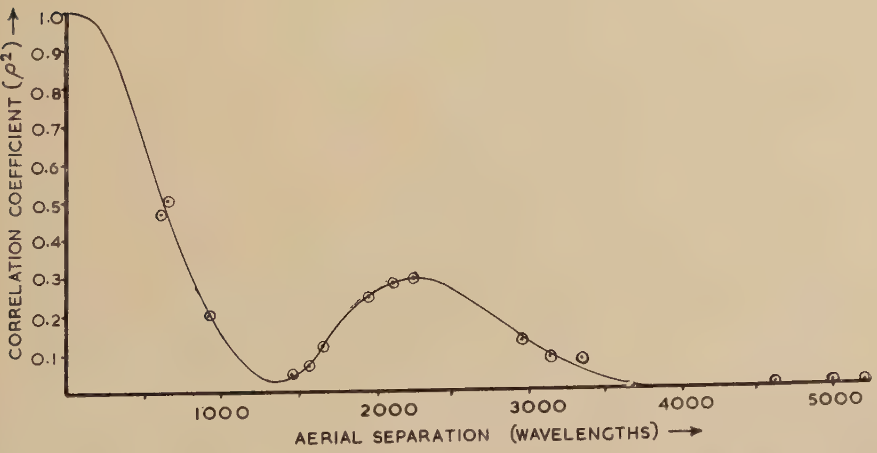

Variation of correlation coefficients with baseline for the intense radio source Cygnus I, measured in position angle 113° at a frequency of 125 Mc/s.

(*f*) *Further Measurements on Cassiopeia*

Subsequent to the initial measurements, which served to confirm the identification, no attempt has been made specifically to investigate the structure of the Cassiopeia source. The post-detection interferometer is unsuitable for measurements of this type and its use is costly and cumbersome at short spacings. Readings were, however, taken concurrently with the Cygnus measurements at extended baselines in position angle 113° to enable a very approximate distribution to be derived. The values of correlation coefficients at these spacings are given in table 4, whilst the points are plotted in fig. 2 with the shorter baseline readings obtained by Smith (1952) at 210 Mc/s in position angle 90°. The earlier establishment of a roughly circular distribution has been taken to justify the plotting of the points on a single graph, though this is only a temporary expedient to obtain the approximate distribution. In combining the readings in this manner it has been assumed that the source structure does not vary greatly between 116·5 Mc/s and 210 Mc/s and that the source is radially symmetrical. These assumptions are severe and further measurements are obviously required.

Table 4. Cassiopeia Correlation/Aerial Spacing in Position Angle 113°

Aerial spacing in wavelengths	Correlation coefficient (ρ^2)	Aerial spacing in wavelengths	Correlation coefficient (ρ^2)
605	$0{\cdot}103 \pm 0{\cdot}004$	2100	$< 0{\cdot}022$
650	$0{\cdot}092 \pm 0{\cdot}003$	3140	$< 0{\cdot}018$
900	$0{\cdot}050 \pm 0{\cdot}006$	5000	$< 0{\cdot}02$
1558	$< 0{\cdot}02$		

Fig. 2

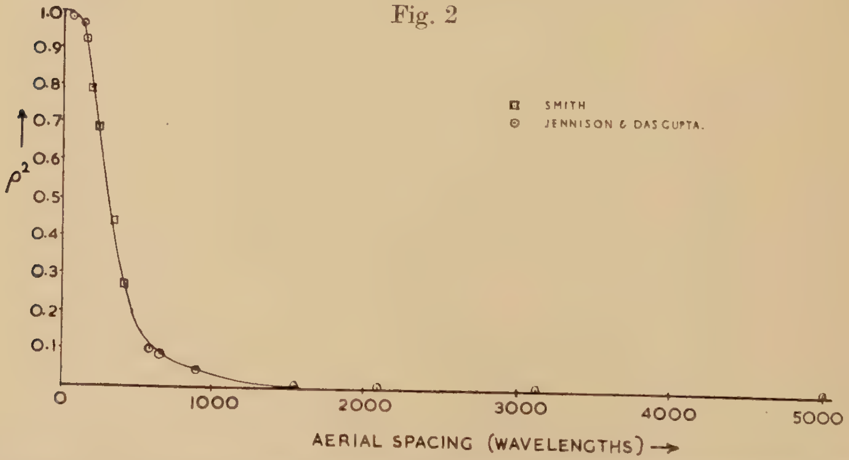

Variation of correlation coefficients with baseline for the radio source Cassiopeia I. The plot is combined from the readings in position angle 113° given in table 4 and the measurements of Smith (1952) in position angle 90°. Perfect symmetry has been assumed and no allowance has been made for the difference in azimuth.

§ 3. DISCUSSION OF RESULTS

(*a*) *Intensity Distribution of the Cygnus Source*

The correlation coefficients obtained for the Cygnus source suggest that the source consists of at least two prominent centres of emission. The curve could be generated by a simple symmetrical function or a complex odd function, and in the absence of phase information the discrimination between the alternatives cannot be made. A symmetrical two-body model of the source distribution which adequately fits the preliminary results is shown in fig. 3. A small amount of limb darkening has been given to the two sources in order to reduce the third maximum, which would otherwise have a value slightly in excess of the upper limit placed on it by the observations. A more complex solution is not proposed until this simple

Fig. 3

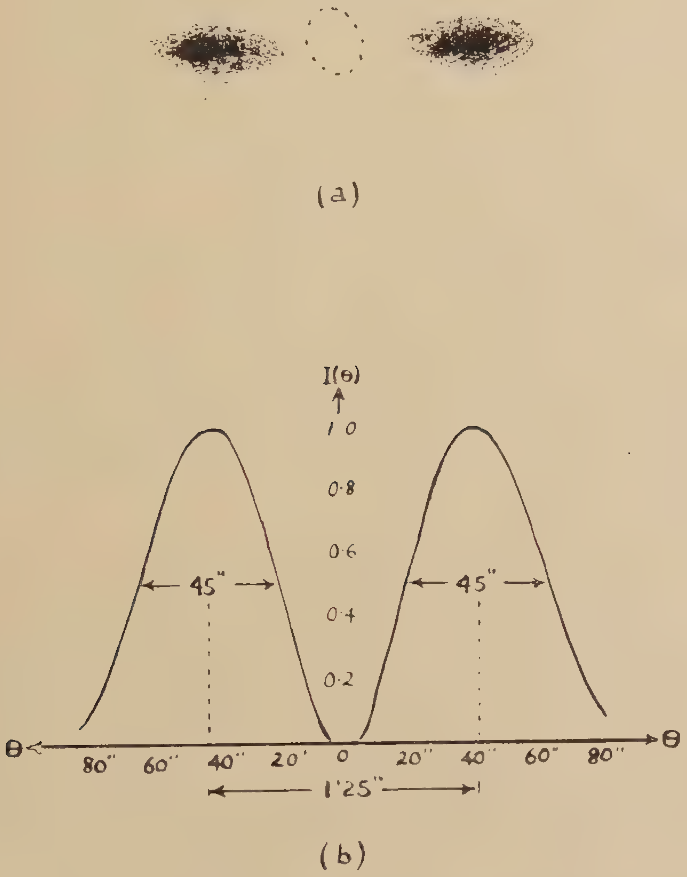

Symmetrical two-body model of the intensity distribution across the Cygnus source. (*a*) Approximate overall distribution of radio intensity, the dotted contour represents the identified galactic collision. (*b*) The distribution of radio intensity in position angle 90°.

interpretation is disproved, for a more complicated model would in general have larger overall dimensions and would be even more difficult to reconcile with the astronomical evidence.

In fig. 4 the measurements made by Smith (1952) and Mills (1952) are recorded on a single plot in which the above measurements have been converted into a position angle along the estimated major axis of the source. The full line in fig. 4 depicts the theoretical correlation function of fig. 3 along the major axis. It will be observed that the original discrepancy of the readings is largely explained if a model similar to that in fig. 3 is employed.

Fig. 4

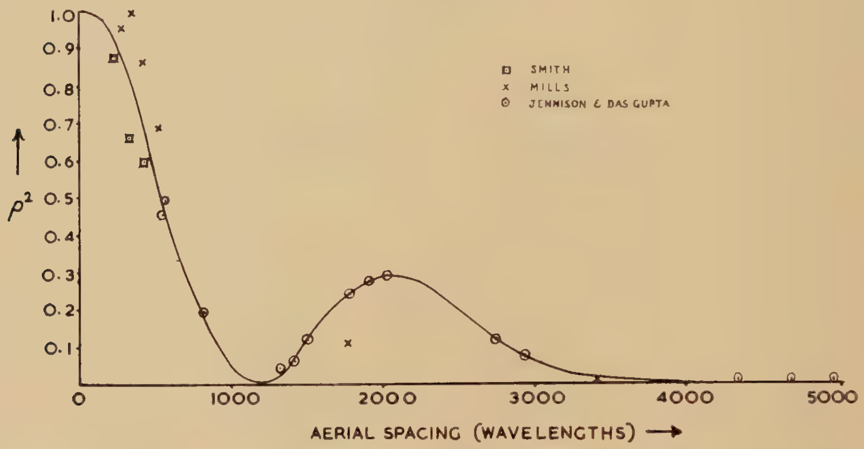

A combined plot showing the variation of correlation coefficients with baseline for the source Cygnus I. The tabulated readings for ρ^2 are given as ordinates whilst the abscissae have been foreshortened by projection on to the approximate position of the major axis. The readings obtained by Smith (1952) and Mills (1952) are shown for comparison. The full line shows the theoretical correlation function of the distribution shown in fig. 3.

There is still some doubt concerning the minor axis of the distribution. Three measurements have been made in the north–south direction and these have yielded an effective strip diameter of 30″. As the width is relatively small a slight discrepancy between the line of measurement and the minor axis itself may lead to a considerable error of assessment, due to the fact that the interferometer measures the projected distribution in any axis. Thus the results could be equally explained if the minor axis is really 30″ in position angle 180° or only a few seconds of arc in a position angle a few degrees away from this azimuth.

(*b*) *Comparison of the Optical and Radio Frequency Distribution of the Cygnus Source*

The radio frequency distribution of the Cygnus source depicted in fig. 3 is very much larger than the optical object and the position measurements indicate that it must be presumed to straddle the position of the colliding galaxies. The dimensions are such that there can be little or no overlap between the regions of intense optical and radio emission and if the identification is correct, this must indicate that radio emission originates in the outermost and most tenuous parts of the galaxies, to the very limit where these might extend. The overall radio dimension in position angle 90° is 2′ 19″, and at a distance of 3×10^7 parsecs this would indicate an actual width of 20400 parsecs which is just feasible for the overall diameter of the galaxies. The new distance-scale would double these figures, but the dimensions could still be consistent with the diameters of normal late type spirals. If any other model than the two-body distribution were chosen it would be necessary to consider a diameter considerably in excess of this figure.

If the visual identification and the interpretation of the radio distribution transform are correct, the most striking feature of the result is the negligible correlation, or possibly negative correlation, between the regions of optical and radio emission. This in turn provides an excellent test for any theories of the radio emission. Not only must the emission arise in the outermost parts but it must shun the bright regions in the centre. It may well be that later measurements will show finer details of the structure in the inner regions, but the presence of two very strong outer components appears to be indisputable. There is a faint possibility that the image of the source has been distorted by the interstellar medium *en route* to the earth, but the effect is unlikely to be serious.

(c) *Equivalent Black Body Temperature of the Cygnus Source*

The approximate evaluation of the Cygnus source distribution enables an estimate to be made of the equivalent surface temperature (T_A) of the source from the known flux incident at the earth. The value of T_A is given by

$$T_A = \frac{S\lambda^2}{2K\int b\,d\Omega}$$

where S is the observed flux, b is the normalized brightness of the source and Ω is an associated element of solid angle. If the first order distribution of the Cygnus source is taken as consisting of two rectangles $50''\times30''$, no limb darkening being assumed, the apparent temperature at 125 Mc/s is $T_A=3\times10^8$ deg. K. This figure is obviously higher than the thermal temperature which would eventually result from the collision. In the initial collision the electron energies are small and, in the absence of radiation, the proton energies may be taken as approximately representing twice the final particle energy on equipartition. Thus for a collision at 1500 km/sec, $T_e\sim5\times10^7$ deg. K. If the mean density is taken as 1 atom/cm³ this corresponds to an absorption coefficient $\sim10^{-10}$ parsec^{-1} and the galaxies viewed face-on should therefore appear optically thin.

If the same source distribution still holds at very much lower frequencies the discrepancy is even greater. An apparent temperature $\sim 10^{10}$ at 30 Mc/s can hardly be reconciled with a simple thermal process at the source.

(*d*) *Intensity Distribution of the Cassiopeia Source*

The most prominent features of the curve in fig. 2 are the long tail and the absence of pronounced subsidiary maxima. A curve of this form would result from the transform of a tapered distribution and if a symmetrical distribution is assumed the source may be considered as having severe limb darkening whilst the long tail could be generated by a smaller intense region situated near the centre of the general distribution. This model is shown in fig. 5 but the interpretation must be treated with considerable uncertainty in view of the small number of useful observations and the assumption of symmetry. There may well be marked deviations from the curve in fig. 2 when more readings have been established, and the distribution in fig. 5 will have to be modified accordingly. If the true curve is complex it is also probable that the phase of the transform will indicate that a symmetrical distribution is not justified.

Fig. 5

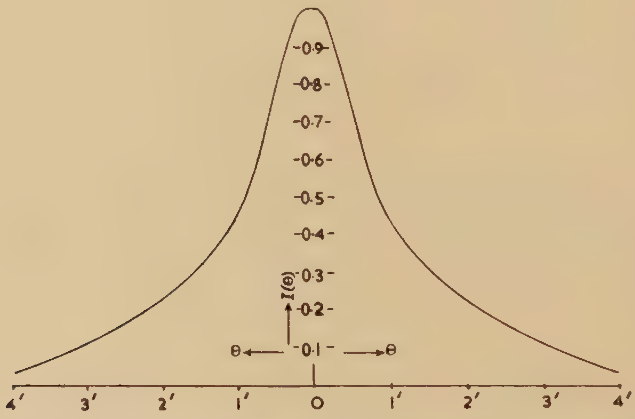

Symmetrical model of the intensity distribution across the Cassiopeia source. This model is given only as a preliminary result and may require extensive modification when investigated with a more powerful technique.

(*e*) *Comparison of the Optical and Radio Frequency Distribution of the Cassiopeia Source*

Some justification for the symmetrical model of the Cassiopeia distribution shown in fig. 5 is provided by the position of the source. The accurate radio position, as measured by Smith (1951) coincides with the centre of the region as a whole, whilst the photographic centre of gravity is considerably removed towards the arch on the northerly limb. The photographic distribution differs in the blue and red, and, as in the blue only the arch and a few diffuse filaments are visible, whilst in the red the arch becomes less prominent and more filaments appear over the whole area, it is apparent that a detailed comparison between the optical and radio frequency distributions must take into account the passband of the photographic filter, whilst it is also possible that the radio frequency distribution may differ at the extremes of the radio spectrum.

Though the accuracy of the present measurement is far too low to permit a detailed analysis, it is apparent that, as with the Cygnus source, the correlation between regions of optical and radio emission is poor. It is evidently of great importance to investigate the radio distribution more thoroughly, and though the resolution required to discern detail of the size of the optical filaments may prove extremely difficult to obtain, the whole assemblage of filaments in the northerly limb may be more simply resolved from the main body of the nebula.

(*f*) *Equivalent Black Body Temperature of the Cassiopeia Source*

The approximate intensity distribution of the Cassiopeia source may be used to derive the equivalent temperature of the source. The resulting apparent temperature at 125 Mc/s is $\sim 4 \times 10^7$ deg. K over the main body of the structure.

ACKNOWLEDGMENTS

The authors gratefully acknowledge the advice and encouragement of Professor A. C. B. Lovell and Mr. R. Hanbury Brown. One of us (R. C. J.) is indebted to the Royal Society for the Mackinnon Studentship during the latter part of the work.

REFERENCES

BAADE, W., and MINKOWSKI, R., 1954, *Ap. J.*, **119,** 206.
HANBURY BROWN, R., JENNISON, R. C., and DAS GUPTA, M. K., 1952, *Nature, Lond.*, **170,** 1061.
JENNISON, R. C., and DAS GUPTA, M. K., 1953, *Nature, Lond.*, **172,** 996.
MILLS, B. Y., 1952, *Nature, Lond.*, **170,** 1063.
RYLE, M., SMITH, F. G., and ELSMORE, B., 1950, *Mon. Not. Roy. Astr. Soc.*, **110,** 508.
SMITH, F. G., 1951, *Nature, Lond.*, **168,** 555 ; 1952, *Ibid.*, **170,** 1065.

VII. *A Thermodynamic Treatment of Ferroelectricity and Antiferroelectricity in Pseudo-Cubic Dielectrics*

By L. E. Cross
Electrical Research Association, Perivale, Middlesex*

[Received August 10, 1955]

Abstract

The Kittel–Devonshire phenomenological treatment of antiferroelectricity is extended to the case of polarizations in three dimensions in a pseudo-cubic material. There are ten possible solutions of the proposed free energy equation, corresponding to non-polar, ferroelectric, antiferroelectric and ferrielectric states, and expressions are derived for the polarization and dielectric stiffness coefficients in these forms.

Using the experimental data for $NaNbO_3$, values of the constants in the free energy expression are derived which give satisfactory agreement with the observed phase changes, optical anisotropies and dielectric constants in this material. It is also shown that the major features of the phase diagram for $(NaK)NbO_3$ solid solutions are reproduced from the $NaNbO_3$ free energy expression if T_a, the antiferroelectric 'curie' temperature decreases linearly with increasing $KNbO_3$ concentration. These results are discussed in terms of the spatial relationships in the $NaNbO_3$ and $KNbO_3$ structures, and compared to the properties of the corresponding alkali tantalates.

§ 1. Introduction

The thermodynamics of antiferroelectricity was first studied by Kittel (1951). In this treatment, the dielectric is assumed to contain two equivalent, interpenetrating, polarizable sub-lattices. Designating the sub-lattice polarizations P_a, P_b, the free energy is expressed in the form

$$\Delta G=f(P_a^2+P_b^2)+gP_aP_b+h(P_a^4+P_b^4)+\dots \quad (1.1)$$

There are two possible solutions of (1.1), $P_a=P_b$, a ferroelectric state, and $P_a=-P_b$, an antiferroelectric state. The stable solution is that which gives the least minimum value of (1.1).

Devonshire (1954) shows that it is more convenient to transform (1.1) by putting in new variables

$$\left.\begin{aligned} P&=P_a+P_b. & (a)\\ p&=P_a-P_b. & (b)\end{aligned}\right\}(1.2)$$

The free energy expression then takes the form

$$\Delta G=\tfrac{1}{2}\chi'P^2+\tfrac{1}{4}\xi'P^4+\dots+\tfrac{1}{2}\chi p^2+\tfrac{1}{4}\xi p^4+\dots+\tfrac{1}{2}\lambda p^2P^2+\dots \quad (1.3)$$

---

* Communicated by the Author.

The conditions for stability are

$$\partial \Delta G/\partial P=0, \qquad (1.4)$$

$$\partial \Delta G/\partial p=0, \qquad (1.5)$$

and the dielectric stiffness is given by

$$\chi=\partial^2 \Delta G/\partial P^2. \qquad (1.6)$$

It has been suggested (Kittel 1951, Shirane *et al.* 1951) that $PbZrO_3$, and certain related compounds are antiferroelectric. The thermodynamic method gives a plausible explanation of the dielectric anomalies at the curie temperature in these substances, but its usefulness is limited by lack of experimental data which prevents any detailed evaluation of the coefficients in (1.3).

Recently, more complete experimental data have been published for $NaNbO_3$, and mixed $(KNa)NbO_3$, crystals, and it would appear that a more detailed thermodynamic analysis might profitably be attempted.

§ 2. DEVONSHIRE'S EQUATION FOR A PSEUDO-CUBIC MATERIAL

In (1.3) both P and p are vectors, and in general they need not lie in the same direction. For a pseudo-cubic material (1.3) may be expanded in rectangular coordinates, and takes a reasonably simple form.

Assuming again that the material contains two interpenetrating polarizable sub-lattices with polarizations P_a, P_b, these will have components P_{ax}, P_{ay}, P_{az} and P_{bx}, P_{by}, P_{bz} in the directions of the cube axes x, y, z.

Putting

$$\left.\begin{array}{llll} P_x=P_{ax}+P_{bx} & (a) & p_x=P_{ax}-P_{bx} & (d) \\ P_y=P_{ay}+P_{by} & (b) & p_y=P_{ay}-P_{by} & (e) \\ P_z=P_{az}+P_{bz} & (c) & p_z=P_{az}-P_{bz} & (f) \end{array}\right\} \qquad (2.1)$$

the free energy may be expressed in the form

$$\begin{aligned} \Delta G=&\tfrac{1}{2}\chi_f(P_x^2+P_y^2+P_z^2)+\tfrac{1}{4}\xi_{11}'(P_x^4+P_y^4+P_z^4)\\ &+\tfrac{1}{2}\xi_{12}'(P_x^2P_y^2+P_y^2P_z^2+P_z^2P_x^2)+\tfrac{1}{6}\zeta(P_x^6+P_y^6+P_z^6)\\ &+\tfrac{1}{2}\chi_a(p_x^2+p_y^2+p_z^2)+\tfrac{1}{4}\xi_{11}(p_x^4+p_y^4+p_z^4)\\ &+\tfrac{1}{2}\xi_{12}(p_x^2p_y^2+p_y^2p_z^2+p_z^2p_x^2)+\tfrac{1}{6}\zeta_{111}(p_x^6+p_y^6+p_z^6)\\ &+\tfrac{1}{6}\zeta_{112}(p_x^4p_y^2+p_x^4p_z^2+p_y^4p_x^2+p_y^4p_z^2+p_z^4p_x^2+p_z^4p_y^2)\\ &+\tfrac{1}{2}\zeta_{123}p_x^2p_y^2p_z^2+\tfrac{1}{8}\eta(p_x^8+p_y^8+p_z^8)+\tfrac{1}{2}\lambda(P_x^2p_x^2+P_y^2p_y^2+P_z^2p_z^2)\\ &+\tfrac{1}{2}\theta(P_x^2p_y^2+P_x^2p_z^2+P_y^2p_x^2+P_y^2p_z^2+P_z^2p_x^2+P_z^2p_y^2). \qquad (2.2) \end{aligned}$$

The 'ferroelectric' part of the expression contains all possible terms up to the fourth order, and the first sixth order term. The 'antiferroelectric' part contains all terms up to the sixth order, and the first eighth order term. Only first order interactions between ferroelectric and antiferroelectric are considered.

From (1.4) the conditions for stability in zero external field will be

$$\left.\begin{aligned}
&P_x=0 \text{ or } 0=\chi_f+\xi_{11}'P_x^2+\xi_{12}'(P_y^2+P_z^2)+\zeta'P_x^4+\lambda p_x^2+\theta(p_y^2+p_z^2), && (a)\\
&P_y=0 \text{ or } 0=\chi_f+\xi_{11}'P_y^2+\xi_{12}'(P_x^2+P_z^2)+\zeta'P_y^4+\lambda p_y^2+\theta(p_x^2+p_z^2), && (b)\\
&P_z=0 \text{ or } 0=\chi_f+\xi_{11}'P_z^2+\xi_{12}'(P_x^2+P_y^2)+\zeta'P_z^4+\lambda p_z^2+\theta(p_x^2+p_y^2), && (c)
\end{aligned}\right\} \quad . \quad . \quad . \quad . \quad (2.3)$$

and from (1.5)

$$\left.\begin{aligned}
p_x=0 \text{ or } 0=\chi_a&+\xi_{11}p_x^2+\xi_{12}(p_y^2+p_z^2)+\zeta_{111}p_x^4\\
&+\tfrac{1}{6}\zeta_{112}\{4(p_x^2p_y^2+p_x^2p_z^2)+2(p_y^4+p_z^4)\}\\
&+\zeta_{123}p_y^2p_z^2+\eta p_x^6+\lambda P_x^2+\theta(P_y^2+P_z^2), \quad (a)\\
p_y=0 \text{ or } 0=\chi_a&+\xi_{11}p_y^2+\xi_{12}(p_x^2+p_z^2)+\zeta_{111}p_y^4\\
&+\tfrac{1}{6}\zeta_{112}\{4(p_y^2p_z^2+p_y^2p_x^2)+2(p_x^4+p_z^4)\}\\
&+\zeta_{123}p_x^2p_z^2+\eta p_y^6+\lambda P_y^2+\theta(P_x^2+P_z^2). \quad (b)\\
p_z=0 \text{ or } 0=\chi_a&+\xi_{11}p_z^2+\xi_{12}(p_x^2+p_y^2)+\zeta_{111}p_z^4\\
&+\tfrac{1}{6}\zeta_{112}\{4(p_z^2p_x^2+p_z^2p_y^2)+2(p_x^4+p_y^4)\}\\
&+\zeta_{123}p_x^2p_y^2+\eta p_z^6+\lambda P_z^2+\theta(P_x^2+P_y^2). \quad (c)
\end{aligned}\right\} \quad (2.4)$$

From the symmetry also,

$$\text{if} \quad P_n\neq 0, \quad \text{then} \quad p_n=0. \quad . \quad . \quad . \quad . \quad . \quad . \quad (2.5)$$

$$\text{and if} \quad p_n\neq 0, \quad \text{then} \quad P_n=0, \quad . \quad . \quad . \quad . \quad . \quad . \quad (2.6)$$

where $n=x, y, z$.

There are then ten possible sets of solutions for (2.2).

$$\left.\begin{array}{lll}
P_x=P_y=P_z=0, & p_x=p_y=p_z=0, & (a)\\
\quad 0=\chi_f+(\xi_{11}')P_x^2+\zeta'P_x^4, & P_y=P_z=0, & \\
 & \quad p_x=p_y=p_z=0, & (b)\\
\quad 0=\chi_f+(\xi_{11}'+\xi_{12}')P_x^2+\zeta'P_x^4, & P_x=P_y, \quad P_z=0, & \\
 & \quad p_x=p_y=p_z=0, & (c)\\
\quad 0=\chi_f+(\xi_{11}'+2\xi_{12}')P_x^2+\zeta'P_x^4, & P_x=P_y=P_z, & \\
 & \quad p_x=p_y=p_z=0, & (d)\\
P_x=P_y=P_z=0, & & \\
\qquad 0=\chi_a+\xi_{11}p_x^2+\zeta_{111}p_x^4+\eta p_x^6, & p_y=p_z=0, & (e)\\
P_x=P_y=P_z=0, & & \\
\qquad 0=\chi_a+(\xi_{11}+\xi_{12})p_x^2+(\zeta_{111}+\zeta_{112})p_x^4+\eta p_x^6, & & \\
 & p_x=p_y, \quad p_z=0, & (f)\\
P_x=P_y=P_z=0, & & \\
\qquad 0=\chi_a+(\xi_{11}+2\xi_{12})p_x^2+(\zeta_{111}+2\zeta_{112}+\zeta_{123})p_x^4+\eta p_x^6, & & \\
 & p_x=p_y=p_z, & (g)\\
\quad 0=\chi_f+\xi_{11}'P_x^2+\zeta'P_x^4+\theta p_y^2, & P_y=P_z=0, & \\
\qquad 0=\chi_a+\xi_{11}p_y^2+\zeta_{111}p_y^4+\eta p_y^6+\theta P_x^2. & p_x=p_z=0, & (h)\\
\quad 0=\chi_f+(\xi_{11}'+\xi_{12}')P_x^2+\zeta'P_x^4+\theta p_z^2, & P_x=P_y, \quad P_z=0, & \\
\qquad 0=\chi_a+\xi_{11}p_z^2+\zeta_{111}p_z^4+\eta p_z^6+2\theta P_x^2, & p_x=p_y=0, & (i)\\
\quad 0=\chi_f+\xi_{11}'P_x^2+\zeta'P_x^4+2\theta p_y^2, & P_y=P_z=0, & \\
\qquad 0=\chi_a+(\xi_{11}+\xi_{12})p_y^2+(\zeta_{111}+\zeta_{112})p_y^4+\eta p_y^6+\theta P_x^2. & & \\
 & p_z=p_y, \quad p_x=0. & (j)
\end{array}\right\} \quad (2.7)$$

The stable solution at any temperature will be that which corresponds to the least minimum in the free energy (2.2).

From (1.6) the dielectric stiffness coefficients are given by

$$\left.\begin{aligned}\chi_{xx}&=\chi_f+3\xi_{11}'P_x^2+\xi_{12}'(P_y^2+P_z^2)+5\zeta'P_x^4+\lambda p_x^2+\theta(p_y^2+p_z^2), \quad (a)\\ \chi_{yy}&=\chi_f+3\xi_{11}'P_y^2+\xi_{12}'(P_x^2+P_z^2)+5\zeta'P_y^4+\lambda p_y^2+\theta(p_x^2+p_z^2), \quad (b)\\ \chi_{zz}&=\chi_f+3\xi_{11}'P_z^2+\xi_{12}'(P_x^2+P_y^2)+5\zeta'P_z^4+\lambda p_z^2+\theta(p_x^2+p_y^2). \quad (c)\end{aligned}\right\} (2.8)$$

§ 3. APPLICATION OF THE THERMODYNAMIC TREATMENT TO $NaNbO_3$

To make use of this treatment in $NaNbO_3$, it is necessary to determine the constants in both ferroelectric and antiferroelectric parts of the free energy expression (2.2). The situation is thus more complex than in $BaTiO_3$ and it is necessary to make more direct use of the experimental data than in Devonshire's treatment (Devonshire 1949).

3.1. *Experimental Data*

The necessary data are taken from papers by Cross and Nicholson (1955) for $NaNbO_3$, Shirane, Newnham and Pepinsky (1954) for $NaNbO_3$ and mixed $(NaK)NbO_3$, and Shirane, Danner, Pavlovic and Pepinsky (1954) for $KNbO_3$. In further references in the text, these papers are abbreviated C_1, S_1 and S_2 respectively.

Qualitatively, the following sequence of properties with decreasing temperature is suggested :

(*a*) $T>638$°C	Cubic probably paraelectric.
(*b*) 638°C$>T>$500°C	Tetragonal, almost cubic, the distortion being too small to detect by x-rays, probably paraelectric.
(*c*) 500°C$>T>$350°C	Orthorhombic, almost tetragonal, again the distortion from the higher symmetry may only be detected optically, probably antiferroelectric.
(*d*) 350°C$>T>-$135°C	Orthorhombic (rotated axes) antiferroelectric.
(*e*) -135°C$>T$	Probably monoclinic, probably ferrielectric with antiferroelectric displacements in the a.c. plane, and a ferroelectric polarization along (*b*).

There appears to be some doubt as to the properties near 500°C. C_1 reports minor structure changes at 470°C and 518°C. S_1 a minor change at 480°C. Evidence for the low temperature polarized state below -135°C comes only from C_1 ; S_1 reports no symmetry changes at low temperature but does not appear to have investigated this region in detail.

The general data suggest that the sequence of solutions of (2.2) with decreasing temperature is (2.7(*a*), (*e*), (*f*), (*j*)), and these solutions will be used to evaluate the constants in the free energy expression.

3.2. *Evaluation of Constants in Free Energy Equation*

Following Devonshire 1949, it will be assumed that χ_f is a linearly decreasing function of T, of the form

$$\chi_f=\chi_{f0}(T-T_f) \quad . \quad . \quad . \quad . \quad . \quad . \quad . \quad (3.1)$$

and also that χ_a has the similar form

$$\chi_a=\chi_{a0}(T-T_a) \quad . \quad . \quad . \quad . \quad . \quad . \quad . \quad (3.2)$$

where χ_{f0}, T_f, χ_{a0} and T_a are constant.

In an antiferroelectric, the macroscopic polarization is always zero, so that it is not possible to measure p directly. It is probable, however, that p will be related to the structure distortion, and to the optical anisotropy, and it will be assumed that this relation takes a similar simple form to that found for the ferroelectric polarization in BaTiO$_3$, i.e.

$$p_x^2=\rho\left(\frac{c}{a}-1\right)=K\Delta\mu \quad . \quad . \quad . \quad . \quad . \quad . \quad . \quad (3.3)$$

where ρ and K are constant.

In the orthorhombic form there are two measurable anisotropies. For this work $\Delta\mu_1$ (C$_1$) will be used, as it is the difference between two principle indices.

From (3.2) and (3.3) solutions (2.7(*e*), (*f*)), of (2.2) may be rewritten in terms of $\Delta\mu$ and $\Delta\mu_1$

$$0=(T-T_a)+A\Delta\mu+C\Delta\mu^2+F\Delta\mu^3, \quad . \quad . \quad . \quad . \quad . \quad . \quad . \quad (3.4)$$

$$0=(T-T_a)+(A+B)\Delta\mu_1+(C+D)\Delta\mu_1^2+F\Delta\mu_1^3 \quad . \quad . \quad (3.5)$$

and from (2.2) the free energy in the two states will be

$$\Delta G=K\chi_{a0}\{\tfrac{1}{2}(T-T_a)\Delta\mu+\tfrac{1}{4}A\Delta\mu^2+\tfrac{1}{6}C\Delta\mu^3+\tfrac{1}{8}F\Delta\mu^4\} \quad . \quad . \quad . \quad . \quad . \quad . \quad (3.6)$$

$$\Delta G=K\chi_{a0}\{(T-T_a)\Delta\mu_1+\tfrac{1}{2}(A+B)\Delta\mu_1^2+\tfrac{1}{3}(C+D)\Delta\mu_1^3+\tfrac{1}{4}F\Delta\mu_1^4\} \quad . \quad (3.7)$$

where

$$A=K\xi_{11}/\chi_{a0},\ B=K\xi_{12}/\chi_{a0},\ C=K^2\zeta_{111}/\chi_{a0},\ D=K^2\zeta_{112}/\chi_{a0},\ F=K^3\eta/\chi_{a0}.$$

To evaluate the constants A, B, C, D, F the following procedure is adopted :

(*a*) By the method of least squares, values of T_a, $A+B$, $C+D$, and F are obtained which give a 'best fit' between (3.5) and the experimental temperature variation of $\Delta\mu_1$, in the orthorhombic state (C$_1$).

(*b*) At the transition temperature from orthorhombic to tetragonal structures, the free energies of the two states must be equal, i.e.

$$\tfrac{1}{2}(T_1-T_a)\Delta\mu+\tfrac{1}{4}A\Delta\mu^2+\tfrac{1}{6}C\Delta\mu^3+\tfrac{1}{8}F\Delta\mu^4$$
$$=(T_1-T_a)\Delta\mu_1+\tfrac{1}{2}(A+B)\Delta\mu_1^2+\tfrac{1}{3}(C+D)\Delta\mu_1^3+\tfrac{1}{4}F\Delta\mu_1^4 \quad . \quad (3.8)$$

substituting the experimental values of T_1, $\Delta\mu$, $\Delta\mu_1$ and the constants previously determined in (*a*), (3.4) and (3.8) may be solved for A and C.

The least squares method (*a*) gives a value of $T_a=538$°c ; this is close to the observed minor structure change at 520°c, and assuming this to be the antiferroelectric 'curie' temperature recalculation with $T_a=520$°c gives the values $A+B=1{\cdot}322\times10^4$, $C+D=-2{\cdot}526\times10^5$, $F=2{\cdot}326\times10^6$ and the fit with the experimental $\Delta\mu_1$ shown in fig. 1.

Fig. 1

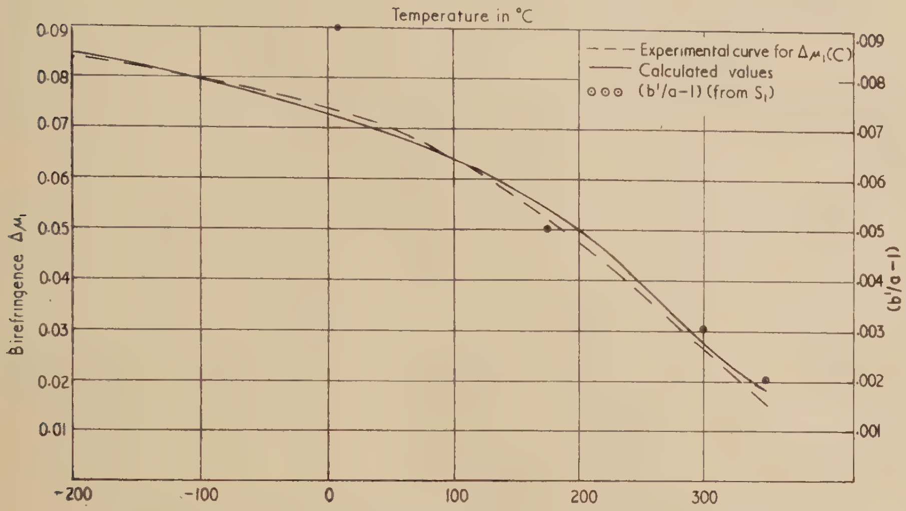

The variation of birefringence with temperature in $NaNbO_3$.

Fig. 2

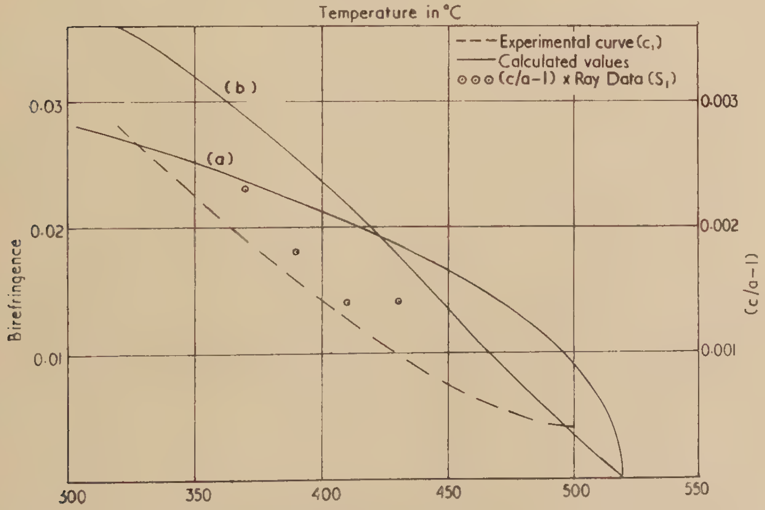

Variation of birefringence with temperature in $NaNbO_3$ (tetragonal).

The experimental value of $\Delta\mu$ at the transition temperature substituted in (*b*) gives values of A and C, which in (3.4) produce a temperature variation of $\Delta\mu$ dissimilar to the observed variation (fig. 2, curve (*a*)).

Using a value of $\Delta\mu=0{\cdot}034$ at the transition, a more similar temperature variation is obtained (fig. 2, curve (*b*)). The difference in scale between observed and calculated values may be due to the oversimplification of using a single value for K in both orthorhombic and tetragonal regions. The values of A and C for $\Delta\mu=0{\cdot}034$ are

$$A=0{\cdot}612\times 10^4, \qquad C=-0{\cdot}989\times 10^5.$$

Using the constants enumerated above, the free energy in units of $K\chi_{a0}$ may be evaluated from (3.6) and (3.7), and is shown in fig. 3 (curves (*a*), (*b*)).

Fig. 3

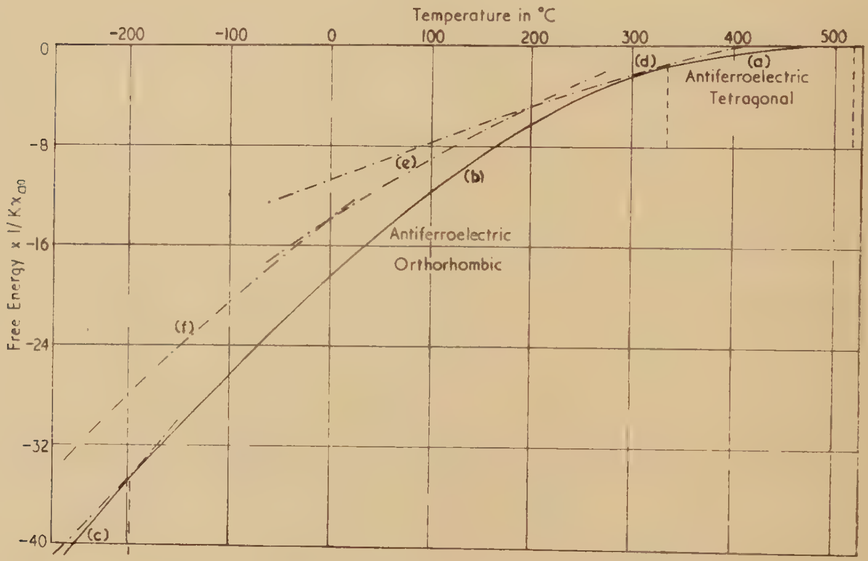

Free energy in $NaNbO_3$ as a function of temperature.

3.3. *The Determination of the Ferroelectric Constants, and the Cross Constants*

The ferroelectric curie temperature T_f, χ_{f0} and the cross constants λ and θ, may be determined from the dielectric constant data.

For solutions (2.7(*a*), (*e*), (*f*)) eqns. (2.8) may be rewritten

$T>520°c$

$$\chi_{xx}=\chi_{yy}=\chi_{zz}=\chi_{f0}(T-T_f) \quad . \quad . \quad . \quad . \qquad (3.9)$$

$520°c>T>320°c$

$$\left.\begin{aligned}\chi_{xx}&=\chi_{f0}(T-T_f)+\alpha\Delta\mu \quad . \quad . \quad . \quad . \quad . \quad . \quad (a)\\ \chi_{yy}=\chi_{zz}&=\chi_{f0}(T-T_f)+\beta\Delta\mu \quad . \quad . \quad . \quad (b)\end{aligned}\right\}(3.10)$$

$350°c>T>-209°c$

$$\left.\begin{aligned}\chi_{xx}=\chi_{yy}&=\chi_{f0}(T-T_f)+(\alpha+\beta)\Delta\mu_1 \quad . \quad . \quad (a)\\ \chi_{zz}&=\chi_{f0}(T-T_f)+2\beta\Delta\mu_1 \quad . \quad . \quad . \quad . \quad . \quad (b)\end{aligned}\right\}(3.11)$$

where

$$\alpha=K\lambda \qquad \text{and} \qquad \beta=K\theta. \quad . \quad . \quad . \quad . \qquad (3.12)$$

The values of the constants χ_{f0}, T_f, α and β giving the best fit between calculated and observed dielectric constant are $\chi_{f0}=0{\cdot}7\times 10^{-4}$, $T_{f0}=310°\text{C}$, $\alpha=1{\cdot}37$, $\beta=0{\cdot}265$ and the fit obtained is shown in fig. 4.

Fig. 4

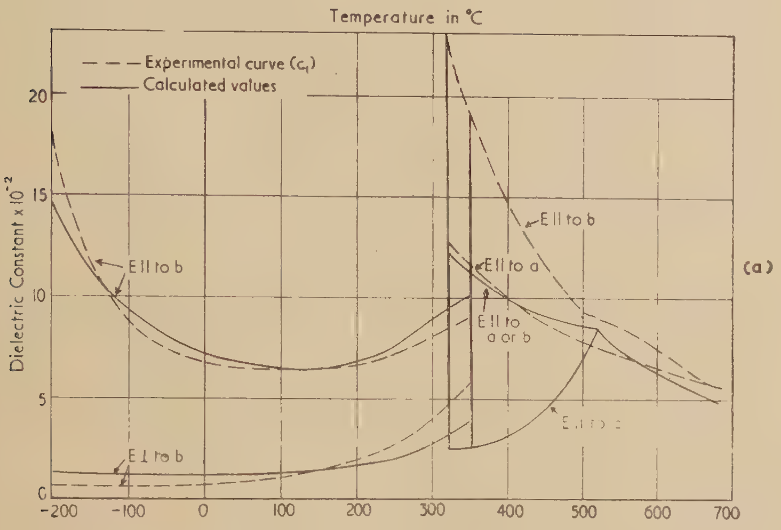

Dielectric constant of $NaNbO_3$ monocrystals.

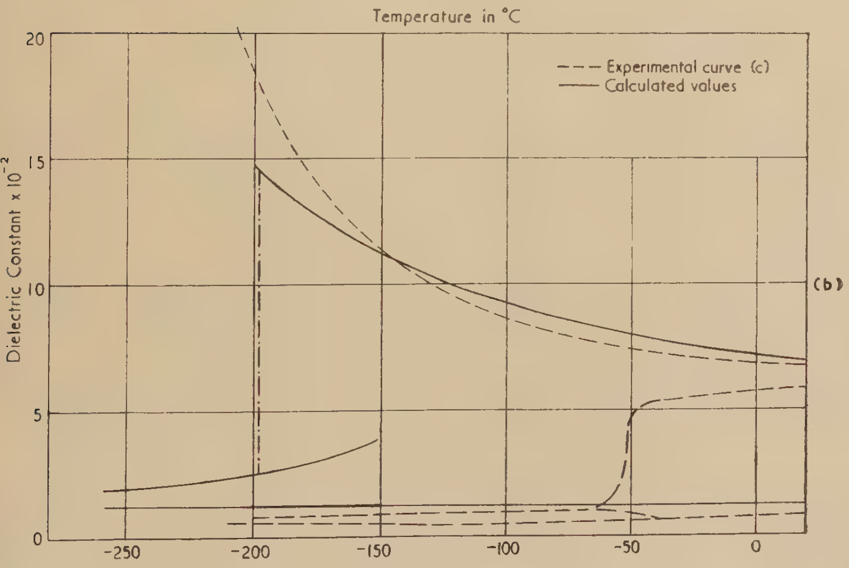

Dielectric constant at low temperature.

To determine the remaining ferroelectric constants, it is necessary to consider the low temperature ferrielectric state. Experimental data are meagre, but the sudden onset of hysteresis and the small change in extrapolated polarization with temperature (C_1) would suggest that at the ferroelectric curie temperature there would be a first order change. With this assumption we may make use of Devonshire's treatment (1949) to simplify the ferroelectric part of (2.7(j)). Substituting also from (3.3) for p_y this becomes

$$0=((T-T_f)/(T_1-T_f)+2\beta\Delta\mu_M/\chi_{f0}(T_1-T_f))-4z+3z^2 \quad . \quad (3.13)$$

where

T_1 is the ferroelectric transition temperature,

$\Delta\mu_M$ a measure of the optical anisotropy in the ferrielectric,

P_1 is the ferroelectric polarization at T_1,

$$z=\left(\frac{P_x}{P_1}\right)^2. \quad . \quad . \quad . \quad . \quad . \quad . \quad . \quad . \quad (3.14)$$

The ' antiferroelectric ' part of (2.7(j)) becomes

$$0=(T-T_a)+\beta wz/\{\chi_{f0}(T_1-T_f)\}+(A+B)\Delta\mu_M+(C+D)\Delta\mu_M^2+F\Delta\mu_M^3 \quad . \quad . \quad . \quad . \quad (3.15)$$

where $$w=\chi_{f0}(T_1-T_f)P_1^2/(K\chi_{a0}) \quad . \quad . \quad . \quad . \quad . \quad (3.16)$$

and the free energy in the ferrielectric state is given by

$$\Delta G=K\chi_{a0}\{(\tfrac{1}{2}z^3-z^2+\tfrac{1}{2}z(T-T_f)/(T_1-T_f))w+(T-T_a)\Delta\mu_M+\tfrac{1}{2}(A+B)\Delta\mu_M^2$$
$$+\tfrac{1}{3}(C+D)\Delta\mu_M^3+\tfrac{1}{4}F\Delta\mu_M^4+\beta\Delta\mu_M wz/(\chi_{f0}(T_1-T_f))\}. \quad . \quad . \quad . \quad (3.17)$$

At the transition temperature T_T, antiferroelectric and ferrielectric states must have similar free energy so that from (3.17) and (3.7)

$$(\tfrac{1}{2}z^3-z^2+\tfrac{1}{2}z(T_T-T_f)/(T_1-T_f))w+(T_T-T_a)\Delta\mu_M$$
$$+\tfrac{1}{2}(A+B)\Delta\mu_M^2+\tfrac{1}{3}(C+D)\Delta\mu_M^3+\tfrac{1}{4}F\Delta\mu_M^4+\beta\Delta\mu_M wz/\chi_{f0}(T_1-T_f)$$
$$=(T_T-T_a)\Delta\mu_1+\tfrac{1}{2}(A+B)\Delta\mu_1^2+\tfrac{1}{3}(C+D)\Delta\mu_1^3+\tfrac{1}{4}F\Delta\mu_1^4. \quad (3.18)$$

With the additional condition that no other ferrielectric or ferroelectric states have lower free energy than the antiferroelectric structures observed at higher temperature, a reasonable fit with the observed transition temperature is obtained with

$$w=3{\cdot}65, \qquad T_1=415°\text{c}.$$

The free energy in the ferrielectric phase, using these values is shown in fig. 3 (curve (c)). The alternative ferroelectric tetragonal phase (fig. 3, curve (d)) deduced using these values of w and T_1 has only slightly higher free energy than the antiferroelectric states at 335°c (fig. 3, curves (a), (b)).

3.4. *Dielectric Constant at Low Temperature*

For the ferrielectric solution (2.7(j)), the dielectric stiffness eqns. (2.8) become

$$\chi_{xx}=\chi_{yy}=\chi_{f0}(T-T_f)+(\lambda+\theta)p_y^2+\xi_{12}'P_x^2, \quad . \quad . \quad . \quad (3.19)$$

$$\chi_{zz}=\chi_{f0}(T-T_f)+3\xi_{11}'P_x^2+5\zeta'P_x^4+2\theta p_y^2. \quad . \quad . \quad (3.20)$$

Using eqn. (3.2) and Devonshire's simplification for the ferroelectric terms, (3.19) and (3.20) become

$$\chi_{xx}=\chi_{yy}=\chi_{f0}(T-T_f)+(\alpha+\beta)\Delta\mu_M+4\chi_{f0}(T_1-T_f)\alpha z, \quad . \quad . \quad . \qquad (3.21)$$

$$\chi_{zz}=\chi_{f0}(T_1-T_f)\{(T-T_f)/(T_1-T_f)-12z+15z^2\}+2\beta\Delta\mu_M. \qquad (3.22)$$

Substituting the values of z, $\Delta\mu_M$ and T calculated in § 3.3, χ_{xx}, χ_{yy}, χ_{zz} may be evaluated, and thus the corresponding dielectric constant values deduced. These are shown in fig. 4(*b*).

3.5. *Electrically Forced Transitions*

The experimental double hysteresis curves at room temperature (C_1) show that there is a sudden increase in the total polarization at a field ≃100 kv/cm, applied in a direction perpendicular to the orthorhombic *c*-axis.

From (2.2) there is a solution (2.7(*h*)), which is a spontaneously polarized ferrielectric state of only slightly higher free energy than the stable antiferroelectric orthorhombic state at zero field. At high field strength this may become the state of least energy.

For a field E_x applied axially along x, conditions for stability of (2.7(*h*)) become

$$E_x=P_x(\chi_f+\xi_{11}'P_x^2+\zeta'P_x^4+\theta p_y^2), \quad . \quad . \quad . \quad . \qquad (3.23)$$

$$0=\chi_a+\xi_{11}p_y^2+\zeta_{111}p_y^4+\eta p_y^6+\theta P_x^2. \quad . \quad . \quad . \qquad (3.24)$$

Using (3.3) and Devonshire's simplification for the ferroelectric terms, (3.23) and (3.24) may be rewritten

$$E_x/\{\chi_{f0}P_1(T_1-T_f)\}=z^{1/2}\{(T-T_f)/(T_1-T_f)+\beta\Delta\mu/\chi_{f0}(T_1-T_f)-4z+3z^2\}$$
$$. \quad . \quad . \quad . \qquad (3.25)$$

$$0=(T-Ta)+\beta wz/(\chi_{f0}(T_1-T_f))+A\Delta\mu+C\Delta\mu^2+F\Delta\mu^3 \qquad (3.26)$$

and from (2.2) the free energy is given by

$$\Delta G=\{\tfrac{1}{2}z^3-z^2+\tfrac{1}{2}z(T-T_f)/(T_1-T_f)\}w+\tfrac{1}{2}(T-Ta)\Delta\mu+\tfrac{1}{4}A\Delta\mu^2$$
$$+\tfrac{1}{6}C\Delta\mu^3+\tfrac{1}{8}F\Delta\mu^4+\tfrac{1}{2}\beta\Delta\mu wz/(\chi_{f0}(T_1-T_f))+E_xz^{1/2}w/P_1\chi_{f0}(T_1-T_f).$$
$$. \quad . \quad . \quad . \qquad (3.27)$$

The dielectric constant in the antiferroelectric state is low for this field orientation, so that for an approximate solution we may neglect the energy contribution from the field in the antiferroelectric state, and write

$$0=(T-Ta)+(A+B)\Delta\mu_1+(C+D)\Delta\mu_1^2+F\Delta\mu_1^3, \quad . \quad . \qquad (3.28)$$

$$\Delta G=(T-Ta)\Delta\mu_1+\tfrac{1}{2}(A+B)\Delta\mu_1^2+\tfrac{1}{3}(C+D)\Delta\mu_1^3+\tfrac{1}{4}F\Delta\mu_1^4. \qquad (3.29)$$

At the forced transition

$$\{\tfrac{1}{2}z^3-z^2+\tfrac{1}{2}z(T-T_f)/(T_1-T_f)\}w+\tfrac{1}{2}(T-T_a)\Delta\mu_1+\tfrac{1}{4}A\Delta\mu^2+\tfrac{1}{6}C\Delta\mu^3+\tfrac{1}{8}F\Delta\mu^4$$
$$+\tfrac{1}{2}\beta\Delta\mu wz/(\chi_{f0}(T_1-T_f))+E_xz^{1/2}w/\chi_{f0}P_1(T_1-T_f)=(T-T_a)\Delta\mu_1$$
$$+\tfrac{1}{2}(A+B)\Delta\mu_1^2+\tfrac{1}{3}(C+D)\Delta\mu_1^3+\tfrac{1}{4}F\Delta\mu_1^4. \quad . \quad . \quad . \quad . \quad . \qquad (3.30$$

Eliminating E_x and z, (3.30) may be solved numerically for $\Delta\mu$ at any fixed temperature, and substituting back in (3.25) and (3.26) z and E/P_1 evaluated.

Using $P_1=10\,\mu c/cm^2$ the calculated temperature variation of the field required to force the transition is shown in fig. 5.

Fig. 5

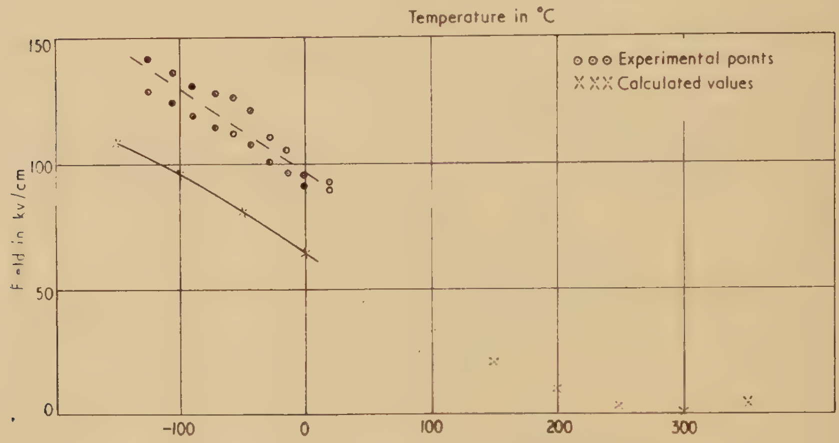

Field required to generate double hysteresis in $NaNbO_3$.

§ 4. THE PROPERTIES OF MIXED (KNa)NbO_3 CRYSTALS

$KNbO_3$ has been shown to have properties closely analogous to those of $BaTiO_3$ (S_2). There are first order structure changes at 425°c, 225°c and −10°c, and the observed symmetries suggest that the stable states correspond to solutions (2.7(*a*), (*b*), (*c*), (*d*)) of (2.2).

The properties appear to be adequately described by a simple Devonshire expression with values of the constants

$$T_1=430°\text{c}, \quad T_f=320°\text{c}, \quad \chi_{f0}=2{\cdot}62\times10^{-5}, \quad \alpha=0{\cdot}365.$$

In $NaNbO_3$, T_1 and T_f have similar values, respectively, to those for $KNbO_3$. Assuming that α is also similar for the two materials, the free energy in the unstable* orthorhombic and rhombohedral states may be calculated (fig. 3, curves (*e*), (*f*)).

It has been shown (S_1) that in mixed (NaK)NbO_3 crystals the antiferroelectric 'curie' temperature is linearly depressed with increasing $KNbO_3$. If in the free energy expression (2.2) only T_a changes, the free energy of mixed crystals may be directly deduced from fig. 3 by moving the antiferroelectric curve to lower temperature without changing its shape.

---

* The ferroelectric states are described as unstable in pure $NaNbO_3$ as though the solutions (2.7 (*b*), (*c*), (*d*)) correspond to minima in the free energy, they are not at any temperature the least minimum.

Using the experimentally determined value for the rate of change of curie temperature with concentration, i.e.

$$T_a = 10°\text{c}/1\% \text{ added K in (NaK)NbO}_3,$$

the free energy for a number of concentrations of $KNbO_3$ is shown in fig. 6. From these and other similar curves, the phase diagram for the

Fig. 6

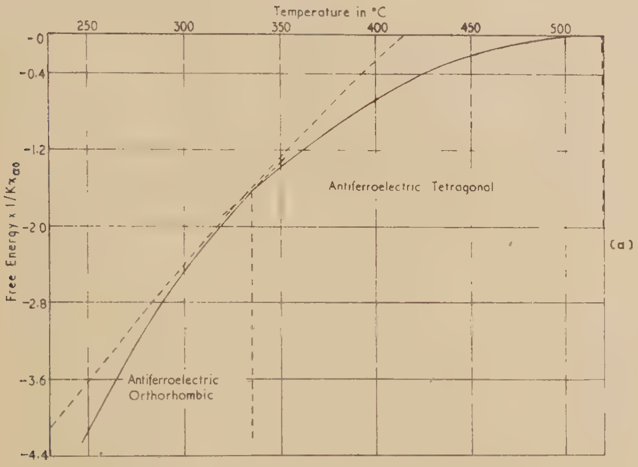

(a) Composition $NaNbO_3$.

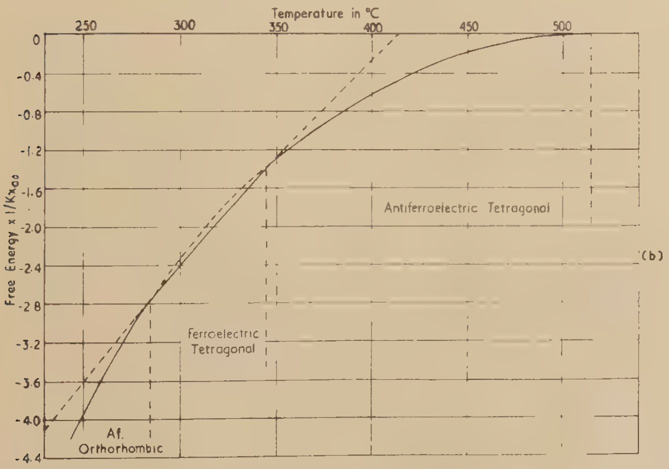

(b) Composition $(Na_{99\cdot5}K_{0\cdot5})NbO_3$.

Free energy as a function of temperature in $(NaK)NbO_3$.

system $NaNbO_3$ to $(Na_{0\cdot9}K_{0\cdot1})NbO_3$ has been deduced (fig. 7). The behaviour of the antiferroelectric to ferrielectric phase transition is not easily determined graphically, and the values shown in fig. 7 have been calculated from (3.13), (3.14), (3.15), (3.16) with suitable values of T_a.

§ 5. DISCUSSION

5.1. *Comparison with Experimental Values*

Over the orthorhombic temperature range (−200°c to +350°c) there is reasonable agreement between the observed and calculated anisotropy values, and as has already been indicated, the ' best fit ' between (3.5) and the experimental curve gives T_a close to one of the observed transitions. To obtain this agreement, it is necessary to include the term in $\Delta\mu^3$ in (3.5) and thus to include terms up to p^8 in the free energy expression. It should be noted also, that though the constant ζ_{123} cannot be evaluated from the available data, $K^2\zeta_{123}/\chi_{a0}$ must be greater than $2{\cdot}035\times10^5$ to avoid the occurrence of a rhombohedral antiferroelectric phase above −200°c.

Fig. 6

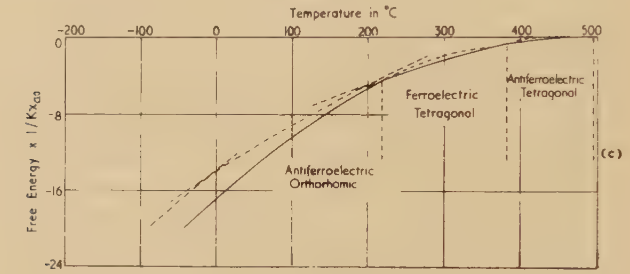

(c) Composition $(Na_{97{\cdot}5}K_{2{\cdot}5})NbO_3$.

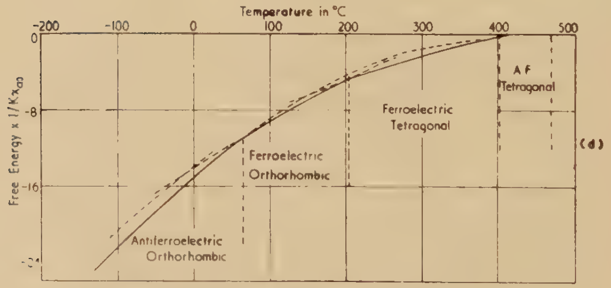

(d) Composition $(Na_{95}K_5)NbO_3$.

Free energy as a function of temperature in $(NaK)NbO_3$.

To obtain agreement with the optical anisotropy in the ' tetragonal ' region, it is necessary to assume different values of K, the constant in (3.3), in orthorhombic and tetragonal regions. From (3.3) however, there should also be a linear relation between p^2 and the elastic anisotropy, and consideration of the electrostrictive constants suggests that the constant ρ in (3.5) should be the same in both phases. Plotting $c/a-1$ against T (S_1) in figs. 1, 2 does show increased anisotropy in the tetragonal region, but the agreement is still poor.

The free energy expression (2.2) assumes that in the unpolarized unstressed condition $NaNbO_3$ has cubic symmetry. Optical measurements (C_1) however show that above 520°c the symmetry is not cubic, and below 520°c the dielectric constant values are not consistent with tetragonal symmetry. Clearly (2.2) is only an approximation to the true free energy expression which must have lower symmetry, but in view of the complexity of the expression no attempt will be made here to improve the agreement.

Fig. 7

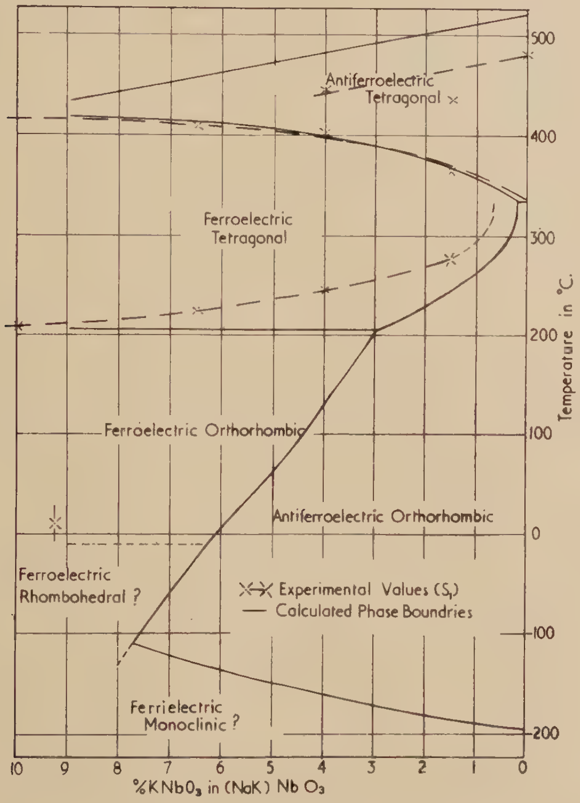

Phase diagram for mixed $(NaK)NbO_3$.

In the thermodynamic treatment it has been assumed that the low temperature polar phase is ferrielectric. The general agreement with observed properties would suggest that this assumption is essentially correct. A critical test could, however, be applied, as in the low temperature form, x-ray examination should reveal the super-lattice associated with the antiferroelectric polarizations.

A striking feature of the mixed $(NaK)NbO_3$ crystals is the rapidity with which the properties change from those of pure $NaNbO_3$ with increasing $KNbO_3$ concentration, so that in solid solutions with less than 90% $NaNbO_3$ the properties are very similar to those of pure $KNbO_3$.

In the foregoing analysis this rapid change arises through the presence of latent ferroelectric forms in pure $NaNbO_3$, similar to the stable phases of $KNbO_3$ but of slightly higher free energy than the antiferroelectric. The general features of the phase diagram for mixed crystals are well reproduced from the $NaNbO_3$ free energy expression changing only the parameters T_a and χ_{f0}.

Below room temperature, the data for mixed crystals are not yet complete, but there is no evidence for the rhombohedral ferroelectric phase which appears in the analysis for $KNbO_3$ concentrations greater than 6%. The treatment however also predicts that the ferrielectric–antiferroelectric phase transition temperature should rise with increasing $KNbO_3$ concentration in the mixed crystals. It is possible that the chosen values of w and T_1 put this phase change in pure $NaNbO_3$ at too low a temperature (the exact transition temperature is difficult to confirm experimentally because of a wide thermal hysteresis) and that values could be chosen which would make the ferrielectric more stable than the rhombohedral ferroelectric phase for intermediate compositions. Further experimental evidence is necessary to decide between these alternatives.

5.2. *Correlation with Crystal Structure*

The phenomenological method gives no direct information as to the origin of the observed properties, and the necessary complementary statistical mechanical treatment will not be attempted here. Certain features of the results with the mixed crystals do however suggest a correlation with the spatial relations in the structure.

In pure $KNbO_3$, the radii of the ions are such that the Goldschmidt tolerance factor t (Goldschmidt 1927) for the perovskite structure is very close to 1, i.e. the K ion is only slightly too small to fulfil the requirements for close packing. The structure may thus be regarded as a regular array of corner linked NbO_6 octahedra with the K ions almost filling the interstices. Substituting the smaller Na ion in some of the K sites in the $(NaK)NbO_3$ solid solutions will clearly have little effect on the already close-packed octahedra. The very small change in the ferroelectric properties with increasing $NaNbO_3$ would thus suggest that in the solid solutions the ferroelectric phenomena are essentially determined within the NbO_6 array.

At high $NaNbO_3$ concentrations, the regular NbO_6 array may become unstable, 'crumpling' to reduce the excessive space available to the Na ions. A possible explanation of the high temperature structure changes in $NaNbO_3$ may then be given as follows :

(*a*) At 638°C the regular NbO_6 array 'crumples' to reduce the excessive space about the Na ions. The symmetry is reduced to tetragonal with $c/a<1$.

(*b*) At 520°C ordered displacements occur in the new NbO_6 array, alternate sheets of Nb ions perpendicular to the tetrad axis being displaced in opposite sense.

(*c*) At 470°C the character of the ordering changes by a doubling of the repeat interval, i.e. the Nb ions in successive sheets perpendicular to *c* have polarizations ++ −− ++ etc.

With this sequence of changes, the displacements of ions occurring in the room temperature phase (Vousden 1951) may be accomplished at 320°C without a major reconstruction of the existing system.

5.3. *Properties of the Alkali Tantalates*

Some support for the dependence on spatial relationships proposed in § 5.2 may be obtained from a comparison of the properties of the niobates with the corresponding tantalates $NaTaO_3$ and $KTaO_3$. Tantalum and niobium have very similar ionic sizes, so that properties which are essentially ‘ space dependent ’ should be common to the two structures.

That the onset of ferroelectricity is not primarily determined by the space available to the B ion in these ABO_3 compounds is clearly demonstrated by the potassium salts. In $KNbO_3$ the curie temperature is at 425°C, whilst in $KTaO_3$ in spite of a slightly smaller Ta ion, spontaneous polarization does not occur above 14°K (Hulm and Matthias 1950).

In sodium niobate, it is suggested in § 5.2 that the collapse of the structure about the Na ions which initiates the antiferroelectricity is primarily due to spatial considerations. We have recently investigated optically the properties of single crystals of $NaTaO_3$ at high temperature (Cross 1955) and do find a similar transition from cubic to tetragonal symmetry at 630°C. There are also further phase changes to an orthorhombic (pseudo-tetragonal) state at 580°C, and the room temperature orthorhombic (rotated axis) form at 480°C. (This latter transition would appear to be the change previously reported as the curie temperature (Matthias 1949).) There is no evidence of any change corresponding to that occurring at 470°C in $NaNbO_3$ and it is interesting to note that a recent determination of the $NaTaO_3$ structure at room temperature (Kay Miles 1954) shows a doubling of the b spacing of the primitive unit cell, as compared with the quadrupling observed in $NaNbO_3$.

Unfortunately there are no data regarding the dielectric constant in $NaTaO_3$ and no information appears yet to have been published on mixed $(KNa)TaO_3$ solid solutions.

List of Symbols

ΔG	The Helmholtz free energy of a free crystal per unit volume. (Taking the energy zero to be that of the unstressed unpolarized crystal.)
P_a, P_b	The sub-lattice polarizations.
P	The total polarization (P_a+P_b).
p	A measure of the antiferroelectric polarizations (P_a-P_b).
P_x, P_y, P_z p_x, p_y, p_z	The components of total polarization and antiferroelectric polarizations in the axial directions.
χ_f, ξ_{11}' ξ_{12}', ζ'	The coefficients of the ferroelectric terms in the free energy expression.

$\chi_a, \xi_{11}, \xi_{12}, \zeta_{111}$ $\zeta_{112}, \zeta_{123}, \eta$	The coefficients of the antiferroelectric terms in the free energy expression.
λ, θ	The coefficients of the ferroelectric, antiferroelectric cross terms in the free energy expression.
χ_{f0}	The temperature invariant factor in χ_f.
χ_{a0}	The temperature invariant factor in χ_a.
T_f	The ferroelectric extrapolated curie temperature.
T_a	The antiferroelectric curie temperature.
χ	The dielectric stiffness, i.e. the reciprocal elastic susceptibility.
$\chi_{xx}, \chi_{yy}, \chi_{zz}$	The axial components of the dielectric stiffness.
$\Delta\mu$	The birefringence of tetragonal $NaNbO_3$.
$\Delta\mu_1$	The birefringence β–α of orthorhombic $NaNbO_3$.
$\Delta\mu_M$	A measure of the optical anisotropy in the low temperature form of $NaNbO_3$.
ρ	The constant of proportionality between elastic anisotropy $(c/a-1)$ and the square of the antiferroelectric polarization.
K	The constant of proportionality between the optical anisotropy and the square of the antiferroelectric polarization.
T_1	The temperature at which the unstable ferroelectric and paraelectric states have the same free energy.
P_1	The spontaneous polarization in the ferroelectric state at T_1.

Acknowledgments

The author wishes to express his sincere thanks to Professor E. C. Stoner, under whose direction this work was initiated, and to Dr. B. J. Nicholson for his assistance in the early formulation of the treatment. He is also indebted to the British Electrical and Allied Industries Research Association for the facilities to complete the work, and to the Director for permission to publish this paper.

References

Cross, L. E., 1955, Unpublished.
Cross, L. E., and Nicholson, B. J., 1955, *Phil. Mag.*, **46,** 212.
Devonshire, A. F., 1949, *Phil. Mag.*, **40,** 1040 ; 1954, *Advances in Physics*, **3,** 85.
Goldschmidt, V., 1927, *Geo. Chem. Vest. Elem.*, VII, VIII.
Hulm, J. K., and Matthias, B., 1950, *Phys. Rev.*, **79,** 885.
Kay, H. F., and Miles, J. L., 1954, Private communication from the Authors.
Kittel, C., 1951, *Phys. Rev.*, **82,** 729.
Matthias, B. J., 1949, *Phys. Rev.*, **75,** 1771.
Shirane, G., Sawaguchi, E., and Takeda, A., 1951, *Phys. Rev.*, **84,** 476.
Shirane, G., Danner, H., Pavlovic, A., and Pepinsky, R., 1954, *Phys. Rev.*, **93,** 672.
Shirane, G., Newnham, R., and Pepinsky, R., 1954, *Phys. Rev.*, **96,** 581.
Vousden, P., 1951, *Acta Cryst.*, **4,** 545.

VIII. *An Unusual Double V-Event at Sea Level*

By J. L. Lloyd and A. W. Wolfendale
The Physical Laboratories, The University, Manchester*

[Received September 27, 1955]

A multiplate cloud chamber has been operated at sea level under the Manchester Spectrograph in an experiment designed primarily to study the scattering of μ-mesons (Lloyd and Wolfendale 1955 a) and among the photographs taken is the one reproduced in Plate 1 and the figure. The spectrograph gives no information on the momentum of the particle responsible for the interaction since the primary particle is part of a shower.

The event has been reprojected, through the actual lenses used, together with other photographs taken before and after in order to find the extent of the illuminated region, condensation and illumination conditions and noise-level scattering. The photograph probably indicates an interaction by the particle marked (1) in one of the 1 cm lead plates, in which is produced a number of charged particles, (2)–(5), together with two neutral particles emitted in opposite directions and decaying into particles a_1 and a_2, b_1 and b_2 respectively. The knock-on electron produced by (1) in the top plate shows that this particle is very probably moving downwards.

The primary particle has the ionization of a fast singly-charged particle (I_{plat}) and an r.m.s. projected angle of scattering of 0·4° per plate ; tracks in this region have an r.m.s. noise-level scattering of 0·2°. Assuming particle (1) to be a proton the estimated momentum is $2{\cdot}1^{+2\cdot3}_{-0\cdot5}$ GeV/c (Lloyd and Wolfendale 1955 b). The most probable value is quoted and the errors are the limits for a 68·27% probability of the true value lying between them. If (1) is a π-meson the momentum will be approximately the same. The data of Camerini *et al.* (1952) on star production indicate a momentum of about 4 GeV/c, in rough agreement.

Particles (2), (3) and (5) pass out of the illuminated region with ionizations less than $3\times I_{\text{plat}}$. Particle (4) has ionization $(1{\cdot}5\text{–}4)\times I_{\text{plat}}$. From the scattering in two plates the value of $p\beta$ for particle (5) is found to be $p\beta=140^{+84}_{-48}$ MeV/c. From considerations of range particle (5) is probably a π-meson although a μ-meson is not excluded.

The origin of the interaction is well defined by tracks (1), (2), (3) and (5).

Two neutral V-particles, designated a and b are associated with the interaction. Particle a decays into two charged secondaries a_1 and a_2, 8·4 cm from the origin of the interaction. The spatial angles ϕ_1 and ϕ_2 between the trajectories of a and a_1, a and a_2, together with the estimated ionizations are given in table 1. Evidence that the decay event is directly associated with the interaction is provided by the fact that the lack of coplanarity (the angle δ between the plane of the secondaries and the origin of the interaction) is small, δ being $1\cdot5\pm2°$. Particle a_1 penetrates two plates before reaching the edge of the illuminated region. Scattering measurements indicate that the momentum is given by

---

* Communicated by the Authors.

$$p\beta=800^{+480}_{-270}\ \text{Mev}/c.$$

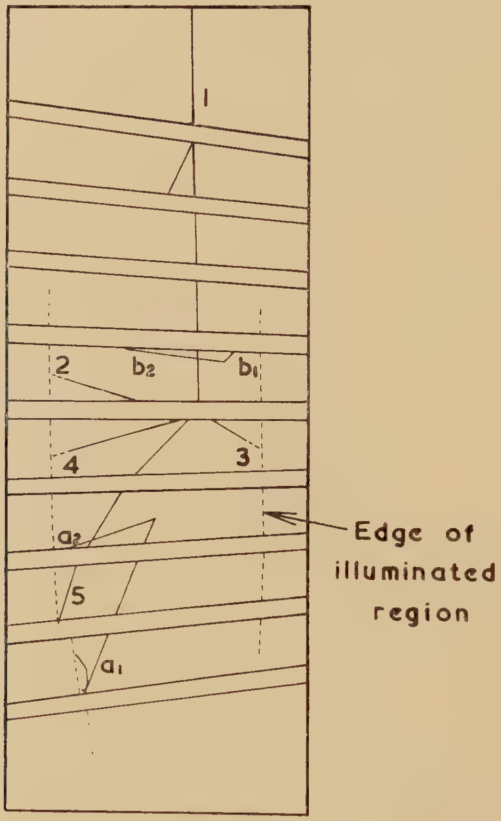

Side View

Particle a_2 travels obliquely towards the rear and the track would not be seen to emerge even if the particle had penetrated the plate.

The upper *V*-event consists of two decay products b_1 and b_2, the lack of coplanarity again being small: $\delta=1\pm6°$. The track of particle b_1 would be visible above the plate if the particle had penetrated (unless it had suffered a large deflection towards the front of the chamber), so b_1 has a range less than 1·7 cm Pb.

The *V*-events have been analysed (following Podolanski and Armenteros 1954) on the assumption that they represent the dacays of θ^0- or

Table 1. V^0-Event *a*

Secondary particle	Visual estimate of relative ionization I/I_{plat}	ϕ (deg)	Primary assumed to be			
			$\theta^0(\pi, \pi)$ 1020^{-20}_{-22} Mev/c		$\Lambda^0(P, \pi)$ 1003^{-127}_{+102} Mev/c	
			Momentum in Mev/c (calc.)	I/I_{plat} (calc.)	Momentum in Mev/c (calc.)	I/I_{plat} (calc.)
a_1	2 Ratio $<1{\cdot}5$	$5{\cdot}2 \pm 1{\cdot}6$	936^{-41}_{+3}	$1{\cdot}0$ Ratio $1{\cdot}7^{-0{\cdot}3}_{+0{\cdot}8}$	(P) 922^{-136}_{+121}	$1{\cdot}5^{+0{\cdot}2}_{-0{\cdot}2}$ Ratio $1{\cdot}15^{-0{\cdot}3}_{+0{\cdot}6}$
a_2	2	$44{\cdot}5 \pm 2{\cdot}0$	121^{+30}_{-37}	$1{\cdot}7^{-0{\cdot}3}_{+0{\cdot}8}$	(π) 119^{+13}_{-26}	$1{\cdot}7^{-0{\cdot}2}_{+0{\cdot}5}$

The ratio of observed path length to mean decay length is about unity for each decay scheme.

Table 2. V^0-Event *b*

Secondary particle	Visual estimate of relative ionization I/I_{plat}	ϕ (deg)	Primary assumed to be $\Lambda^0 177^{+69}_{-46}$ Mev/c	
			Momentum in Mev/c (calc.)	I/I_{plat} (calc.)
b_1	4–9	28 ± 8	(P) 200^{+64}_{-40}	$11{\cdot}5^{-4}_{+4{\cdot}5}$
b_2	2·5–5	$90{\cdot}5 \pm 2{\cdot}5$	(π) 94^{-4}_{+2}	$2{\cdot}3^{+0{\cdot}1}_{-0{\cdot}1}$

The ratio of observed path length to mean decay length is $2{\cdot}4^{+0{\cdot}9}_{-0{\cdot}7}$.

Λ^0-particles and the results are given in tables 1 and 2. The errors quoted are standard deviations, the asymmetry occurs because the momentum of the primary passes through a maximum as ϕ_1 is varied.

It can be seen that the evidence of table 1 is consistent with particle a being a θ^0- or a Λ^0-particle.

If particle b were a θ^0-particle, the ionizations of its secondaries would be near to I_{plat}, in disagreement with the observed ionizations. Furthermore the secondary b_1 would be visible above the plate. It is concluded that particle b is a Λ^0-particle, with which view all the data are consistent.

The angle between the planes of the V^0-events is $43 \pm 8^\circ$.

As mentioned earlier the two V-particles are emitted from the interaction in almost opposite directions, the lack of collinearity being $2{\cdot}5 \pm 2{\cdot}5^\circ$.

The interpretation of the photograph is not entirely clear. The collinearity of the V^0 trajectories strongly suggests the two-body decay of a particle at rest. However, the momentum of the centre of mass in the $\theta^0 + \Lambda^0$ scheme would be 843 ± 60 Mev/c, and in the $\Lambda^0 + \Lambda^0$ scheme 826 ± 130 Mev/c, both values obviously being inconsistent with zero.

It is possible that the photograph shows a reaction of the type

$$\pi^- + P \rightarrow \theta^0 + \Lambda^0.$$

If the momentum of the θ^0-particle exceeds 1 Gev/c at production (the estimated momentum of particle a is $\sim$ 1020 Mev/c if a θ^0-particle) then the greatest possible angle between the V-particles is 80° (James and Salmeron 1955). This would indicate scattering of one or both of the V-particles; the low momentum, 177^{+69}_{-46} Mev/c, of particle b is typical of Λ^0-particles and may result from a loss of energy by scattering. James and Salmeron estimate that only 2% of pairs of V^0-particles emerge from a heavy nucleus without either suffering scattering. Thus double production with subsequent scattering seems probable, but the collinearity must then be fortuitous.

ACKNOWLEDGMENTS

The authors wish to thank Professor G. D. Rochester and Mr. G. D. James for many helpful discussions.

REFERENCES

CAMERINI, V., LOCK, W. O., and PERKINS, D. H., 1952, *Progress in Cosmic Ray Physics*, I (Amsterdam: North-Holland Publishing Co.).

JAMES, G. D., and SALMERON, R. A., 1955, *Phil. Mag.*, **46**, 571.

LLOYD, J. L., and WOLFENDALE, A. W., 1955 a, *Proc. Phys. Soc.* A, **68**, 1045; 1955 b, *Cloud Chamber Conference* (London: Physical Society), in the press.

PODOLANSKI, J., and ARMENTEROS, R., 1954, *Phil. Mag.*, **45**, 13.

IX. CORRESPONDENCE

Proportional Counter Measurements of π-Mesonic X-Rays from Beryllium

By D. West and E. F. Bradley
Atomic Energy Research Establishment, Harwell

[Received October 14, 1955]

Up to now π-mesonic x-rays have been studied exclusively with scintillation counters (Camac *et al.* 1952, 1955, Stearns *et al.* 1954). An improvement in energy resolution, amounting to nearly a factor of six, can be attained by using proportional counters instead. An aluminium counter (diameter 5·3 cm, wall thickness 0·030 in.) was fitted with field tubes providing a well-defined region, 10 cm long, over which the multiplication factor was constant. It was filled with xenon at 2 atm pressure, plus methane at a pressure of 3 cm of mercury. The negative meson beam from the Liverpool synchrocyclotron entered the apparatus shown in fig. 1. The thickness of the absorber *A* is adjusted to give a maximum number of π^--mesons stopped in the target material X. Scintillation counters 1, 2 and 3 were used to select mesons stopping in X by means of a 1, 2-coincidence in anticoincidence with 3. The 1, 2–3 pulse was put in coincidence with the proportional counter output (resolving time 2 μsec); and this coincidence pulse was used to trigger a gating unit which opened for 10 μsec and allowed the proportional counter pulse to pass to a multichannel kicksorter. The anticoincidence scintillator 3 completely covered the active region of the proportional counter and was viewed by two photomultipliers. The beam intensity was adjusted to give a negligible casual

Fig. 1

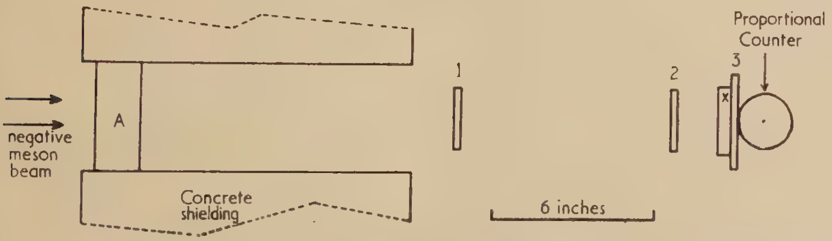

Experimental Arrangement. A, Slowing material $1\frac{5}{8}$ in. Cu; X, . . Mesonic x-ray source element; 1, 2, Plastic scintillators 2·3 in. × 2·5 in. × 0·25 in.; 3 Plastic scintillator (anticoincidence) 4 in. × 3·5 in. × 0·25 in.

rate. The mean rate in the proportional counter was about 1600 c.p.m. (160 000 c.p.m. during the pulse) and about 400 π^--mesons/minute stopped in the target. The gating rate was about 15 c.p.m. The counter was calibrated with K x-rays from ^{153}Gd (weighted average energy of K_α peak$=41{\cdot}3_1$ kev) at intervals of two hours during the runs.

Two runs, each of ten hours' total duration were carried out with metallic beryllium samples, 2·97 g/cm² in thickness (3 in. × $2\frac{3}{4}$ in.) and 2·3 g/cm² in thickness ($2\frac{1}{2}$ in. × $2\frac{1}{2}$ in.) respectively. The spectrum obtained with the thicker sample is shown in fig. 2. Peaks due to the mesonic $K_\alpha(2p \rightarrow 1s)$ radiation with its associated 'escape' peaks $K_\alpha - K_{\alpha\,\text{xenon}}$, $K_\alpha - K_{\beta\,\text{xenon}}$* are clearly seen, together with smaller peaks $K_\beta(3p \rightarrow 1s)$ and its 'escape' peak $K_\beta - K_{\alpha\,\text{xenon}}$. Counts in adjacent channels were added to give the above spectrum. In determining the energy of the K_α peak, curves were drawn by two independent observers using plots in which adjacent channels were added in pairs in the two possible ways, so that four values of the energy were obtained. A correction due to slight non-uniformity of multiplication factor along the counter is necessary since the calibration

Fig. 2

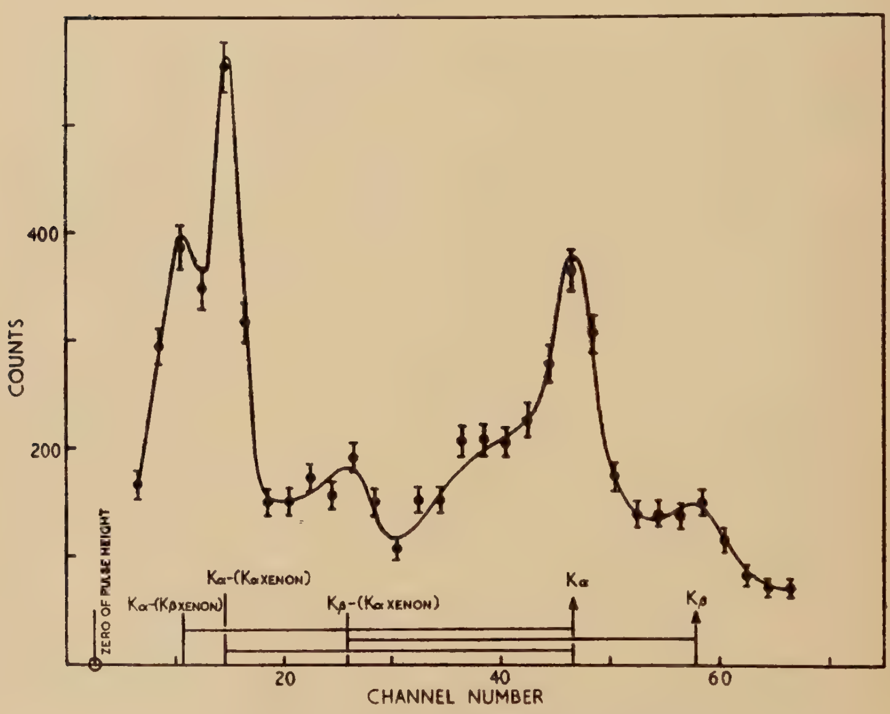

π mesonic K x-rays from Beryllium (2·97 gm/cm²).

---

* $K_{\alpha\,\text{xenon}}$ (electronic)$=29{\cdot}66$ kev, $K_{\beta\,\text{xenon}}$ (electronic)$=33{\cdot}62$ kev.

x-rays entered the counter mid-way along it, whereas the mesonic x-ray source covered most of the counter. The correction was determined by measuring the pulse heights from a calibration source placed at a large number of points over the area covered by the beryllium. It amounted to a change of $+0{\cdot}3\%$. Possible shifts associated with the high counting rate during the cyclotron pulse were checked with a strong source placed behind a rotating shutter. The shift was less than $0{\cdot}1\%$ at the rate used during the cyclotron runs. The value for the K_α energy obtained with the thicker source was $41{\cdot}69$ kev and with the thinner source $41{\cdot}8_4$ kev, giving a mean value of $41{\cdot}7_6$ kev. The probable error is estimated at $\pm 0{\cdot}20$ kev. Previous determinations gave values of $43 \pm 3{\cdot}5$ kev (Camac *et al.* 1955), $42{\cdot}9 \pm 0{\cdot}5$ kev and $42{\cdot}00 < E < 43{\cdot}57$ kev (Stearns *et al.* 1955). The calculated value of the energy in the absence of nuclear force effects is $43{\cdot}9$ kev (Stearns *et al.* 1955), so that a nuclear force shift is definitely confirmed for beryllium.

Fig. 3

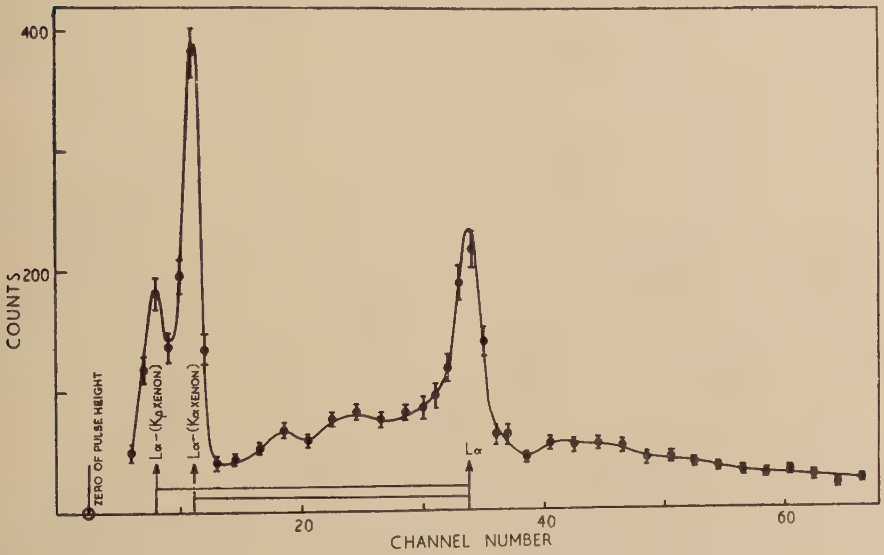

π mesonic L x-rays of Fluorine. Source Li F $1{\cdot}74$ g/cm^2.

The intensity of the K_β peak, which may contain contributions from higher transitions, is approximately $0{\cdot}4$ times that of the K_α peak when the relative efficiency of the counter for the two radiations is taken into account.

The widths of the K_α and its escape peak were determined by fitting gaussians to the spectra obtained by plotting the single channel counts. Values of the observed standard deviation $\sigma_{\text{obs}} = 1{\cdot}9$ and $2{\cdot}2$ kev were obtained for the K_α peak in the two runs and $\sigma_{\text{obs}} = 1{\cdot}3$ and $1{\cdot}1$ kev for the escape peak. The instrumental widths determined from measurements with a small source placed mid-way along the counter are $\sigma_{\text{ins}}=1{\cdot}3$ kev and $\sigma_{\text{ins}}=0{\cdot}83$ kev for these two energies. However a more direct measurement of the instrumental widths using the whole sensitive region of the counter is required. For this purpose the π-mesonic L rays of fluorine were studied. Energy shifts and line broadening due to nuclear interactions are expected to be small in this case. A run of six hours' duration was carried out with a source of lithium fluoride $1{\cdot}74$ g/cm^2 in thickness. The spectrum shown in fig. 3 was obtained. It clearly shows peaks due to the $L_\alpha(3\rightarrow2)$ transition and its associated escape peaks $(L_\alpha\text{–}K_{\alpha\,\text{xenon}})$ and $(L_\alpha\text{–}K_{\beta\,\text{xenon}})$. The energy was determined as $41{\cdot}25$ kev to be compared with the calculated value of $41{\cdot}5$ kev (Stearns *et al.* 1955), neglecting nuclear shifts but including vacuum polarization and finite nuclear size effects. The observed widths of the L_α peak and its escape peak are $\sigma_{\text{obs}}=1{\cdot}7$ kev and $\sigma_{\text{obs}}=0{\cdot}8_4$ kev respectively, and these widths are presumed to be purely instrumental in origin. Since the energy is closely similar to that of the beryllium K radiation the fluorine spectrum provides good values of the relevant instrumental widths. The K_α peak of beryllium is therefore naturally broadened by an amount

$$\Gamma=\surd({\sigma_{\text{obs}}}^2-{\sigma_{\text{ins}}}^2)=\surd(2{\cdot}05^2-1{\cdot}7^2)=1{\cdot}3 \text{ kev}$$

whereas its escape peak is naturally broadened by an amount

$$\Gamma=(1{\cdot}2^2-0{\cdot}8_4{}^2)=0{\cdot}7_4 \text{ kev}.$$

Any natural broadening of the K_α line would of course show up equally in the main and escape peaks.

A theoretical expression for the natural broadening due to capture from the 1s state has been given by Brueckner (1955). In the case of beryllium a value of $\Gamma=0{\cdot}9$ kev is predicted. The indications of a broadening in the present measurements are consistent with this value.

ACKNOWLEDGMENTS

We are very grateful to Professor Skinner for allowing us to use the strong focused pion beam of the synchrocyclotron and the facilities of his laboratory and to Dr. J. M. Cassels and Mr. A. Merrison and other members of the laboratory for their advice, and to Mr. B. S. Halliday and the cyclotron crew. Dr. F. C. Barker (A.E.R.E.). elucidated several points in connection with the theoretical expression for the width.

REFERENCES

BRUECKNER, K. A., 1955, *Phys. Rev.*, **98,** 769.

CAMAC, M., MCGUIRE, A. D., PLATT, J. B., and SCHULTE, H. J., 1952, *Phys. Rev.*, **88,** 134; 1955, *Ibid.*, **99,** 897.

STEARNS, M., STEARNS, M. B., DEBENEDETTI, S., and LEIPUNER, L., 1954, *Phys. Rev.*, **93,** 1123; 1955, *Ibid.*, **97,** 240.

Polygonization in Copper

By A. Franks and D. McLean
Communication from the National Physical Laboratory

[Received September 29, 1955]

Recent experiments in this Laboratory have shown that copper tends to polygonize during creep. This is evident from back-reflection x-ray diffraction patterns taken with a microbeam camera (beam diameter approximately $60\,\mu$, specimen to film distance 14 mm).

Figures 1, 2 and 3 (figs. 1–4, Plate 2) show the progressive development of polygonization in a copper specimen. The ill-defined spots in fig. 3 indicate that the process of polygonization was not completed. Sub-crystal formation could not proceed beyond the stage shown in the figure because further strain of the specimen resulted in fracture owing to the brittleness of copper at high temperatures.

Polygonization is associated with the climb of dislocations and therefore the rate of polygonization depends on the number of jogs and vacancies (Mott 1951). The rates of polygonization in aluminium and copper were compared by taking microbeam photographs of a number of specimens which had been subjected to various rates of strain and extensions. The experiments were carried out at temperatures proportional to the ratio of the absolute melting points of aluminium and copper respectively, in a rough attempt to make the thermal mobilities in both metals equal.

Figures 3 and 4 illustrate the differing rates of polygonization. The aluminium specimen (fig. 4) was stretched faster than the copper specimen (fig. 3) to approximately the same extension, but produces sharper spots. Though the experiments were not carried out at identical rates of strain and extension, the general conclusion after examining all the photographs is that aluminium polygonizes faster than copper.

The difference in the rates of polygonization is however not nearly as great as the difference in the number of jogs present in thermal equilibrium, as deduced from the jog energies calculated by Seeger and Schoeck (1955). Using their values of about 4 ev and 0·4 ev for the energies of jogs in edge dislocations in copper and aluminium respectively, the ratio of the number of jogs present in thermal equilibrium at the temperatures used in the experiments ($T_{\mathrm{Cu}} \doteqdot 400^\circ\mathrm{C}$ and $T_{\mathrm{Al}} = 200^\circ\mathrm{C}$) is

$$\exp\,[(4\ \mathrm{ev}/KT_{\mathrm{Cu}}) - (0{\cdot}4\ \mathrm{ev}/KT_{\mathrm{Al}})] = 10^{25}.$$

If the number of jogs in thermal equilibrium determines the rate of polygonization, then aluminium should polygonize to the same extent as the copper specimen in fig. 3 in 10^{-19} sec. This is obviously contrary to experience (Wilms and Wood 1949, Greenough and Smith 1950).

It can be concluded from a general examination of the present results that aluminium polygonizes about 100 times faster than copper. It is clearly unlikely that the vacancy concentrations differ sufficiently to account for much of this discrepancy. The phenomenon can however be explained by making the assumption, which is consistent with current ideas, that the number of jogs produced mechanically during the deformation of the copper specimen is of the order of 1/100 of the total number present in the aluminium specimen.

ACKNOWLEDGMENTS

The work described above has been carried out as part of the General Research Programme of the National Physical Laboratory, and this paper is published by permission of the Director of the Laboratory.

REFERENCES

GREENOUGH, G. B., and SMITH, E. M., 1950, *J. Inst. Met.*, **17**, 435.
MOTT, N. F., 1951, *Proc. Phys. Soc.* B, **64**, 729.
SCHOECK, G., and SEEGER, A., 1955, *Report of Bristol Conference* (London: The Physical Society).
WILMS, G. R., and WOOD, W. A., 1949, *J. Inst. Met.*, **16**, 693.

Gamma Rays from Inelastic Neutron Scattering in Sodium and Iodine

By ELIZABETH A. WOLF
Clarendon Laboratory, Oxford

[Received October 3, 1955]

THE gamma ray spectrum from inelastic scattering of 2·5 MEV neutrons in sodium metal has been measured with a sodium iodide crystal spectrometer, by the method described in a previous publication (Eliot, Hicks, Beghian and Halban 1954).

The scatterer was prepared by melting small blocks of sodium under dry liquid paraffin, into an aluminium can 5 cm in diameter, 3 cm deep, and 0·1 mm in wall thickness. Any oxide that had formed rose to the surface of the liquid metal and could be easily removed. The container was then closed with an aluminium lid and sealed. To compensate for scattering in the aluminium an empty can, similar to the one containing sodium, replaced the scatterer during background measurements.

Pulse height distributions were measured with and without the sodium scatterer, and normalized to the same number of neutrons entering the detector. The lower curve in fig. 1 shows the spectrum without scatterer, due to primary neutrons only. The upper curve shows the spectrum with scatterer, in which gamma rays from inelastic scattering in sodium are superimposed on the background due to neutrons. The spectrum due to sodium gamma rays only, with the background subtracted, is shown in fig. 2.

Fig. 1

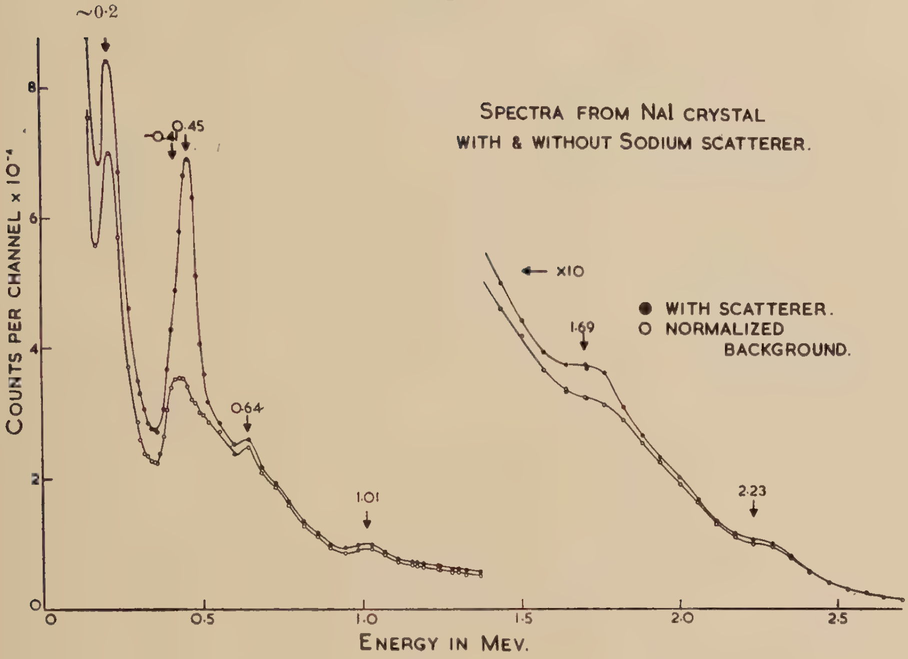
SPECTRA FROM NaI CRYSTAL
WITH & WITHOUT SODIUM SCATTERER.
● WITH SCATTERER.
O NORMALIZED BACKGROUND.
~0·2
0.41
0.45
0.64
1.01
← x10
1.69
2.23
COUNTS PER CHANNEL x 10⁻⁴
0
2
4
6
8
0
0.5
1.0
1.5
2.0
2.5
ENERGY IN MEV.

Fig. 2

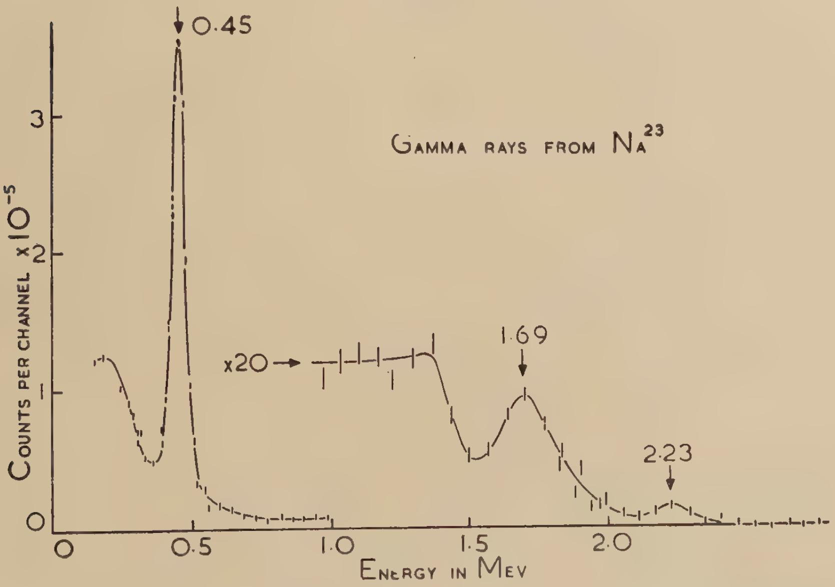
GAMMA RAYS FROM Na²³
0.45
x20 →
1.69
2.23
COUNTS PER CHANNEL x10⁻⁵
0
1
2
3
0
0.5
1.0
1.5
2.0
ENERGY IN MEV

With fast neutrons the most likely processes to occur in a NaI crystal are inelastic scattering in the sodium and iodine. Gamma rays from scattering in sodium will be enhanced by introduction of the scatterer, while those from iodine will not. It can be seen in fig. 1 that several peaks visible in the crystal background appear stronger in the spectrum with the scatterer, and from fig. 2 it is evident that these are due to gamma rays from sodium of energy

$$0{\cdot}45 \pm 0{\cdot}01,\ 1{\cdot}69 \pm 0{\cdot}03,\ \text{and}\ 2{\cdot}2 \pm 0{\cdot}1\ \text{MeV}.$$

The remaining peaks in the background are not enhanced by introduction of the sodium scatterer, and are therefore most probably due to scattering in the iodine. They correspond to photopeaks from gamma rays of energy

$$\sim 0{\cdot}2, \sim 0{\cdot}41,\ 0{\cdot}64 \pm 0{\cdot}05,\ \text{and}\ 1{\cdot}01 \pm 0{\cdot}05\ \text{MeV}$$

in good agreement with previous measurements of inelastic scattering in iodine (Kiehn and Goodman 1954 a, Scherrer *et al.* 1954, and Lind and van Loef 1955).

Previous measurements on sodium by various methods have indicated levels below 2·5 MEV of energy

0·439, 2·07, and 2·37 MEV (Endt and Kluyver 1954).

The strong 0·45 MEV gamma ray found by us is therefore almost certainly due to decay of the first excited state. The 1·69 MEV gamma ray may be due to direct decay of a new level of that energy to the ground state, or else to decay of a 2·14±0·04 MEV level by cascade through the first excited state. The ambiguity could be most easily resolved by measuring the threshold energy of the 1·69 MEV gamma ray with a neutron source of variable energy (Kiehn and Goodman 1954). The second alternative is supported by the presence of the 2·2 MEV peak, which would correspond to an ‘ addition peak ’ due to simultaneous detection of the two cascading gamma rays. Its intensity is somewhat greater than would be expected for such a peak (Kahr and Lyon 1953), but the difference is within experimental error.

ACKNOWLEDGMENTS

The author would like to thank Professor H. Halban and Dr. L. E. Beghian for supervising this work, and Messrs. D. Hicks and B. Milman for assistance and helpful discussions.

REFERENCES

ELIOT, E. A. (now WOLF), HICKS, D., BEGHIAN, L. E., and HALBAN, H., 1954, *Phys. Rev.*, **94**, 144.

ENDT, P. M., and KLUYVER, J. C., 1954, *Rev. Mod. Phys.*, **26**, 95.

KAHN, B., and LYON, W. S., 1953, *Nucleonics*, **11** (Nov.), 61.

KIEHN, R. M., and GOODMAN, C., 1954 a, *Phys. Rev.*, **95**, 636 ; 1954 b, *Ibid.*, **95**, 989.

LIND, D. A., and VAN LOEF, J. J., 1955, *Phys. Rev.*, **99**, 621.

SCHERRER, V. E., ALLISON, B. A., and FAUST, W. R., 1954, *Phys. Rev.*, **96**, 386.

The Interactions of Cosmic Ray Alpha-Particles

By C. J. Waddington
H. H. Wills Physical Laboratory, University of Bristol

[Received October 1, 1955]

This letter describes the results of a study of the nuclear interactions produced by α-particles of the primary cosmic radiation. These particles were recorded in various stacks of stripped and glass-backed nuclear emulsions exposed at balloon altitudes. Most of the disintegrations were observed in a stack of stripped emulsions exposed in such conditions that few of the incident α-particles had energies less than 0·5 bev/nucleon; the median energy of all the α-particles considered was approximately 1·3 bev per nucleon.

The nuclear disintegrations were detected by first making a systematic search for the tracks of fast α-particles (Waddington 1954), and then following them through the emulsions until they either left the stack, or interacted with a nucleus. Eighty-nine 'stars' were observed in a total effective path length of 1825 cm; the corresponding value of the interaction mean free path of an α-particle in emulsion is $20{\cdot}5 \pm 2{\cdot}2$ cm. A separation of the tracks into groups corresponding to α-particles of different energies, failed to reveal any significant variation over the energy range considered. Further, the mean value is in good agreement with that found by Quareni and Zorn (1955) for the mean free path of 350 mev α-particles, i.e. $20{\cdot}02 \pm 1{\cdot}67$ cm. In only two examples was a high energy α-particle observed to emerge from one of the disintegrations, a result indicating that the mean free path for absorption is only a little greater than that for interaction; if the α-particle interacts with a nucleus it rarely emerges.

The interaction cross section corresponding to the observed value of the mean free path, as observed in the present experiment, is equal to approximately half the value calculated from the equation derived from geometrical considerations:—

$$\sigma_{\rm cal}=\pi(R_n+R_\alpha)^2,$$

where R_n and R_α are the radii of the target and incident nuclei respectively, their magnitudes being given, for a nucleus of atomic number A, by the relation $R=r_0A^{1/3}$, with $r_0=1{\cdot}45\times10^{-13}$ cm. If r_0 is taken as $1{\cdot}20\times10^{-13}$ cm, the disparity between the observed and calculated values is still considerable: $\sigma_{\rm ob}=0{\cdot}70\sigma_{\rm cal}$. If, alternatively, the cross section is calculated assuming $R_\alpha=0$, it becomes greater than the experimental value, even when r_0 is taken to be $1{\cdot}45\times10^{-13}$ cm. Since the experimental cross sections found for energetic nucleons, and for the heavy nuclei of the cosmic radiation, are always less than those derived geometrically, the assumption that R_α may be neglected does not seem justified.

Sixty-eight of the stars observed in the present investigation, five of which were tentatively identified as due to collisions with hydrogen, have been analysed, in order to compare them with those observed by Ceccarelli *et al.* (1955). These authors detected the disintegrations due to α-particles by a direct search. It is well known that this method commonly suffers from the fact that there may be a considerable difference in the efficiency with which observers detect disintegrations of different types. In particular, there is a tendency to overlook small stars, a defect from which the present method is free. A comparison between the results from the two methods allows the effect of any scanning bias to be estimated. Figure 1 shows the distribution in the values of N_h for the stars observed in the two experiments. It has been convenient to plot an integral distribution—the number of 'stars' with N_h greater than any given value—and to normalize the two values corresponding to $N_h=7$. The results suggest that there was a considerable bias against detecting small stars in the earlier work. Whereas the early data suggested that only about 2% of the 'stars' had $N_h \leq 4$, the present results indicate that the true value is about 50% (see also Engler *et al.* 1954).

Fig. 1

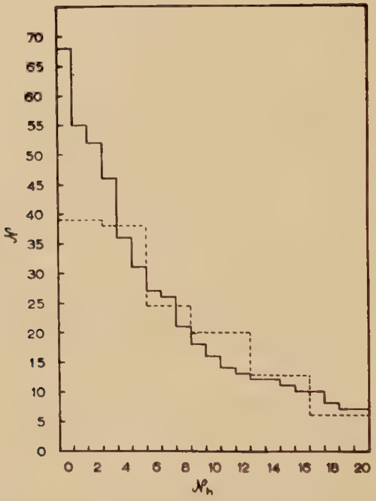

The integral N_h distribution for the stars found in the present investigation is shown by the continuous line; and that found by Ceccarelli *et al.* by the broken line, the two distributions being normalized at $N_h=7$.

A similar indication of the effects due to a failure to observe small stars, in methods employing direct scanning, is provided by the results shown in fig. 2, which gives the distribution in n_s of the stars found in this present investigation. The results of Ceccarelli *et al.* indicate that there is a peak in such a distribution at $n_s=1$, whereas in the present work it is actually observed at $n_s=2$. This discrepancy can be readily accounted for if the majority of the small stars with $N_h \leqslant 4$—believed, on the basis of the evidence presented in fig. 1, to have been overlooked in the early work, have two associated shower particles. This interpretation is supported by the distribution in the values of n_s of those stars observed in the present experiments which show a total liberation of energy, among the evaporation and ‘ knock-on ’ fragments, of less than 100 MeV, and which have not been tentatively classified as collisions with hydrogen. The values of n_s for such stars, all of which have $N_h \leqslant 4$, are shown shaded in fig. 2, and display a very pronounced peak at $n_s=2$ which accounts for most of the peak observed in the total distribution.

Fig. 2

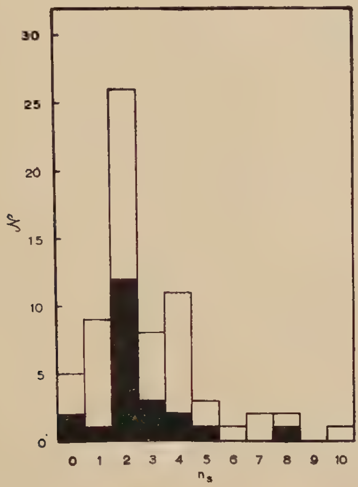

The distribution in n_s of the stars found in the present investigation. Those shown ‘ blocked-in ’ correspond to ‘ stars ’ which, while showing less than 100 MeV visible energy in the form of black or grey ‘ prongs ’, have not been classified as due to collisions with hydrogen nuclei.

The observed features—both of the mean free path and of the distribution in N_h of the disintegrations—may be explained by dividing the interactions into two separate classes. For simplicity, this may be done on the basis of a purely geometrical model, in which the significant parameters are taken to be the overlapping target areas of nuclear matter in the collisions rather than the interpenetrating volumes. The two types of collisions are then :

(i) Central collisions in which all the nucleons of the incident α-particle pass through the nuclear matter of the target nucleus. The interaction cross section for such collisions will be given by

$$\sigma_c=\pi(R_n-R_\alpha)^2.$$

(ii) Peripheral collisions in which not all the nucleons of the incident nucleus pass through the nuclear matter of the target nucleus.

The relative cross sections for collisions of these two types is independent of the assumed value of r_0, and it is found that for emulsion nuclei only $\sim 14\%$ of the total cross section will be available to central collisions. The results of Ceccarelli *et al.* indicate that for these central collisions the nucleus is opaque, even when allowance is made for the transparency of the nuclei to individual nucleons. In order, therefore, to account for the small value of the experimental cross section, it is necessary to assume that the effectiveness of peripheral collisions is small. For such collisions, the nucleus is partially transparent. The degree of transparency deduced from the results depends on the assumed value of r_0, and represents an average over the various possible impact parameters. Using the experimentally determined cross section, and assuming that $r_0 = 1{\cdot}45 \times 10^{-13}$ cm, the transparency f, for peripheral collisions is found to be 0·43 ; the corresponding value for the fraction of central collisions among those observed is 27%. If, however, $r_0 = 1{\cdot}20 \times 10^{-13}$ cm, then the transparency is $f = 0{\cdot}71$, and the percentage of central collisions is 18% of those observed.

In the present work, the number of stars with $N_h \geqslant 9$ was 27% of the total. Since the cross section for central collisions is almost entirely due to the heavy nuclei of the emulsion, it appears reasonable to assume that the number of such stars represents an upper limit to the number of central collisions. This assumption is supported by the observed peak at $n_s = 2$ in the distribution shown in fig. 2, and at $n_s = 1$ in the earlier work in which, it is suggested, there was a much larger proportion of central collisions.

It seems therefore that the simple model of a ' black ' nucleus proposed by Ceccarelli *et al.* should be replaced by one in which the core only of the nucleus is opaque, while the edges have a mean transparency of which the estimated value depends on the value taken for r_0. The use of such a model, in calculating the mean free paths in media other than emulsion, gives results which are in good agreement with the experimental values in glass, found by Bradt and Peters (1950) ; and with the values based on their model, which assumes that a certain overlap of the nuclear radii must occur before an interaction can take place.

REFERENCES

BRADT and PETERS, 1950, *Phys. Rev.*, **77**, 54.

CECCARELLI, QUARENI and ZORN, 1955, *Il Nuovo Cim.*, **1**, 669.

ENGLER, HARBER-SCHAIM and WINKLER, 1954, *Il Nuovo Cim.*, **12**, 930.

QUARENI and ZORN, 1955, *Il Nuovo Cim.*, **1**, 1282.

WADDINGTON, 1954, *Phil. Mag.*, **45**, 1312.

The Paramagnetic Resonance Spectrum of Chlorine Dioxide

By J. E. Bennett and D. J. E. Ingram
University of Southampton

[Received October 26, 1955]

Chlorine dioxide is one of the few stable gases which possess unpaired electrons in their normal chemical state and are therefore paramagnetic. Detailed resonance measurements have been made on the other common gases, such as nitric oxide, nitrogen peroxide and oxygen (Beringer and Castle 1950, 1951), but none have so far been reported on chlorine dioxide. Preliminary experiments (Bennett *et al.* 1955) have indicated, however, that an intense absorption could be obtained from aqueous solutions of chlorine dioxide with a marked hyperfine structure from the nuclear moment of the chlorine atoms.

In this letter measurements on different solutions of chlorine dioxide are reported and the variation of the hyperfine splitting with the physical state of the solvent shows that a strong ‘ averaging ’ or ‘ tumbling ’ effect is produced by the mobile solvent molecules. The simplest type of spectra is that obtained from a dilute solution of chlorine dioxide in alcohol at 1·25 cm wavelength and 200°K, as shown in fig. 1. Four narrow and well resolved lines are observed, the width of each line being 8 gauss with an overall separation of 50 gauss. The g value of $2{\cdot}010 \pm 0{\cdot}001$, corresponding to the centre of the pattern, can be measured by comparison with the hydrazyl absorption line, which is exactly coincident with the highest field hyperfine component at 1·25 cm wavelength. When this same solution is cooled to liquid oxygen temperatures a marked change in the spectrum is observed, as shown in fig. 2. It would appear that the hyperfine splitting has considerably increased and also become markedly anisotropic. As a result the individual lines are noticeably broadened and the pattern corresponds to an averaging over all possible orientations, with a maximum splitting of 170 gauss, which is more than three times that observed in the liquid solvent.

These results may be most readily interpreted by assuming that there is a strong crystalline field axis acting in each molecule when in the solid solution, which produces the anisotropy in the hyperfine splitting. The very narrow and well resolved lines obtained from the liquid solution show that the motion of the solvent molecules is extremely effective in averaging out the anisotropy in the splitting. This radical change in the spectrum on freezing the solvent is quite general as the two different patterns are also obtained from solutions in acetone, benzene and water. The temperature at which the pattern changes always corresponds to the melting point of the particular solvent.

The lines in the liquid solvent are broadened by both ‘ spin–spin ’ and ‘ spin–lattice ’ interaction. Thus, if the concentration of the dissolved chlorine dioxide is too high, the individual hyperfine components are not resolved at any temperature and a single broad absorption of 150 gauss total half-width is produced. This same line is also obtained from the pure chlorine dioxide in either the liquid or solid phase. A broadening of the individual lines is also observed as the temperature is raised, and in the case of alcohol only a single unresolved line is obtained at room temperature. This, together with the departure of the g value from that of a free-spin indicates that there is considerable orbital coupling to the unpaired electron.

Fig. 1

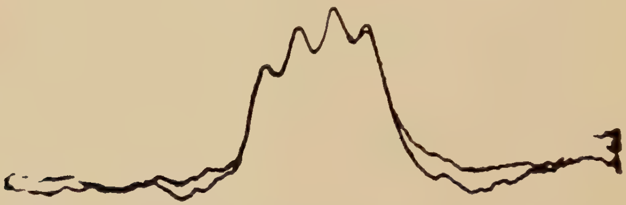

Spectrum observed from alcoholic solution of chlorine dioxide at 200°K and 1·25 cm wavelength.

Fig. 2

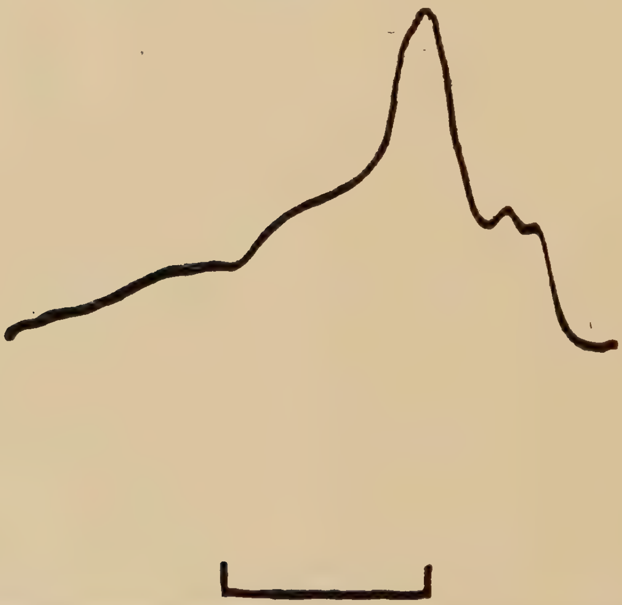

Spectrum observed from same solution as in fig. 1, but at 90°K.

The two spectra are on the same scale and the line at the bottom is equivalent to a 100 gauss splitting.

Another feature of interest is the difference between the hyperfine patterns at 3 cm and 1·25 cm wavelengths. The solution which gives the four lines of fig. 1 at 1·25 cm wavelength gives an identical pattern at 8 mm, but only a single line of 26 gauss width is obtained at 3 cm wavelength. This is again true for all solvents, and it would appear that a form of exchange narrowing is present so that frequencies higher than 10 000 Mc/s are necessary to resolve the individual hyperfine components. In contrast to this the same spectra is observed at all wavelengths at 90°K showing that the ‘ tumbling ’ effect of the mobile solvent molecules, and any exchange interaction between the chlorine dioxide molecules, have both been quenched at this temperature.

REFERENCES

BENNETT, J. E., INGRAM, D. J. E., SYMONS, M. C. R., GEORGE, P., and GRIFFITH, J. S., 1955, *Phil. Mag.*, **46,** 443.

BERINGER, R., and CASTLE, J. G., 1950, *Phys. Rev.*, **78,** 581, **80,** 114 ; 1951, *Ibid.*, **81,** 82.

X. REVIEWS OF BOOKS

Radio Astronomy. By J. L. PAWSEY and R. N. BRACEWELL. (Oxford: University Press, 1955.) [Pp. x+357+23 plates.] Price 55*s*.

To present a well-balanced review of a subject which is expanding as rapidly as radio astronomy is no easy task and the authors of this volume, another in the series of International Monographs on Radio, have achieved a commendable degree of success. In this book, which is certainly the most comprehensive account of the subject which has yet appeared, the growth of the various branches is taken to approximately mid-1952. It was during this period that most of the fundamental advances were made; these include the accurate location of the most intense radio stars and their subsequent identification with visual objects both inside and outside the galaxy, the discovery of the 21 cm hydrogen line, the detailed studies of thermal radiation from the solar corona and the spectrum analysis of the enhanced radiation associated with solar activity.

The book appears to be written primarily for the physicist with no previous knowledge of the subject, and the first three chapters are devoted to an account of the observational techniques and to the theory of radio waves in ionized gases. Two additional chapters deal with some of the basic features of general astronomy and astrophysics which are relevant to radio astronomy. Further chapters give a detailed account of solar, lunar and cosmic radio emission, the investigation of meteors and the moon by the radar echo technique, and effects introduced by the earth's atmosphere. Throughout the book the reader is constantly referred to original papers and detailed references are given at the end of each chapter. The text is well illustrated by line diagrams and some two dozen plates are included. The latter show different types of aerial system and also some photographs taken at the Mt. Wilson and Palomar observatories. Unfortunately we are not shown the colliding galaxies in Cygnus.

Impeccably printed by the Oxford University Press this book can be warmly recommended to all who desire a general survey of the principal branches of radio astronomy, and it should be of particular value to research workers who are newcomers to the subject. A. H.

Applied Group-Theoretic and Matrix Methods. By B. HIGMAN. (Oxford: Clarendon Press.) [Pp. xii+454.] Price 60*s*.

THIS book gives an account of the applications of group theory to a wide variety of subjects in physics and chemistry including some subjects less frequently treated such as Eddington's quantum relativity. It is useful as giving an indication of the fields in which the theory can be applied, but in covering so wide a field it seems to the reviewer to fall between two stools; the treatment is not rigorous and not complete enough to serve as an authoritative work on any one branch of the subject; it is on the other hand too advanced and too long to serve as an introduction to the subject for a beginner who wants to learn it with a view to its applications in natural science. Also the book makes use of a notation for vectors which is different from that most commonly in use, and the explanation of the crystalline notation is spread over a very considerable part of the book. The presence of many small defects such as these would make it difficult to use as a reference book. V. H.

[The Editors do not hold themselves responsible for the views expressed by their correspondents.]

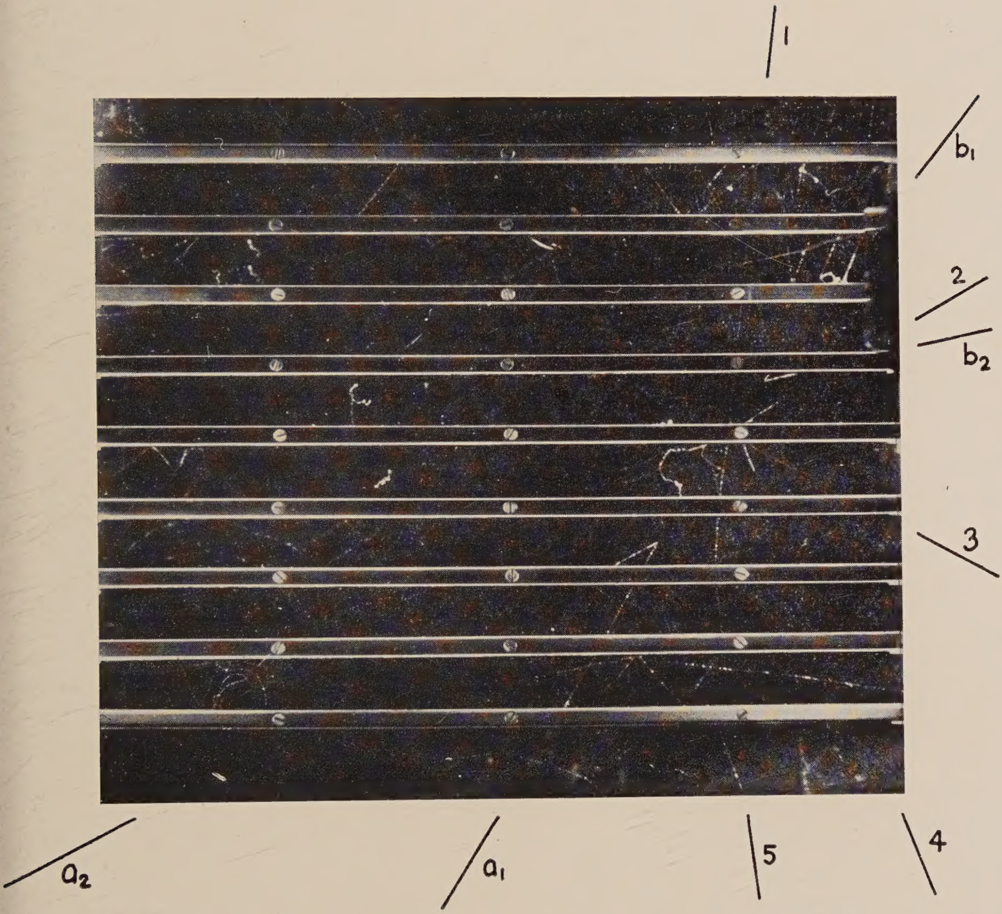
1
b₁
2
b₂
3
a₂
a₁
5
4

Fig. 1

Fig. 2

Fig. 3

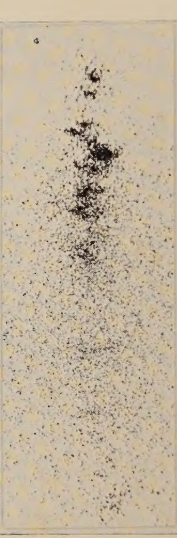

Fig. 4

1 mm

The scale represents 1 mm on the original.

Fig. 1. Diffraction photograph of annealed copper.

Fig. 2. Diffraction photograph of copper stretched 6–7% in 57 hr at 400°c.

Fig. 3. Diffraction photograph of copper stretched 6% in 308 hr at 400°c.

Fig. 4. Diffraction photograph of aluminium stretched 8·4% in 5 hr at 200°c.